TÉCNICO LISBOA

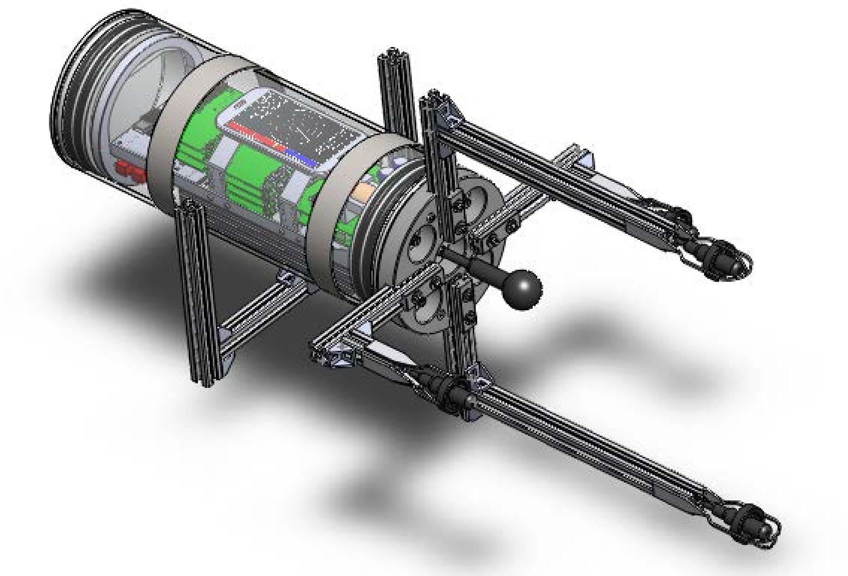

Development of a Portable Underwater Tool to Track Marine Animals

Marta Joana Cunha Ribeiro

Dissertação para a obtenção do grau de Mestre em
Engenharia Aeroespacial

Júri

Presidente:	Professor Doutor João Manuel Lage de Miranda Lemos
Orientador:	Prof. Doutor Paulo Jorge Coelho Ramalho Oliveira
Co-orientador:	Mestre Bruno Miguel Simões Carvalho Cardeira
Vogais:	
Vogais:	

Outubro de 2013

Acknowledgments

The present thesis was the final result of a research fellowship of almost a year in the MAST/AM project. During this time I developed my work in a laboratory in ISR where beyond experimenting first hand what research work entails, I had the opportunity of working with people with an admirable level of knowledge.

My first words of appreciation are due to those who have given me such opportunity, namely my advisor Prof. Paulo Oliveira and my co-advisor Master Bruno Cardeira.

To Bruno Cardeira a second word of recognition for the continued support in the laboratory not only to me, but to everyone which contributed to the project.

To my colleagues in the MAST/AM project, Joel Reis and Nuno Carvalho, a word of friendship. Additionally, I could not neglect to mention Pedro Pereira and Bruno Gomes. Although they were not part of the MAST/AM project, they were part of my everyday at ISR.

A very special thanks to José Tojeira whose help in the construction of the tube was vital. I also want to express gratitude for his patient in teaching both me and my colleagues.

I also gratefully acknowledge the contribution of the remaining elements of the DSOR team: Manuel Rufino, Luis Sebastião, João Botelho, Marco Morgado and Bruno Gomes, for their outstanding assistance both in terms of knowledge and of more practical aspects throughout the development of the prototype.

Financial support: This work was supported by *Fundação para a Ciência e a Tecnologia*, in the scope of the project FCT MAST/AM - PTFC/EEA - CRO/111107/2009.

Resumo

O objectivo desta tese residiu em desenvolver uma arquitectura em tempo real capaz de aquisição e processamento de um sinal acústico submarino. Este protótipo foi implementado no interior de uma ferramenta portátil subaquática capaz de analisar sinais provenientes de pequenos transmissores inseridos em vários tipos de animais marinhos. O sinal é adquirido através de um sistema de *Ultra-Short Baseline* (USBL), composto por um conjunto de hidrofones instalados segundo uma geometria conhecida. Através das diferenças dos tempos de chegada do sinal acústico aos hidrofones, a posição é estimada em três eixos. A recepção e processamento deste sinal, combinada com a fusão de dados provenientes de um sistema de navegação inercial (INS) no interior da ferramenta, possibilita a estimação da posição do emissor num plano de referência estabilizado. Através de um sistema de visualização, a direcção do alvo relativamente ao mergulhador que transporta a ferramenta é apresentada ao mesmo, que poderá, então, efectuar seguimento e observação do animal marinho sem necessitar de ajuda exterior.

No início deste relatório de tese, é apresentada uma análise no âmbito de sistemas autónomos de aquisição e processamento de sinal acústico, arquitecturas em tempo real e sistemas de navegação inercial. Esta servirá como guia para a realização do protótipo da arquitectura desejada. Posteriormente, a validação e avaliação do desempenho do mesmo serão introduzidas a fim de ser determinada a sua viabilidade.

É de realçar que a ferramenta foi projectada e utilizada no âmbito do projecto "Metodologias Avançadas de Seguimento e Telemetria para Estudo de Animais Marinhos" (MAST/AM) coordenado pelo Instituto de Sistemas e Robótica (ISR) do Instituto Superior Técnico (IST), em parceria com o Centro de Ciências do Mar (CCMar/CIMAR), Departamento de Pesca e Aquicultura da Universidade Federal Rural de Pernambuco (DPA-UFRP) e *Hopkins Marine Station* (HMS). Financiado pela Fundação para a Ciência e Tecnologia (FCT), o objectivo deste projecto é a criação de ferramentas de baixo custo capazes de localizar animais marinhos portadores de um transmissor.

Palavras-chave: USBL, Arquitecturas em Tempo Real, Sistemas de Navegação, Sistema de Aquisição e Processamento de Sinais Acústicos Submarinos, Android development

Abstract

The purpose of this thesis was to develop a real time architecture capable of acoustic signal acquisition and processing. The architecture was implemented within a portable underwater tool capable of acquiring and processing underwater acoustic signals from small transmitters inserted in multiple marine animals. This architecture is built around the fusion of data from an Ultra-Short Baseline system (USBL), and an inertial navigation system (INS). USBL systems resort to a set of hydrophones disposed according to a known geometry. By computing the time difference of arrival of an acoustic signal in each hydrophone, the target's position can be estimated in three axis. Additional, the INS enables a stabilized reference frame. A display unit inside the portable tool serves as a visual interface for displaying the result of the signal processing and localization estimation to the diver carrying the tool, which is hence able to perform monitoring of the target's direction without external aid. The portable underwater tool is intended to be as compact and small as possible, in order to be easily carried by the diver.

This thesis report commences with a survey within the framework of autonomous systems for acquisition and processing of an underwater acoustic signal, real time architectures and inertial data acquisition systems, which will serve as a knowledge base for the development and implementation of the prototype. Furthermore, validation and performance assessment are presented in order to determine the feasibility of the system.

It is noteworthy that the portable underwater tool was developed and tested in the scope of the "Advanced Tracking and Telemetry Methodologies to Study Marine Animals" (MAST/AM) project conducted in *Instituto de Sistemas e Robótica* (ISR) of *Instituto Superior Técnico* (IST), in partnership with *Centro de Ciências do Mar* (CCMar/CIMAR), *Departamento de Pesca e Aquicultura da Universidade Federal Rural de Pernambuco* (DPA-UFRP) and Hopkins Marine Station (HMS). Funded by *Fundação para a Ciência e Tecnologia* (FCT), the projct's aim is to endow the scientific community with new moderate cost robotic tools able to track multiple tagged marine animals.

Keywords: USBL, Real-time Architectures, Navigation Systems, Underwater Acoustic Signal Acquisition and Processing, Android development

Contents

Acknowledgments **III**

Resumo **V**

Abstract **VII**

Contents **IX**

List of Figures **XV**

List of Tables **XVII**

Nomenclature **XIX**

List of Acronyms **XIX**

1 Introduction **1**

1.1 Objectives 2

1.2 Motivation 3

1.3 State-of-the-art 4

1.4 Main Contributions 6

1.5 Dissertation Outline 6

2 Real Time Architectures For Acoustic Signal Acquisition and Processing **9**

2.1 Acoustic Signal Acquisition 10

2.1.1 Components of a basic acoustic positioning system 10

2.1.2 Position systems architecture 12

2.1.2.1 Ultra Short or Super Short Baseline 12

2.1.2.2 Short Baseline 13

2.1.2.3 Long Baseline Baseline 13

2.1.2.4 Primary acoustic positioning system comparison 13

2.1.3 Time of Arrival Calculation 15

2.1.4 Time of Arrival Calculation of Sinusoidal Signal 16

2.1.5 Direction of the transmitter 18

2.1.6 Distance of the transmitter 20

2.2 Real Time Processing and Advanced Signal Techniques 20

3 Navigation Systems **23**

3.1 Orientation Representation 23

3.1.1 Rotation Matrix 24

3.1.2 Euler angles 26

3.2 Earth Surface Model 27

3.2.1 Earth's gravity and Centrifugal Force 28

3.2.2 The Ellipsoid 29

3.2.3 The Geoid 30

3.3 Reference Systems 31

3.3.1 Inertial Frame 31

3.3.2 NED frame 32

3.3.3 Body Frame 32

3.4 Inertial Navigation 33

3.5 Inertial System Configurations 34

3.5.1 Overview of Inertial Sensors 36

3.5.1.1 Gyroscope 36

3.5.1.2 Accelerometer 37

3.6 Earth's magnetic field 39

3.6.1 Magnetometer 39

3.6.2 AHRS and Orientation filter 40

3.7 Complementary Filter 41

4 System Design **49**

4.1 Acoustic 49

4.1.1 Hydrophone 49

4.1.2 Transducer . . . 50
4.1.3 Underwater Acoustic Tags . . . 50
4.2 Hardware Architecture . . . 51
4.2.1 Array . . . 51
4.2.2 Signal Processing . . . 51
4.2.3 Interrogator System . . . 53
4.2.4 Visualization Hardware . . . 54
4.2.5 Inertial Navigation Systems . . . 55
4.2.6 Outbound connection . . . 56
4.2.7 Temperature Reading . . . 58
4.2.8 Pressure Reading . . . 60
4.2.9 Power Source . . . 61
4.2.10 System Autonomy . . . 63
4.2.11 Dimensions and Weight . . . 66
4.2.12 Connectors . . . 66
4.3 Software . . . 68
4.3.1 Android's Kernel replacement and driver installation . . . 69
4.3.2 Visualization Application . . . 71

5 System Validation and Assessment 73

6 Conclusion and Future Work 77

A Matched filter and Correlation Function 79

B Vehicle INS simulation 81

C Simulik Model for the Complementary Filter for Pitch Estimation 83

D Hardware developed at ISR/IST 85
D.1 Automatic Gain Control Amplifier (AGCAMP) . . . 85
D.2 Battery Monitor (BATMONIT) . . . 85
D.3 Class D Power Amplifier (PWRAMPD) . . . 87
D.4 Microcontroller AVRCAN128 . . . 88
D.5 Power Connector (PWRCONN) . . . 89

D.6 Power Supply/Can opto-isolation and termination/RS-485 board (PWROPT0485) . . . 89
D.7 Switching Low Noise Power (SWLNPWR) . . . 90
D.8 Voltage Gain Amplifier with Band-Pass Filter (VGAMP) . . . 92

E Parts design in Solidworks© 95

List of Figures

1.1 MAST/AM Mission scenario. Source : [56] (Modified). 2

1.2 Products from VEMCO©. 4

1.3 Products from JW Fishers company. 5

2.1 Basic acoustic positioning system architecture. 10

2.2 Primary types of acoustic positioning systems. 14

2.3 Match Filter Model. 16

2.4 Response of a matched filter to a sinusoidal signal under ideal an non-ideal scenarios. 17

2.5 Direction of the transmitter 19

2.6 Distance of the transmitter. 20

2.7 DSP based acoustic signal acquisition architecture. 22

3.1 Vector relative to frame. 23

3.2 Euler angles. $z-y-x$ convention (ψ - Yaw; θ - Pitch; $\phi - Roll$). Source: [23]. . 26

3.3 Ellipsoid and Geoid representation. 31

3.4 Representation of the Earth's, Geoid's and Ellipsoid's surface. 31

3.5 NED and Body Frame representation. 33

3.6 Gimbaled platform INS. Source: [38]. 34

3.7 Navigation algorithm for a stable platform system. 35

3.8 Navigation algorithm for a strapdown system. 35

3.9 Model of a micromachined gyroscope. 37

3.10 Earth's magnetic field. 40

3.11 Movement of the diver handling the MAST/AM tool. 42

3.12 Complementary Filter. 43

3.13 Pitch estimated based on data from IMU using complementary filters. 44

3.14 Vehicle's graphic representation. Source: [55]. 44

3.15 Diver's path simulated. 45
3.16 Simulation's resulting Euler angles. 45
3.17 Simulation's resulting INS output. 46
3.18 MAST/AM tool's pitch rotation estimated versus simulated pitch, in $\{B\}$. 46
3.19 Difference between pitch estimated and simulated, in $\{B\}$. 46
3.20 Results of the transmitter's distance and depth difference to the diver when using $\hat{\theta}$. 47

4.1 Acoustic positioning system devices. 50
4.2 VEMCO© V16 transmitter. Source: [74]. 51
4.3 USBL array attached to the tool. 51
4.4 DSP stack. 53
4.5 Architecture for signal acquisition and processing. 53
4.6 Interrogator system architecture. 54
4.7 Connections established with input and output ports of the DSP stack. 55
4.8 Jitter from Android Device Sensors. 57
4.9 Jitter from Microstrain's Sensors. 58
4.10 Outbound Connection, DSP and Android's device connected through an Ethernet switch. 58
4.11 Architecture for control and communication with the BMP085 sensor. 59
4.12 Connections established with the Android device. 59
4.13 MAST/AM tool's sealing method and pressure port. 60
4.14 Experiment: pressure and temperature rise inside the MAST/AM tool. 61
4.15 OTG Y cable with charging enabled. 63
4.16 Architecture of the prototype for the MAST/AM tool. —— power, −− data . . 64
4.17 MAST/AM tool dimensions (mm). 66
4.18 MAST/AM tool final prototype. 67
4.19 IE55 connector and pinout. 67
4.20 SubConn© connector and pinout. 68
4.21 Diver graphical user interface. 72

5.1 Albufeira experiment. 74
5.2 Trajectory of the boat during experiment at Albufeira Bay, Portugal. 74
5.3 Belém dock sea trials setup. 75
5.4 Comparison between signal output of AGCAMP and VGAMP. 76

B.1 *Simulinks* block diagram for the vehicle's simulator implementation. Source: [55]. 81

C.1 *Simulink* Model for Complementary Filter for Pitch Estimation. 83
C.2 *Simulink* Model for Complementary Filter for Pitch Estimation. 83
C.3 Acceleration forces in $\{B\}$. 84

D.1 AGCAMP board. 85
D.2 AGCAMP block diagram. 86
D.3 BATMONIT board. 86
D.4 PWRAMPD board. 87
D.5 PWRAMPD block diagram. 87
D.6 Microcontroller AVRCAN128 board. 88
D.7 PWRCONN board. 90
D.8 PWROPT0485 board. 90
D.9 SWLNPWR board. 91
D.10 SWLNPWR block diagram. 91
D.11 VGAMP board. 92
D.12 VGAMP block diagram. 92

E.2 Devices designed in Solidoworks. 97

List of Tables

2.1 Primary Acoustic Systems Comparison. Source: [78, 10]. 14

4.1 Sensors available at Samsung Galaxy SIII LTE. Acquired by direct request from the sensors. The API provides several classes and interfaces, which allow to request values for maximum range, manufacturer, power requirements, and resolution [37, 53]. 56

4.2 Microstrain's INS specifications. Source: [19]. 56

4.3 Consumption of devices inside the MAST/AM tool found by assumption. 64

4.4 Consumption of devices inside the MAST/AM tool found experimentally. 65

4.5 IE55 connector pin. 67

4.6 IE55 pinout. 67

4.7 SubConn© connector pin. 68

4.8 SubConn© pinout. 68

5.1 Results from the experiment at Belém dock. 75

B.1 Vehicle's characteristics. 82

D.1 PWRAMPD specifications. 88

D.2 PWROPT's DC-DC converters specifications. 90

D.3 VGAMP specifications. 93

Nomenclature

$\hat{s}$ Estimation of vector s.

$\{B\}$ Body Frame.

$\{I\}$ Inertial Frame.

a Ellipsoid's semi-major axis.

b Ellipsoid's semi-minor axis.

C Capacity value.

e Ellipsoid's eccentricity.

f Ellipsoid's flattening.

I Current Drawn.

t Time interval.

w Gyro measurements.

$\mathbf{f}$ Accelerometer measurement in {B}.

List of Acronyms

ACM Abstract Control Model.

AGC Automatic Gain Control.

AGCAMP Automatic Gain Control Amplifier board.

AHRS Attitude and Heading Reference Systems.

AUV Autonomous Underwater Vehicle.

BATMONIT Battery Monitoring board.

CPU Central Processing Unit.

DC Direct Current.

DGND Digital Ground.

DMA Direct Memory Access.

DSOR Dynamical Systems and Ocean Robotics Lab.

DSP Digital Signal Processor.

ECEF Earth-Centered, Earth-Fixed.

ECI Earth Centered Inertial.

FFT Fast Fourier Transform.

GPS Global Positioning System.

IC Integrated Circuit.

IMU Inertial Measurement Unit.

INS Inertial Navigation System.

IP Internet Protocol.

ISR *Instituto de Sistemas e Robótica.*

IST *Instituto Superior Técnico.*

LBL Long Baseline acoustic positioning system.

LTP Local tangent plane.

LTP Local Tangent Plane.

LZD Lead Zirconate Titanate.

MAST/AM *Metodologias Avançadas de Seguimento e Telemetria para estudo de Animais Marinhos.* (Translation: Advanced methods for tracking and telemetry for the study of marine animals.)

MEMS Microelectromechanical systems.

MFLOPS Million Floating Point Operations Per Second.

MIPS icroprocessor without Interlocked Pipeline Stages.

NED North/East/Down frame.

OS Operating System.

OTG USB On-The-Go. Specification that allows USB devices to act as a host.

PC Personal Computer.

PPS Pulse Per Second.

PWM Pulse Width Modulation.

PWRAMPD Power Amplifier Class D board.

PWRCONN Power Connector board.

PWROPT0485 Power Supply/CAN opto-isolation and termination/RS-485 board.

RF Radio Frequency.

RFID Radio Frequency Identification.

ROV Remotely Operated Vehicle.

RS-232 Standards for serial binary single-ended data and control signals connecting between DTE (data terminal equipment) and DCE (data circuit-terminating equipment).

SBL Short Baseline acoustic positioning system.

SNR Signal to noise ratio.

SS Spread Spectrum.

SSBL Super Short Baseline acoustic positioning system.

SWLNPWR Switching Low Noise Power board.

TCP Transmission Control Protocol.

TDOA Time Difference of Arrival.

TOA Time of Arrival.

UHF Ultra High Frequency.

USB Universal Serial Bus.

USBL Ultra Short Baseline acoustic positioning system.

VGAMP Voltage Gain Amplifier with Band-Pass Filter.

VRU Vertical Reference Unit.

1 Introduction

Worldwide, development of underwater vehicles has expanded to the point where they have become able to accurately survey large ocean areas. Routine operations such as surveillance, environmental monitoring and underwater inspection are nowadays tasks commonly performed either by remotely operated vehicles (ROVs) or by autonomous underwater vehicles (AUVs). The ability of reaching the deepness of the oceans and perform these procedures, often impossible or hazardous for humans, makes marine robotic tools emerge as one of the strongest focus of investigation and efforts by the robotics scientific community [54]. This, combined with advances in telemetry systems and the decreasing size of transmitters along with increasing reliability of equipment has resulted in the possibility for applications with smaller species, in salt or brackish water [56]. Acoustic based telemetry can provide important knowledge on the behavior of various types of marine animals, as the results of direct observation of their habitats, migrate patters, among others, are instrumental to validate and solve a number of challenging problems in marine biology.

Some of the most important concerns for underwater navigation are the effects of acoustic propagation. Electromagnetic energy cannot propagate appreciable distances in the ocean except at very low frequencies. Acoustic energy, however, propagates well in the ocean, and hence acoustic transponders are used to guide the motion of an underwater vehicle without the need for resurfacing. Acoustic transmitters produce continuous or coded omnidirectional signals that can contain the identification of the animal or information from installed sensors. The primary choice for underwater positioning often resides among systems such as long baseline (LBL), short baseline (SBL) and ultra-short baseline (USBL). The study of these systems is, thus, considerate to be of high importance for the implementation of underwater applications.

The use of these robotic platforms requires low-cost, compact, high performance robust navigation systems that can accurately estimate the vehicle's position and attitude. Navigation is an important requirement for any type of mobile robot, but this is especially true for autonomous underwater vehicles. Good navigation information is essential for safe operation and recovery of an underwater vehicle. For the data gathered by an underwater vehicle to be of value, the location from which the data has been acquired must be accurately known [49]. In fact, the design and implementation of navigation systems stands out as one of the most critical steps towards the successful operation of autonomous marine robotic vehicles. Inertial navigation systems (INSs) provide self-contained passive means for threedimensional positioning in open ocean with excellent short-term accuracy. Consequently, their study is considered essentially for a successfully underwater vehicles operation. However, unbounded positioning errors induced by the uncompensated rate gyro and accelerometer errors degrade the INS accuracy over time. Diverse techniques, such as an Extended Kalman Filter (EKF) combined with aiding devices, such as the magnetometer, are adopted to estimate and compensate the INS integration errors build-up.

1.1 Objectives

More than a literature report concerning the problem of autonomous underwater navigation, this thesis aims to implement an architecture prototype for an underwater portable tool to be used in such underwater navigation applications. This tool will be employed in the Portuguese project MAST/AM [56], funded by the *Fundação para a Ciência e Tecnologia* (FCT), and developed at *Instituto de Sistemas e Robótica* (ISR)/*Instituto Superior Técnico* (IST) and Dynamical Systems and Ocean Robotics Lab (DSOR)/IST.

The MAST/AM project addresses advanced methodologies for the study of tagged marine animals, resorting to telemetry techniques. It intends to develop and operate robotic tools able to track the acoustic signals emitted by marine animals, based on range and depth data acquired with an USBL system aided by an INS. Tracking can be engaged over considerable distances, ranging typically from a few meters to several kilometers. The USBL and INS systems are implemented within the underwater portable tool. Said tool is be carried by a diver (Fig. 1.1), who is able to perform tracking of the marine animal which emitted the signal.

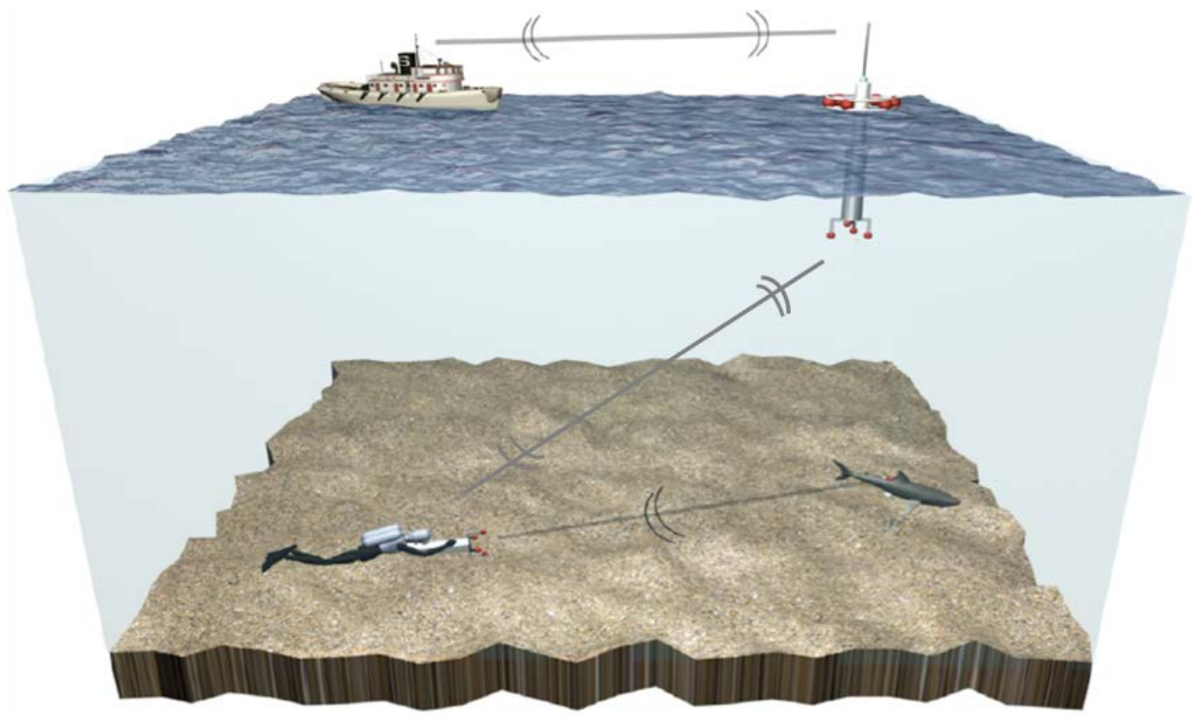

Figure 1.1: MAST/AM Mission scenario. Source : [56] (Modified).

The portable underwater tool will acquire a signal emitted from the marine animal, and process it in order to estimate its direction and distance. Depending on the algorithm implemented in the portable underwater tool, it may use an interrogator transducer for communication with a vessel at surface, whose response will provide information regarding the underwater tool's position. The algorithms designed and tested at ISR will be defined further along in this report.

Beyond being capable of acquiring and processing the received signal, the prototype architecture is restricted to a small size and weight to enable handling by the diver. The broad focus of this thesis will then cover the use of compact, high-performance navigation systems. The preliminary design and implementation phases will be described and the results obtained to validate the proposed approach will be presented.

1.2 Motivation

Many automatic underwater vehicles have been modified for the purpose of underwater tracking, however the MAST/AM project attempts to offset a market shortage.

Nowadays, tracking of marine animals is achieved through the insertion of a tag (Fig. 1.2a) which acts as a transmitter of a known signal. This signal is acquired by a receiver and processed in order to obtain some information concerning the location of said marine animal. Regarding the production and sale of these products for emission and reception, one can state that the brand VEMCO© is the most acquired by the scientific community. One of the purposes of the MAST/AM project is for the signal acquisition and processing to be compatible with VEMCO© emitters hence being compatible with the most commonly used products.

Taking into account the portable underwater tool was to act as a VEMCO© tag detector, it was regarded as relevant to analyze what the brand already has to offer in the field of signal detectors. Two products were considerer valuable for underwater tracking and surveillance: the VR100 receiver (Fig. 1.2b) and the VEMCO© Positioning System (VPS).

The VR100 receiver is designed for manual tracking of aquatic animals from small boats or for recording laboratory data. It is only capable of computing if a signal has been received and its strength. No information regarding the transmitter's distance or direction is given. Consequently, researchers are limited to an estimation of a large area where the transmitter may be (the area where the receptor registers the signal).

Secondly, the VPS is a underwater acoustic positioning system, which consists on the deployment of transmitters on the animals or objects being tracked, and of receivers (Fig. 1.2c) at fixed stations, in a area of interest to detect and record their transmissions. Receivers are usually arranged in a grid of triangles and squares. VPS is based on Time Difference of Arrival (TDOA) calculation. It measures differences in transmission detection times at pairs of time-synchronized receivers, and converts these to distance differences using the signal propagation speed. The difference in distance indicates how much closer or farther the transmitter is to one receiver than the other. With a minimum of three receivers, the position of the transmitter can be calculated in three axis. Despite promising a good rate of success, this system has the disadvantages of being restricted to a static area enclosed by the receivers and requiring a fairly complex setup. Results processing entails collection of the receivers' data and subsequent analysis. Consequently, this system can solely be employed for periodically analysis of the movement of a transmitter and not for real time position calculation.

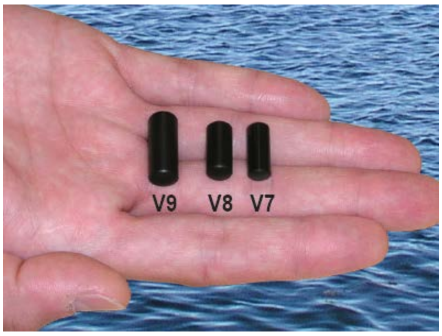

(a) Example of VEMCO©'s tags. Source : [75].

(b) VR100, VEMCO©'s receiver. Source : [77].

(c) VEMCO©'s VPS receiver. Source : [76].

Figure 1.2: Products from VEMCO©.

The previous products work reasonable well within their applicability range, however there is a mission profile they are not accountable for: direct tracking and surveillance of a tagged animal. They only avail for confirming their presence at a given instant of time, at a location nearby, or for periodically examination of the transmitter's path pattern. Ergo it is easily comprehended how researchers have a constant need of a more maneuverable product capable of a precise estimation almost immediately.

1.3 State-of-the-art

Having set a clear notion that this project intends to develop a product not yet on the market, it is of importance to analyze the progress being made in other projects which also attempt to achieve similar tracking devices, as to confirm the MAST/AM project's innovative implementation and advantages.

Before stepping forward, an important notion to assert is the fact that the MAST/AM portable underwater tool intends to be an off the shelf product with the single application of underwater tracking using VEMCO© tags, which distinguishes the prototype of this thesis from an AUV. Although, the MAST/AM tool resembles an AUV in terms of its shape, and the architecture of specific AUVs may be considered as groundwork for this tool (in such case it is advisable the study of [72, 32, 60]), its aim varies widely from an AUV's. The later are designed to navigate underwater, being capable of reaching high depths. Hence requiring a propulsion system, control surfaces, and an autonomy suitable for the mission's expected time length. The MAST/AM tool has sufficient autonomy for powering the system, its shape is a "torpedo" format, which most favors movement, similar to the majority of AUVs, however is does not require a propulsion system and control surfaces as its movement is induced by a diver. A correct definition of the MAST/AM final product would be one of an underwater tracking tool and not an AUV.

To the best knowledge of this thesis's author, there is no AUV on the market, off the shelf, with direct specifications for tracking underwater tags. Using an AUV for this purpose requires modifications to its initial firmware and architecture. As one can rapidly apprehend, this entails several disadvantages in comparison with the prototype of this thesis. Most AUVs are not handleable by a human hand, requiring some sort of grasp mechanism for retrieval. Many AUVs mission profiles include data sending to the surface. Usually, it resorts to a data logger for data recording and posterior analysis, or a link for continuous communication with an unit closeby (usually a vessel at surface). For the latter, an antenna must be included in the AUV and it must be above water. Due to the this specification, many AUVs present an overhead bulge which is above water, where the antenna is situated, while the rest of the vehicle's body is below water line. The MAST/AM tool does not need to account for data transmission. Data is processed and presented to the diver directly. Lastly, and widely significant, costs of the MAST/AM tool are significantly lower compared to an AUV.

Taking into account the two last paragraphs, it is of more value to analyze the state-of-art of similar underwater tools which act only as a tracking device, instead of those which act primarily as standard AUVs. Currently, an underwater tracking tool off the shelf, in accordance with what the author of this thesis was able to ascertain, is solely manufactured by a company named "JW Fishers" [25], which is specialized in underwater search systems. Within its product line, two products are found whose direct application is similar to the one of the MAST/AM tool: JW Fisher's Pinger Receiver(PR)-1 (Fig. 1.3a) and Diver Held Interrogator(DHI)-1 (Fig. 1.3b).

(a) JW Fishers's PR-1 (Pinger Receiver). Source: [31].

(b) JW Fishers's DHI-1 (Diver Held Interrogator). Source: [31].

Figure 1.3: Products from JW Fishers company.

The PR-1 Pinger Receiver is designed to locate any pinger transmitting a frequency between 3 kHz and 97 kHz. The receiver can be carried by a diver or deployed from a boat. When the diver points the receiver in the direction of the pinger, an audio alarm sounds through an underwater earphone and a LED light bar flashes. As the diver approaches the pinger, the audio tone gets louder and the receiver's light bar flashes more LEDs. Secondly, the DHI-1 Diver Held Interrogator can also be carried by a diver or deployed from a boat. When the diver points the DHI-1 in the direction of a transponder, an audio alarm is activated, a LED light bar flashes and the distance to the transponder is displayed in a digital screen.

A direct comparison between the products stated above and the MAST/AM tool raises many disadvantages for the former. The DHI-1 calculates the distance to the transponder by measuring the time between the transmitted signal and the return signal, whereas the pinger uses only the strength of the signal. These methods are highly prone to error. The later depends upon the sensitivity of the receiver, and the former does not take into account multipath sustained by the received signal. Furthermore, heading or depth are not estimated. As previously stated, the MAST/AM tool aims to estimate the target's position in three axis by computing the TDOA in all hydrophones of an array positioned at one end of the tool. Additionally, data is presented to the diver resorting to a visual interface resulting in a easier and faster comprehension than sound volume and a compass.

Products available nowadays on market present a series of limitations the MAST/AM tool intends to surpass. A device operated by a diver with an array of hydrophones and capable of computing TDOA, is something new to both market and academic practices.

1.4 Main Contributions

The main contributions of this thesis are associated with more engineering aspects of the design, development and implementation of an integrated USBL/INS prototype to be used as a low-cost tool for tracking of tagged marine animals and to be carried by a diver. Apart from producing a tool which will be used in future underwater applications, the architecture study may serve as a guide for the design of similar tools or prototypes. Additionally, Navigation Systems are addressed for the purpose of estimating the vehicle's position and performing platform stabilization.

Considering the relevance of this thesis for the completion of studies in Avionics Master's in Aerospace Engineering, it is of importance to emphasize its contribution in terms of increasing both theoretical and practical knowledge in the development of embedded systems, sensors operation and signal processing techniques.

1.5 Dissertation Outline

This thesis report is organized in the following way:

Notation Throughout this thesis, bibliographic references are cited in square brackets, e.g [1], referring to its number in the list of bibliographic references in page 99.

Chapter 1 Addresses motivation for designing the MAST/AM portable underwater tool and state-of-the-art analysis on the subjects of underwater tracking devices.

Chapter 2 Definition of the primary system types for acoustic signal acquisition in underwater surveillance and tracking missions, and the required equipment. TOA, transmitter's direction and distance calculation. Introduction of real-time processing used for advanced signal processing techniques. Definition of a Digital Signal Processor employed in the prototyped architecture.

Chapter 3 Definition of an INS, required for the correct estimation of the direction of the target, a marine animal. Reference frames and coordinated systems applied in the MAST/AM project. Analysis of the various methods for Earth surface delineation. Application of a complementary filter for platform stabilization.

Chapter 4 Addresses the design and development of the architecture for the prototype of the portable underwater tool.

Chapter 5 Assessment of the architecture prototype presented herein. The overall system was validated with experimental data obtained at sea.

Chapter 6 Conclusion of this thesis as well as reference for possible future work based on the results obtained.

2 Real Time Architectures For Acoustic Signal Acquisition and Processing

In underwater applications, the Global Positioning System (GPS) is clearly not a solution for tracking, due to the strong attenuation of electromagnetic signals. Exception made for intermittent corrections by surfacing regularly. Available underwater acoustic positioning systems stand often as the primary choice for underwater positioning. These emit a sound wave which is acquired and processed in order to estimate position of the marine animal.

Transmitters used in airborne missions, or on the Earth's surface, use radio-frequency electromagnetic fields to transfer data. However, underwater, a different method must be applied as this radio signals are absorbed by water, and eventually cover short distances. As a result, acoustic signals are preferred for water signaling, as they are able to travel longer distances. The tags employed underwater convert electrical to acoustic energy. According to [61], Lead Zirconate Titanate (LZT) ceramic transducers are universally used due to of their considerable small size and superior efficiency. Furthermore, because of the need to operate near resonance for usable efficiency, cylindrical transducers are the only choice to produce omnidirectional radiation necessary for a telemetry transmitter. A sphere, the other possible structure, is larger for a given resonant frequency, and both expensive and difficult to incorporate into a transmitter. A sound wave is basically a pressure wave, and hence detection of an acoustic signal underwater is based on detecting a pressure variation.

Acoustic propagation is naturally slower than radio frequency propagation, which leads to lower communications rates than those of the latter. Furthermore, underwater hight data rate communications using acoustic waves have a greater number of difficulties:

- Travel time spread caused by multipath propagation, via multiple reflections from the surface and bottom or from particles and air bubbles present in the water column.

- Occurrence of Doppler spread of the channel, due to motion from both source and receiver as well as motion of the water column (waves). These motions causes a shift in the frequency of the signal transmitted along each signal path, also known as Doppler shift. Based on [6], the difference in Doppler shifts between different signal components, contributing to a single fading channel tap, is what is referred to as Doppler spread. Channels with a large Doppler spread have signal components that are each changing independently in phase over time, resulting in a very short coherence time. In other words, the amount of time in which the phase of the signal is predictable is very narrow.

- Increase of frequency directly related with propagation loss. Typical frequencies for underwater communication go from 10 Hz to 1 MHz. Frequencies above 1 MHz are absorbed rather quickly. The primary causes of absorption include viscosity, thermal conductivity, and chemical reactions involving ions in the seawater. All of them are caused by the repeated pressure fluctuations in the medium, which is the way sound waves propagate.

The latter difficulties depend not just on the location, but as well as in other factors as the weather generated noise and temperature gradients.

In the MAST/AM project, the transmitter in the target (a marine animal) will produce an acoustic signal, which will then be acquired and processed by the portable underwater tool.

2.1 Acoustic Signal Acquisition

Acoustic positioning systems can measure range and direction to transponders inserted in underwater vehicles and objects, or derive acoustic ranges from stations deployed onto the seabed, which are held by some form of fixed seabed framework. Acoustic signal acquisition is conducted under the basic principle of capturing and storing intended signals from these sources. The described system is capable of computing the target's position by determining TOA of the acoustic signal from the transmitter to a set of receivers with known positions. This can be a set of hydrophones, apart from each other, or an array of hydrophones placed in a non-planar configuration, which allows for 3D target localization.

2.1.1 Components of a basic acoustic positioning system

An acoustic positioning system typically has the components presented in Fig. 2.1. Some types of systems may have some variations, which will be described next.

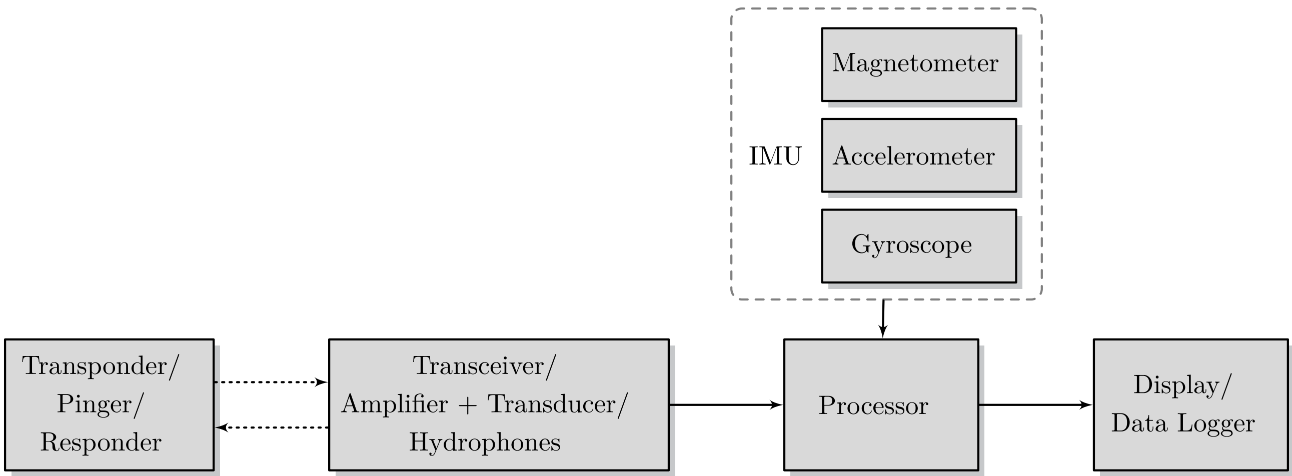

Figure 2.1: Basic acoustic positioning system architecture.

Foremost, a brief description, based on [10, 78], of each component:

Transponder A device which responds to an interrogation and needs no human intervention. It receives a week incoming interrogator signal, amplifies it and returns the signal in response. Can also be called a beacon or a station.

Transceiver Combination of transmitter plus receiver. Does not need an interrogator signal, but requires human interaction.

Transducer A device that converts a form of energy into another. Requires implementation of an amplifier in combination, as is does not amplify the week signal on its own. Does not need an interrogator signal.

Hydrophone An underwater microphone device designed to receive sounds underwater.

Processor Processing unit. This can go from a computer to any kind of device with an embedded Central Processing Unit (CPU). The processor computes the signal and sends the result to the display unit which will exhibit the computed location. Unless the system works as a pinger, which is periodic, the processor will be responsible for scheduling the interrogations by sending an electric signal.

Display Display unit, like a monitor, or a data logger. Serves as a visual interface for exhibiting the result of the signal processing and localization estimation.

Inertial Measurement Unit (IMU) An electronic device that measures and reports on a object's velocity, orientation, and gravitational forces, using a combination of accelerometers, gyroscopes and sometimes also magnetometers. It is worth noting that a magnetometer is not an inertial sensor but is often combined with inertial sensors in order to improve the accuracy of the calculated orientations [46].

Responder A beacon which on receiving electrical trigger, replies after a short fixed time delay (responder turnaround delay). A responder has the same function as a transponder, but is connect via a cable to receive the electric signal that commands the unit to transmit. Does not require an interrogator acoustic signal.

Pinger A transponder set to transmit at a fixed and regular interval.

A positioning system is thus based in a reception module which communicates with an seabed transponder. The latter emits with an acoustic signal, which is received on the reception module and processed. The signal is computed through some kind of CPU unit and the result exhibited on some kind of display unit, such as monitor.

Some acoustic positioning systems require relative range and direction observations to correct the range and bearing computed. As they are measured relatively to the reception platform's heading unit (usually a gyrocompass), and the reception platform may have suffered some pitch or roll, it must be corrected. For this purpose, some systems embed an IMU.

The module may also possess some kind of interrogator device, for constant communication with an element undersea. For producing an interrogator signal, which will make the undersea beacon respond, the acoustic positioning system can work as a pinger, responder, transponder, or transducer. A transponder requires a interrogator signal to respond to, which results in a continuing communication. In turn, the pinger works periodically. Both responder and transducer require an electric trigger. The transducer does not amplify the week incoming signal, and hence the system must be enhanced with an amplifier.

A comparison between the general architecture introduced for an acoustic position system and the functionalities intended from the MAST/AM project is now relevant. The final product of this project can be designated as a signal reception and processing module whose architecture follows the guidelines of a basic system exhibited herein. Additionally, it was likewise considered a system for signal interrogation, based on an interrogator transducer, which can be added to the architecture if desired.

The most widely used form of getting a signal from a target in tracking missions, in which the MAST/AM project can be included, is to insert a small transmitter in the target's body, which produces a continuous or coded omnidirectional signal, as well as some kind of identification. This tags are available commercially. It is important to stress that it has been due to the decrease of size of transmitters conjugated with an increase of reliability, that it has became possible to perform surveillance missions in smaller species. In this project, the desired signal is collected using hydrophones, which are microphones designed to be used underwater for listening or recording underwater sound. Most hydrophones are based on a piezoelectric transducer that generates electricity when subjected to a pressure change. Since sound is a pressure wave, transducers can convert a sound signal into a very small electrical energy that can then be amplified.

2.1.2 Position systems architecture

Based on [78], there are three primary types of acoustic positioning systems: Long Baseline (LBL), Short Baseline (SBL), and Ultra Short Baseline (USBL) or Super Short Baseline (SSBL), which will be defined next. These systems usually differ in the baseline size, which can be defined as the distance between the seabed transponders.

These primary types were purposely chosen as object of study, as they are the most commonly used, and therefore many case studies have been made, from which is possible to evaluate each acoustic system performance.

2.1.2.1 Ultra Short or Super Short Baseline

In a USBL or SSBL system (Fig. 2.2a) the vehicle has a multi-element receiver array that enables it to measure the angle as well as the range to an acoustic beacon. The system determines the bearing from the vehicle to the beacon by acquiring the signal emitted by the target and by measuring the TOA difference of a single sonar ping between two or more hydrophones. In

USBL systems, generally, the distance between hydrophones in the array is of the order of 10 cm.

One of the main advantages of this system, is, undoubtedly, low system complexity combined with a good range accuracy. Unfortunately, the USBL system also requires very careful installation, alignment, calibration and adjustment to ensure the measurements are accurate. As a consequence of these limitations, USBL is used in conjunction with attitude and heading sensors to maintain its positioning accuracy.

2.1.2.2 Short Baseline

As well as the USBL system, the SBL system (Fig. 2.2b) uses a single transponder underwater, hence also requiring a navigation system to provide a position that is earth referenced. Once more, beacon position is determined by measuring the relative arrival times at three or more mounted hydrophones in the reception module. The hydrophone units are usually deployed through tubes in the hull and are generally separated between 30 m and 50 m.

Likewise the USBL system, it presents low system complexity, making it an easy tool to use. However, both the large baseline and the careful calibration it requires constitute obstacles.

2.1.2.3 Long Baseline Baseline

LBL systems (Fig. 2.2c) take their name from the distance between seabed transponders or beacons which can be as much as several kilometers. In LBL navigation systems, an array of transponders is deployed and surveyed into position. The vehicle sends out an acoustic signal which is then returned by each beacon as it is received. Position is determined by measuring the travel time between the vehicle and each beacon, measuring or assuming the local sound speed profile, and knowing the geometry of the beacon array. With this information the relative distances between the vehicle and each array node can be calculated, by integrating the TOA measurements. Most LBL systems work at a frequency of approximately 10 kHz and provide position accuracy to within a few meters with a maximum range on the order of a few kilometers.

The main advantage of using a LBL method, is that it provides accurate local control and high repeatability. However, although this system does offer more information and precision, its high cost, deployment and calibration time-consuming procedures become prohibitive for low-cost operations.

2.1.2.4 Primary acoustic positioning system comparison

Table 2.1 displays a comparison of the primary acoustic positioning system regarding its advantages, disadvantages and errors. As one can see, the option regarding which acoustic positioning system to use depends heavily on the environment's conditions and mission's objectives.

For instance, LBL is the best option when working in a known perimeter and when accuracy is favored over cost and system complexity. This potential makes LBL systems the most used in work sites, where borders are defined and high accuracy and position stability are

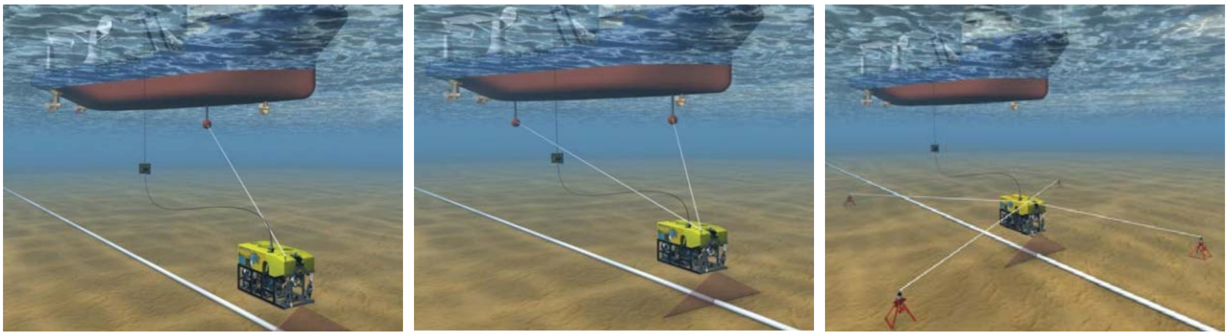

(a) USBL. Source:[10]. (b) SBL. Source: [10]. (c) LBL. Source: [10].

Figure 2.2: Primary types of acoustic positioning systems.

System	**USBL**	**SBL**	**LBL**
Advantages	Good potential accuracy Requires only a single subsea transponder One time calibration at installation	Accuracy dependent on an INS Multiple hydrophones required	Highest potential accuracy Accuracy preserved over wider operating area One hydrophone needed Redundant data for statistical testing/quality control Independent of platform motion and water depth
Disadvantages	Highest noise susceptibility Accuracy dependent on good calibration, INS accuracy and range	Accuracy dependent on INS accuracy Multiple hydrophones required	Area of operation limited to location of subsea reference beacons Requires multiple subsea/seabed transponders Update intervals long compared to SBL/USBL systems Need to redeploy and recalibrate at each site
Errors	Echo Range - timing errors Offset angles - phase detection errors Hydrophone Alignment - measurement errors Tilt Compensation - acceleration	Range and Offset Angles - Timing errors Platform Alignment - Measuring errors Calibration methods mitigate errors	Range - detecting timing errors Field calibration errors Ray bending problems increase as declination range increases

Table 2.1: Primary Acoustic Systems Comparison. Source: [78, 10].

required. Furthermore, this positioning system is independent of water depth.

SBL systems are preferred when such an accuracy, as the one provided by the LBL, is not necessary. With the former being less demanding, is possible to decrease costs and complexity, as it requires a single subsea transponder, and mostly calibration only upon installation, instead of continuously calibration as LBL calls for. However, it is necessary to resort to an inertial navigation system, for earth referenced position. For curiosity purposes, it is added that, as SBL positioning systems accuracy improves with hydrophone spacing, this system can achieve a precision and position accuracy similar of the LBL systems, when the spacing is commensurate to such an extend. Notwithstanding, this is achieved at the expense of a larger reception module (i.e. a vessel). Consequently, this option is considered fewer times, as the implementation of a new positioning system is far more obtainable than the acquisition and handling of a larger vessel. Likewise, a vessel which limits the transducer spacing, will, as well, limit the accuracy.

For the last option, the USBL, this is favored when low system complexity and consumed space constitutes a priority, as it entails the highest noise susceptibility and a more rigorous error handling process. Likewise the SBL, the USBL system requires a single calibration upon installation, being simple to operate afterwards. The fast deployment, less complex hardware and increasing performance of modern factory-calibrated USBL positioning devices makes it suitable for faster intervention missions.

The last comparison was well taken into account in the decision of which acoustic positioning to use in the MAST/AM project. From the very beginning, the MAST/AM project intended to employ an USBL system, as a preference over the remaining two. For validation, one must refer to the advantages of this system. Foremost, in the MAST/AM mission profile there is only one transmitter (tag inserted in the marine animal). By applying a system in which a single beacon is required, the mission can be performed anywhere the marine animal may be located. The last restrictions confines the options for acoustic positioning system to both USBL and SBL. Furthermore, the hydrophone array is to be attached at one end of the portable underwater tool. The SLB accuracy is directly connected with spacing between the multiple hydrophones. For a tool which is designed to be as compact as possible, accuracy would then be minimal. The acoustic positioning system whose properties better fits the mission's constraints is hence the USBL system, which is favored when low system complexity and space are a priority. Notwithstanding, resorting to an USBL system entails the highest noise susceptibility and a more rigorous error handling process. Additionally, it requires a INS with good accuracy.

2.1.3 Time of Arrival Calculation

The basic principle of all fine positioning systems is the same: triangulation and/or trilateration based on the TOA of a transmitter signal at three or more receivers. If the receivers are in three dimensions rather than a planar array, there dimensional positioning is feasible. At least three transducers are required, as two only describe a circumference in which the beacon may be, within a degree of certainty. With a third transducer, it is possible to calculate the distance in a third axis. A higher number of transducers will result in a better degree of certainty, but will also increase the system's complexity and cost. According to [61], TOA measuring with sufficient precision is not difficult as applicable algorithms are well known and seldom limit the accuracy with which position can be estimated. Consequently, the two most potential sources of error are:

- Level of synchronization between the clocks of the receivers.
- Accuracy to which one knows the actual position of the receivers.

The most commonly used method for TOA estimation is to put the received signal, starting from a relevant instant of time, through a matched filter [73]. The later maximizes the Signal to Noise Ration (SNR) of the filtered signal, which makes it an optimum method for the detection of signals in noise. In order to justify this premise, it must be taken into account that the system considers that it has detected a signal if the output of the filter is above a given threshold. Beneath this threshold everything is considered to be noise. The performance of the system is hence determined by this detection threshold, which is the lowest acceptable SNR at the output of the filter that will be considered a true signal [13]. Consequently, the better the SNR the better the performance of the system in differentiate a signal from noise.

The noise signal is considered Gaussian white noise. According to [1], when the input noise is white, the impulse response of the matched filter becomes:

$$h(t) = G_a s(t_1 - t), \tag{2.1}$$

where G_a is an arbitrary real positive constant, t_1 is the time of the peak signal output, and $s(t)$ is the signal emitted by the tag, sinusoidal, after traveling between the transmitter and the receptor. According to (2.1), the impulse response of the matched filter is obtained by inverting and advancing the received signal t_1 seconds in time. From the same equation, it can also be proved that the matched filter forms the cross correlation between the received signal corrupted by noise and a replica of the transmitted signal (see annex A for proof).

A visual representation of the implementation of a matched filter model is presented in Fig. 2.3.

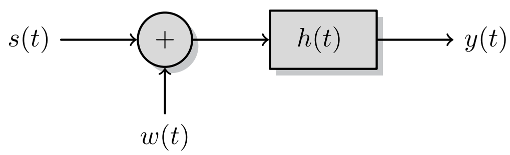

Figure 2.3: Match Filter Model.

The time of arrival is calculated by subtracting the duration of the signal from the time point when the matched filter response reaches its maximum value.

2.1.4 Time of Arrival Calculation of Sinusoidal Signal

TOA calculation is intended to be used on sinusoidal signals from VEMCO© tags. Unfortunately, this signal type presents difficulties in a successfully calculation of TOA. For prove, attention is called for Figs. 2.4a and 2.4b. The former displays the response of the matched filter to a sinusoidal input, with a pulse duration of $T = 2\,\mathrm{ms}$ and $f = 250\,\mathrm{kHz}$. The output has a form referred to as a “diamond”, with a clearly defined peak. However this form is only achieved in ideal conditions. Fig. 2.4b shows the response of the matched filter when Gaussian white noise and multipath are present. Multipath was simulated by adding a delayed and attenuated replica to the input of the matched filter. One can see that there is not a clear distinction between the peak in value of the matched filter response to the signal and the peak from the replica signal. Said effect decreases considerable the probability of success for TOA estimation.

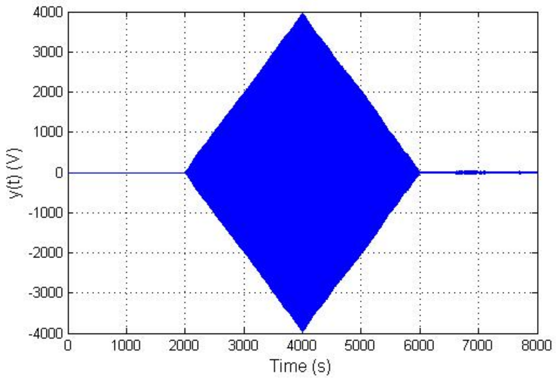

(a) Response of the matched filter to a sinusoidal input in ideal conditions.

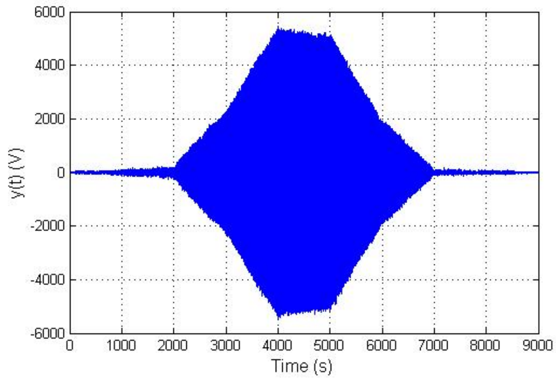

(b) Response of the matched filter to a sinusoidal input with noise and a delayed replica.

Figure 2.4: Response of a matched filter to a sinusoidal signal under ideal an non-ideal scenarios.

Following the results of a practical implementation, is now of added value to introduce a theoretical analysis. When a matched filter is used, the SNR at its output is:

$$SNR = \sqrt{\frac{2E}{n_0}}. \tag{2.2}$$

According to [13], the standard deviation of the TOA calculation is as follows:

$$\sigma_{TOA} \geqslant \frac{1}{\frac{1}{T} \times \sqrt{\frac{2E}{n_0}}} = \frac{1}{BW \times SNR}, \tag{2.3}$$

where BW is a measurement of bandwidth of the received signal, n_0 is the input noise spectrum level and E the energy of a signal $s(t)$ with pulse length T. E is equal to:.

$$E = \int_0^T s(t)^2 dt. \tag{2.4}$$

Based on (2.3), TOA standard deviation is strongly dependent on bandwidth as well as in SNR. Ideally, σ_{TOA} is a low value and hence BW and SNR value would preferably be a large value. The bandwidth increases by reducing the duration of the signal. However, for a sinusoidal signal, its energy is proportional to the amplitude of the pulse duration. Consequently, decreasing pulse duration would result in a lower SNR, contrary to what is desired. The use of a sinusoidal signal thus presupposes the contradiction that decreasing pulse duration to reduce bandwidth, in order to minimize σ_{TOA}, also results in a higher of SNR which increases σ_{TOA}. Analogously, decreasing SNR increases BW.

Taking into consideration the present section, it is safe to say that sinusoidal pulse detection has low rate of success in environments with high level of noise and multipath. Additionally, sinusoidal pulse transmissions usually requires great transmission power, resulting in a higher SNR, necessary due to its susceptibility to noise. Combined with weak results demonstrated in journeys over long distances, sinusoidal emitters are of poor reliability.

As mentioned before, the MAST/AM project is to be associated with VEMCO© sinusoidal tags. Looking at off-the-shell underwater emitters available nowadays, to the best knowledge of this thesis' author, small underwater transmitters are only associated with sinusoidal signals. Notwithstanding the difficulties ahead, experiments for the project will still be conducted with sinusoidal signals in order to estimate their reliability. However, as this thesis addresses tracking underwater, it must account for signals more likely to be successful. This topic will be resumed in section 2.2.

2.1.5 Direction of the transmitter

Finding the transmitter's direction is based upon the TOA calculation, which was introduced in section 2.1.3. In the present section, the TOA value measured will be denoted as t_{im}, in which $i = \{1{,}2{,}...{,}N_R\}$, N_R being the number of receptors. However, we must account for a margin of error, as this calculation is not flawless. Accordingly:

$$t_{im} = t_i + \epsilon, \tag{2.5}$$

where t_i is the correct TOA value and ϵ the error value.

For direction calculation a simple example will be used. In Fig. 2.5 one can see the position of two receptors, in plane xy of $\{B\}$ (the body reference frame), which have detected an transmitter signal wave. d is the direction of the transmitter and points in its direction, contrary to the signal propagation. In all three axis: $d = [d_x \quad d_y \quad d_z]^T$. The position of the receptors is written as: ${}^{B}p_m = [x_m \;\; y_m \;\; z_m]$, where $m = \{i{,}j\}$.

TDOA in both receptors is equal to the distance between them divided by the velocity at which the signal traveled. Mathematically:

$$v_p(t_i - t_j) = -(d_x(x_i - x_j) + d_y(y_i - y_j) + d_z(z_i - z_j)) = -d^T({}^{B}p_i -{}^{B} p_j), \tag{2.6}$$

where v_p is the propagation velocity of sound in water.

When considering N receptors, (2.6) becomes:

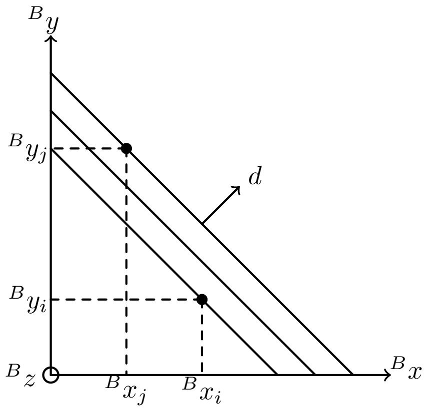

Figure 2.5: Direction of the transmitter

$$v_p\left[(t_1-k_2)\ (t_1-k_3)\dots(t_{N-1}-k_N)\right]^T = -d^T\left[({}^{B}p_1 - {}^{B}p_2)\ ({}^{B}p_1 - {}^{B}p_3)\dots({}^{B}p_{N-1} - {}^{B}p_N)\right]. \tag{2.7}$$

By considering $\triangle = \left[(t_1-k_2)(t_2-k_3)\dots(t_{N-1}-k_N)\right]^T$:

$$v_p\triangle = -d^T[x\ \ y\ \ z], \tag{2.8}$$

where:

$$x = \left[x_1 - x_2 \quad x_1 - x_3 \quad \dots \quad x_{N-1} - x_N\right], \tag{2.9a}$$

$$y = \left[y_1 - y_2 \quad y_1 - y_3 \quad \dots \quad y_{N-1} - y_N\right], \tag{2.9b}$$

$$z = \left[z_1 - z_2 \quad z_1 - z_3 \quad \dots \quad z_{N-1} - z_N\right]. \tag{2.9c}$$

Resolution of (2.9) is achieved by finding the solution which minimizes the mean-square error of:

$$J = \sum_{k=1}^{M}(d_x x_k + d_y y_k + d_z z_k + v_p\triangle_k)^2, \tag{2.10}$$

M being all possible combinations between two receptors, equal to ${}^{N}_{2}C$.

Solution of (2.10) can be found in [14]. The result is equal to:

$$d = -v_p\left[(P^TP)^{-1}M^T\right]\triangle, \tag{2.11}$$

where $P = [x\ \ y\ \ z]$ corresponds to the receptor array geometry, which is known.

2.1.6 Distance of the transmitter

In Fig 2.6, ρ corresponds to the transmitter's distance to the origin of $\{B\}$. Likewise Fig. 2.5, there are two receptors, i and j, in the xy plane. ρ_{ei} and ρ_{ej} are the distance from the transmitter to i and j, respectively. ρ_{oi} and ρ_{oj} indicate the distance between the receptors and the origin of $\{B\}$.

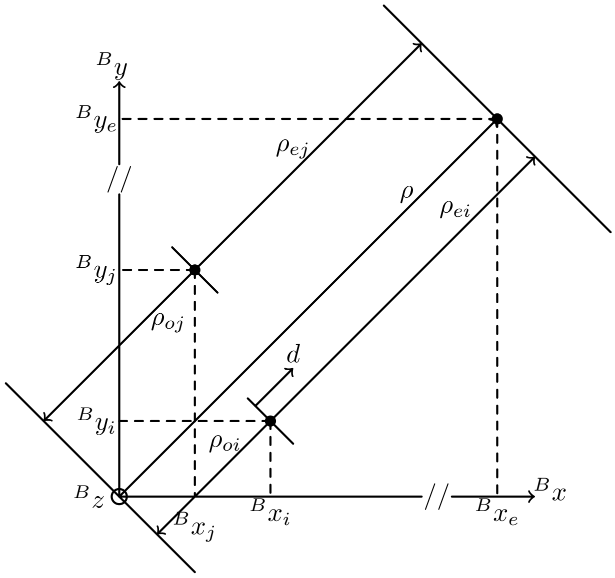

Figure 2.6: Distance of the transmitter.

ρ_k, of receptor k, can be estimated by adding ρ_{ok} and ρ_{ek}:

$$\rho = \rho_{ok} + \rho_{ek} = {}^B p_k^T d + v_p t_{km}, \tag{2.12}$$

where d is the direction of the transmitter, ${}^B p_k$ the position of the receptor in $\{B\}$, v_p is the propagation velocity of sound in water, and t_{km} the TOA value measured in said receptor.

Each receptor can then produce an estimate of the distance from the origin of $\{B\}$ to the transmitter. Finding the average value of the distance ρ_k, given by all the N receptors, helps reduce the estimation error:

$$\rho = \frac{1}{N} \sum_{k=1}^{N} ({}^B p_k^T d + v_p t_{km}) = \frac{1}{N} \sum_{k=1}^{N} \rho_k. \tag{2.13}$$

2.2 Real Time Processing and Advanced Signal Techniques

Recalling what was last introduced in section 2.1.4, it is now necessary to further analyze methods for error adjustment and accuracy improvement. The system performance depends on the accuracy of both the detection of the expected signal and the required processing. The signal may be distorted by additive noise and multipath propagation. In more hazardous acoustic environments, it becomes difficult to distinguish between the direct arrival and multipath interference, so rejection of outliers becomes a key issue. The implemented solution to reduce the possibility of error, is to resort to Spread-Spectrum (SS) methods for signal modulation.

Based on [66], spread spectrum methods are used in communication systems to provide low probability of interception in hostile environments, to provide multiple access capability in systems shared by many users, and to provide processing gain in channels where the transmitted signal is distorted by multipath propagation. This is a technique in which the signal is modulated using a sequence of digits (a spreading code or spreading sequence generated by pseudonoise, or pseudo-random number generator), for the purpose of transmitting the signal on a bandwidth considerably larger than the frequency content of the original information. During the transmission of the signal, it hops from frequency to frequency at fixed intervals. At each successive interval, a new carrier frequency is selected. Better SNR and immunity from various kinds of noise and multipath distortion is gained from the last operation. On the receiver end of the channel, the input signal is passed through a matched-filter whose impulse response is a time-reversed replica of the expected signal. Specially designed SS modulated signals have known good autocorrelation properties allowing for a sharper output of the matched-filter and improving the performance of the detector. Moreover, good cross-correlation properties can be obtained between several spread-spectrum signals allowing for a multi-user configuration in which several entities might be transmitting signals at the same time without interference [54].

The use of SS signals requires advanced signal processing techniques only available using real-time digital processing techniques. Real-time must be referenced as a system constraint, which dictates that said system has an operational deadline from receiving an event to producing a response to such event. Real-time response times are understood to be in the order of milliseconds and sometimes microseconds. A non-real-time system is one that cannot guarantee a response time in any situation.

The main purpose for real-time processing is for guaranteeing that if the received signal processing encounters some computing error, it does hold the processing unit responsible for signal analysis in this task, and makes sure an error in a single signal processing does not affect the acquisition and processing of following input signals. A real-time spectrum analyzer is able to sample the incoming RF spectrum in the time domain and convert the information to the frequency domain using the Fast Fourier Transform (FFT) [57], which is a computer algorithm used to rapidly converts time (or space) to frequency and vice versa. FFT's are processed in parallel with the spectrum sampling, meaning the analyzer does not lose incoming information due to being busy with FFT calculation.

For the MAST/AM project, a Digital Signal Processor (DSP) was chosen to be center of the acquisition and processing architecture in real-time. This element is a specialized microprocessor with an architecture optimized for the operational needs of digital signal processing. In this project, it performs acoustic signal detection using high-speed FFT. In its usage, the DSP becomes the core of the system, functioning as both system management and data processing.

In order to implement an acoustic signal acquisition and processing system, beyond a DSP, it is required a hydrophone set, a signal amplifier and an Analog-to-Digital Converter (ADC)

(Fig. 2.7). The signal amplifier is used to increase the power of the acoustic signal. Hereafter, the ADC converts the analog signal into digital signal which can then be sent to the digital processor.

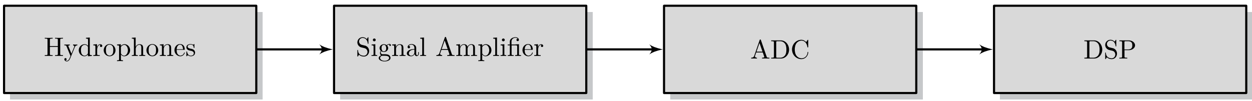

Figure 2.7: DSP based acoustic signal acquisition architecture.

3 | Navigation Systems

The implementation of navigation aid mechanisms is of common practice in missions involving autonomous vehicles, with the output of the previous system being directly applied in location estimation. Navigation algorithms involve various coordinate frames and the transformation of coordinates between them. For example, inertial sensors measure motion with respect to an inertial frame which is resolved in the host platform's body frame. This information is further transformed to a navigation frame. Since measured quantities are required to be transformed between various reference frames during the solution of navigation equations, it is of importance to introduce the concept of references frames and rotations between frames.

As previously observed in section 2.1.2, the USBL (section 2.1.2.1) and SBL (section 2.1.2.2) systems require an INS for earth reference position. The MAST/AM project employs an INS inside the portable underwater tool as a low-cost navigation system and consequently its study is regarded as relevant. The present section will start by reviewing basic mathematical techniques, without which comprehension of transformation of reference frames is not possible. Afterwards, Earth's surface representation methods will be addressed, followed by frames of reference and coordinate systems. Lastly, it will be introduced INS design and implementation.

3.1 Orientation Representation

In this thesis report, orientation will be represented according to [23], as represented in Fig 3.1. The unit vectors of coordinate system $\{A\}$, are denoted as $\hat{X}_A$, $\hat{Y}_A$ and $\hat{Z}_A$. ${}^{A}P$ symbolizes the position P in terms of frame $\{A\}$. In other words, P is represented in frame $\{A\}$.

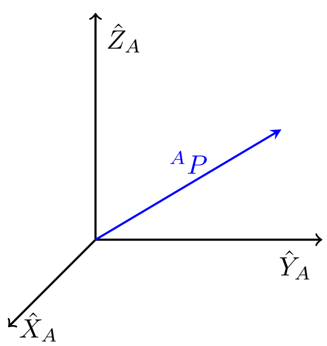

Figure 3.1: Vector relative to frame.

3.1.1 Rotation Matrix

A rotation matrix allows a conversion between frames of reference as it describes rotations of vectors. Unit vectors of frame $\{B\}$, written in terms of frame $\{A\}$, are called ${}^{A}\hat{X}_B$, ${}^{A}\hat{Y}_B$ and ${}^{A}\hat{Z}_B$. The rotation matrix for a transformation of a vector P , firstly in terms of frame $\{B\}$, to a second frame $\{A\}$, is represented as follows:

$$ {}^{A}_{B}R = \begin{bmatrix} {}^{A}\hat{X}_B & {}^{A}\hat{Y}_B & {}^{A}\hat{Z}_B \end{bmatrix} = \begin{bmatrix} r_{11} & r_{12} & r_{13} \\ r_{21} & r_{22} & r_{23} \\ r_{31} & r_{32} & r_{33} \end{bmatrix} = \begin{bmatrix} \hat{X}_B \cdot \hat{X}_A & \hat{Y}_B \cdot \hat{X}_A & \hat{Z}_B \cdot \hat{X}_A \\ \hat{X}_B \cdot \hat{Y}_A & \hat{Y}_B \cdot \hat{Y}_A & \hat{Z}_B \cdot \hat{Y}_A \\ \hat{X}_B \cdot \hat{Z}_A & \hat{Y}_B \cdot \hat{Z}_A & \hat{Z}_B \cdot \hat{Z}_A \end{bmatrix}, \tag{3.1} $$

where the last equality is obtained as each component of ${}^{A}_{B}R$ can be written as the dot product of a pair of unit vectors, as the components of any vector are the projections of that vector onto the unit directions of its reference frame.

Consequently, coordinates of a vector P, from frame $\{B\}$ to frame $\{A\}$, is noted as

$$ {}^{A}P = {}^{A}_{B}R\ {}^{B}P. \tag{3.2} $$

For reference, the dot product is, geometrically, the product of the magnitudes of the two vectors and the cosine of the angle between them. Consequently, the components of rotation matrices are often referred to as direction cosines.

Reviewing the last matrix from (3.1), one can see it is an orthogonal matrix, as it is a square matrix with real entries, whose columns and rows are orthogonal unit vectors. Equivalently, a matrix is orthogonal if its transpose is equal to its inverse. Hence, the rotation matrix from a frame $\{A\}$, to a frame $\{B\}$, is given by

$$ {}^{B}_{A}R = \left({}^{A}_{B}R\right)^{-1} = \left({}^{A}_{B}R\right)^{T}. \tag{3.3} $$

As the columns of ${}^{B}_{A}R$ are the unit vectors of $\{A\}$ written in $\{B\}$, the rows of ${}^{B}_{A}R$ are the unit vectors of $\{B\}$ written in $\{A\}$.

A transformation between frames can be expressed as products of intermediate transformations:

$$ {}^{U}_{D}R = {}^{U}_{A}R\ {}^{A}_{D}R. \tag{3.4} $$

The dynamics of the rotation matrix can be obtained by solving its limit:

$$ \frac{d{}^{A}_{B}R}{dt} = \lim_{\delta t \to 0} \frac{\delta {}^{A}_{B}R}{\delta t} = \lim_{\delta t \to 0} \frac{{}^{A}_{B}R\,(t+\delta t) - {}^{A}_{B}R\,(t)}{\delta t}, \tag{3.5} $$

where ${}^{A}_{B}R\,(t+\delta t)$ and ${}^{A}_{B}R$ are the matrix of direction cosines in the time instants t and $(t+\delta t)$, respectively. With respect to the first tranche, ${}^{A}_{B}R\,(t+\delta t)$, it can be written as:

$$ {}^{A}_{B}R\,(t+\delta t) = {}^{A}_{B}R\,(t)\,A(t)\,, \tag{3.6} $$

which corresponds to the multiplication of two matrices: the matrix of direction cosines at time instant t, and $A(t)$, the rotation matrix which relates, in frame $\{B\}$, time instants t and $(t+\delta t)$.

For small angles of rotation, $A(t)$ can be written as follows:

$$ A(t) = [I + \delta\Psi], \tag{3.7} $$

where I is a 3×3 unit matrix and

$$ \delta\psi = \begin{bmatrix} 0 & -\delta\psi & 0 \\ -\delta\psi & 0 & -\delta\psi \\ 0 & -\delta\psi & 0 \end{bmatrix}, \tag{3.8} $$

where $\delta\psi$, $\delta\theta$ and $\delta\phi$ represent infinitesimal angles according to which frame $\{B\}$ rotated, for a period of time equal to δt, about axes z, y and x, respectively. As δt approaches zero, the rotation matrix for infinitesimal angles becomes valid and the order of rotations is no longer is relevant.

By replacing ${}^{A}_{B}R\,(t+\delta t)$ in equation 3.5, by its value in equation 3.6, the following is obtained:

$$ \frac{d\,{}^{A}_{B}R}{dt} = {}^{A}_{B}R \lim_{\delta t \to 0} \frac{\delta\Psi}{\delta t}, \tag{3.9} $$

In the limit, when $\delta t \to 0$, $\frac{\delta\Psi}{\delta t}$ is the skew-symmetric matrix (matrix which satisfies the condition $-A = A^T$) of the angular velocity vector of frame $\{B\}$, in relation to frame $\{A\}$ $\left({}^{B}\left({}^{A}w_B\right) = [p,q,r]'\right)$, represented in $\{B\}$. Consequently:

$$ \lim_{\delta t \to 0} \frac{\delta\Psi}{\delta t} = \left[{}^{B}\left({}^{A}w_B\right)\times\right], \tag{3.10} $$

Replacing the value from equation 3.10, in equation 3.9, has the following result:

$$ \frac{\partial\,{}^{A}_{B}R}{\partial t} = {}^{A}_{B}\,R\left[{}^{B}\left({}^{A}w_B\right)\times\right]. \tag{3.11} $$

where

$$ \left[{}^{B}\left({}^{A}w_B\right)\times\right] = \begin{bmatrix} 0 & -r & q \\ r & 0 & -p \\ -q & p & 0 \end{bmatrix}. \tag{3.12} $$

3.1.2 Euler angles

The previously mentioned rotation matrix's entries follow from the conventional Euler angles. In consequence it is of importance to define such notation.

The Euler angles were created by Leonhard Euler ($1707-1783$) to describe the orientation of a rigid body. In this representation, each rotation is performed about an axis of a moving system $\{B\}$ rather than one of a fixed reference $\{A\}$. It can be seen as a frame rotating from its initial orientation in order to reach the current orientation. The orientation of each angle is changed after each rotation, and the following rotation its always made in reference to the current orientation.

There are many different conventions of Euler angles. Although, all conventions are the result of three consecutive rotations about three axis, they vary on the choice of rotational axis. The most common convention is the $z-x-z$ (initially defined for gyroscopes). Another common convention is the $z-y-x$ convention, the so called yaw, pitch, and roll Euler angles representing the angles of three successive rotations about the z, y, and x body-fixed axis. The latter will be the convention employed in this thesis. Visual representation of this notation is displayed in Fig. 3.2, in which is visible the variation from frame $\{A\}$ to frame $\{B\}$ caused by each rotation. Bear in mind, for example, that in case of an Roll rotation the x axis remains in the same position from $\{A\}$ to $\{B\}$. The same does not happen with axis y and z. A roll rotation causes $\hat{Y}$ to rotate into $\hat{Y}'$ and $\hat{Z}$ into $\hat{Z}'$. The axis wherein the rotation is effected, does not rotate. Also, each rotation takes place about an axis whose location depends upon the preceding rotations. To be noted that this convention has homogeneous Matrix and angles identical to the yaw, pitch and roll convention. These refer to rotations about the z, y and x axis, respectively, of the moving frame.

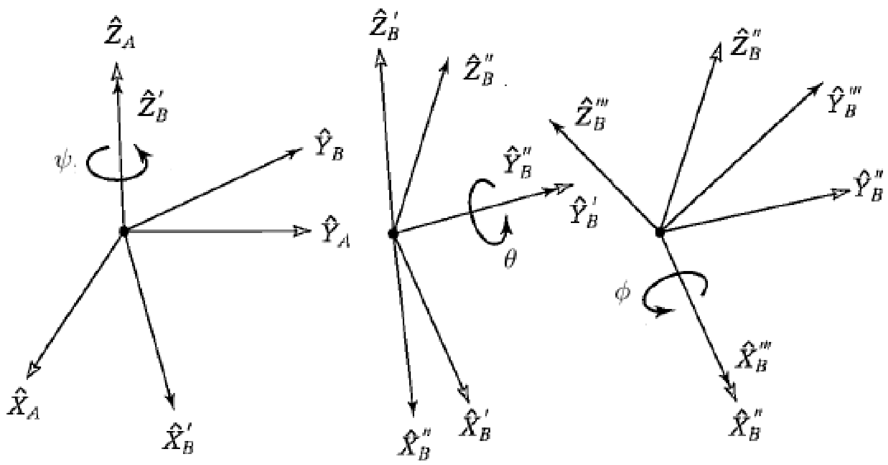

Figure 3.2: Euler angles. $z-y-x$ convention (ψ - Yaw; θ - Pitch; $\phi - Roll$). Source: [23].

With reference to figure 3.2, rotation from frame $\{A\}$ to $\{B\}$ can be obtained by multiplying the three intermediate frames:

$$ {}^{B'''}_{A}R = {}^{B'''}_{B''}R \; {}^{B''}_{B'}R \; {}^{B}_{A}R. \tag{3.13} $$

The right-hand side of equation 3.13 can be calculated using the rotation angles:

$$ {}^{B'''}_{A}R = \begin{bmatrix} c\psi & -s\psi & 0 \\ s\psi & c\psi & 0 \\ 0 & 0 & 1 \end{bmatrix} \begin{bmatrix} c\theta & 0 & s\theta \\ 0 & 1 & 0 \\ -s\theta & 0 & c\theta \end{bmatrix} \begin{bmatrix} 1 & 0 & 0 \\ 0 & c\phi & -s\phi \\ 0 & s\phi & c\phi \end{bmatrix}, \tag{3.14} $$

where $c \equiv \cos$ and $s \equiv \sin$. Multiplying the right-hand-side of equation 3.14, the following result is obtained:

$$ {}^{B'''}_{A}R = \begin{bmatrix} c\psi c\theta & c\psi s\theta s\phi - s\psi c\phi & c\psi s\theta c\phi + s\psi s\phi \\ s\psi c\theta & s\psi s\theta s\phi + c\psi c\phi & s\psi s\theta c\phi - c\psi s\phi \\ -s\psi & c\theta s\phi & c\theta c\phi \end{bmatrix}. \tag{3.15} $$

The solution for extracting the rotational angles from a rotation matrix begins with considering a generic rotation matrix:

$$ {}^{B'''}_{A}R = \begin{bmatrix} r_{11} & r_{12} & r_{13} \\ r_{21} & r_{22} & r_{23} \\ r_{31} & r_{32} & r_{33} \end{bmatrix}, \tag{3.16} $$

then, equaling the equations 3.15 and 3.16, if $\cos\theta \neq 0$:

$$ \begin{aligned} \theta &= Atan2\left(-r_{31}, \sqrt{r_{11}^2 + r_{21}^2}\right) \\ \psi &= Atan2\left(\frac{r_{21}}{c\theta}, \frac{r_{11}}{c\theta}\right) \\ \phi &= Atan2\left(\frac{r_{32}}{c\theta}, \frac{r_{33}}{c\theta}\right) \end{aligned} \tag{3.17} $$

where $Atan2(x{,}y)$ is a two-argument arc tangent function.

In equation 3.17, it is always computed the single solution for which $\theta \in]-\frac{\pi}{2}, \frac{\pi}{2}[$. Also, as mentioned above, there is a singularity for $\theta = \pm\frac{\pi}{2}$. One possible convention, as specified in [23], is to choose $\psi = 0$, with the following result:

$$ \begin{cases} \theta = \frac{\pi}{2} \\ \psi = 0 \\ \phi = Atan2(r_{21}{,}r_{22}) \end{cases} \qquad \begin{cases} \theta = -\frac{\pi}{2} \\ \psi = 0 \\ \phi = -Atan2(r_{21}{,}r_{22}) \end{cases} $$

3.2 Earth Surface Model

Earth surface is not easily defined by a single model, as it has several variations. Until now, the standard has been to resource to one of two principal Earth's surface modulation models, depending on the purpose for which the results will be used. Both will be defined in this section, serving as a knowledge base for the subsequent definition of reference systems.

3.2.1 Earth's gravity and Centrifugal Force

A first study in both Earth's gravitation and centrifugal force is of importance in order to fully understand the topics of Earth's surface modulation, as both elements have a strong influence in Earth's shape.

The present notion of gravity comes from the Newtonian law of universal gravitation, which states every mass attracts other point of mass with a force, F, equal to:

$$|\vec{F}| = mg, \tag{3.18}$$

m being the mass on which the force is applied and g as follows:

$$g = \frac{GM}{r^2}, \tag{3.19}$$

where G represents the universal gravitational constant, M the mass of the object which is attracting, and r the separation between both masses.

If every mass object is subject to the gravitation force, every object has a gravitational potential energy. This potential force is converted into kinetic energy, when the object is moving, result of a gravitational force being applied on it. But when the object is not moving, it is the result of another force contradicting the gravitational force, for example resistance by a surface where the object was placed. But this object is still being subjected to the gravitational force, and consequently has a potential energy which depends on its high (h):

$$\triangle V = mgh. \tag{3.20}$$

Mathematically, this potencial energy is the derivative of the force being applied with respect to a distance s:

$$F = -\frac{dV}{ds}. \tag{3.21}$$

In three dimensions, the force is equal to the gradient of this energy:

$$F = -\vec{\triangle} V. \tag{3.22}$$

According to the Newton law, all things attract each other due to the force of gravity, and this is the reason why planets and starts stay together. The law also states this is the reason why their shape is almost sphere. If gravity was the only force involved, their form would be spherical, as the body is a very tick fluid and modulates according the lowest energy shape.

However, most planets rotate, thus the additional presence of a rotational force. Consequently, its shape differs from a perfect sphere.

Earth is influenced by the previously defined rotational effect. A mass undergoing curved motion constantly accelerates toward the axis of rotation. This centripetal acceleration is provided by a centripetal force, which is exerted on the mass by some other object. In accordance with Newton's Third Law of Motion, the mass exerts an equal and opposite force on the object. This is the reactive centrifugal force. It is directed away from the center of rotation, and is exerted by the rotating mass on the object that originates the centripetal acceleration. The latter is defined as follows:

$$a_c = w^2 p, \tag{3.23}$$

where w is the Earth's angular frequency and p is the distance from the spin axis to the surface. The latter will be a function of latitude, and consequently, the centrifugal acceleration is also a function of latitude. The Earth is, thus, not perfectly sphere, as this centrifugal acceleration will vary according to the latitude.

This spin axis, represented by p in (3.23), is a straight line between the North Pole and the South Pole. In both, the axis encounters the surface, resulting in $p = 0$. Additional, p takes its maximum value at the equator, where the surface has the greatest distance from the axis. Consequently, the centrifugal acceleration is maximum at the equator and zero at the poles.

At the equator, p equals the radius of the earth $r_{\oplus}$, about 6378 km. At the poles $r = 0$, as the axis meets the surface. As a result:

$$\begin{aligned} a_{c_{equator}} &= \frac{2\pi}{T_{\oplus}} r_{\oplus} = 3.39\,\mathrm{cm/s^2} \\ a_{c_{poles}} &= 0 \end{aligned} \tag{3.24}$$

$T_{\oplus}$ being the Earth's rotation period, equal to 86,164 s.

As response to the centrifugal force, Earth dilates at the equator, taking up a shape more resemblant of an ellipse rotating about the spin axis, than that of a sphere.

The total force of Earth's gravity can be expressed as follows:

$$U = V + \frac{1}{2} w^2 p^2. \tag{3.25}$$

3.2.2 The Ellipsoid

Before the emergence of the ellipsoid model, the Earth was represented by a spherical model. However, the latter was a misconceive, as the actual shape of Earth is not round. A spherical model would have an acceptable amount of success for cases of short-range navigation, whereas for medium and long rang navigation, there was a need to creat a more reliable characterization of Earth. Analyzing the shape of the earth, it is observed that it diverges from a sphere due to a slight flattening at the poles, a difference of about 20 km between the average equatorial and the polar radius, and a small protuberance at the equator. Therefore, the earth better resembles an ellipsoid of revolution.

The ellipsoid is a level surface of constant U, introduced in (3.25). Gravity acceleration, g, is not constant. It is generated by the gradient in U. For this model, the surface gravity is a function of latitude.

Different mathematical models for the ellipsoid have been applied in different parts of the planet. All of them are defined by the same mathematical expressions, but differ in the parameters values. Visual representation of ellipsoid is shown in Fig. 3.3a, where a represents semi-major axis, and b the semi-minor axis.

Ellipsoid models are defined by their semi-major axis, a, and flattening, f. The latter is expressed as follows:

$$f = \frac{a-b}{a}. \tag{3.26}$$

Other parameters, such as first eccentricity (e) and second eccentricity (e'), can also be used to describe a reference ellipsoid:

$$\begin{aligned} e &= \sqrt{1-\frac{b^2}{a^2}} = \sqrt{1-(1-f)^2} \\ e' &= \sqrt{\frac{b^2}{a^2}-1} = \frac{e}{1-f}. \end{aligned} \tag{3.27}$$

3.2.3 The Geoid

The geoid is a model for the Earth's surface where the gravity potential is equal in every point of the surface, and the direction of the gravity is always perpendicular. The direction of gravity being perpendicular to the geoid is of great importance as optical instruments containing level devices are often used in geodetic measurements. When correctly calibrated, the vertical axis of the instrument coincides with the direction of gravity, and is perpendicular to the geoid.

The geoid specifies the surface level the ocean would take upon the entire earth if it were free to adjust to the combined effect of the attraction force from the Earth's mass force and Earth's centrifugal force. As the Earth's mass is uneven distributed, the geoid surface is irregular (as can be seen in Fig. 3.3b), and, consequently, the geoid and ellipsoid do not coincide. The variation between ellipsoid an geoid can vary up to ± 100 m. A visual example of the latter difference can be seen on Fig. 3.4, where L_1 and L_2 are the astronomic latitude and the geodetic latitude, respectively. The angle between the line perpendicular to the geoid and the line perpendicular to the ellipsoid is called the "deflection of the vertical".

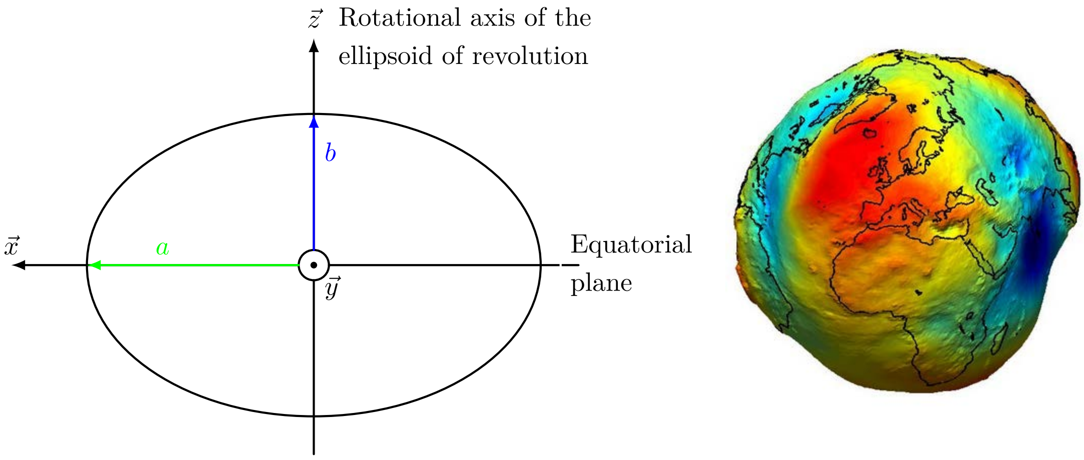

(a) Ellipsoid. (b) Geoid. Source: [80].

Figure 3.3: Ellipsoid and Geoid representation.

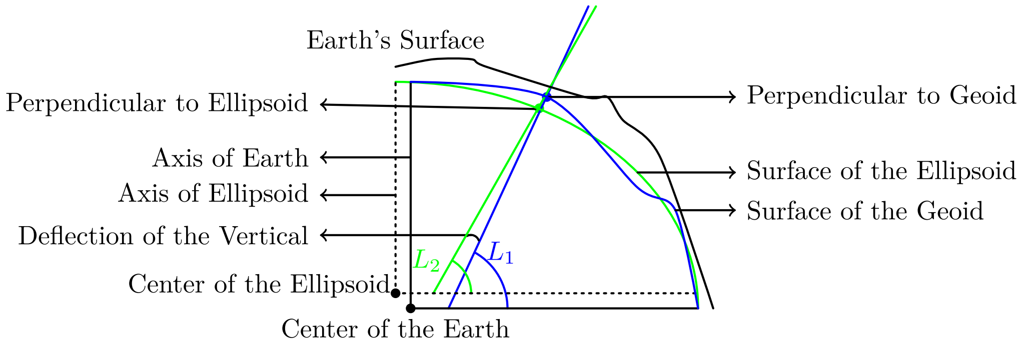

Figure 3.4: Representation of the Earth's, Geoid's and Ellipsoid's surface.

3.3 Reference Systems

The present section will introduce both reference frame and coordinate system. Foremost, is of importance to clearly establish a differentiation between the two. According to [69, 41], although sometimes they might be used as synonymously, there is a slight difference. Whereas, changes from one coordinate system to another may not involve change of time, transformation from one frame of reference to another must include change in time. Hence, the frame of reference includes all the coordinate systems at rest with respect to any particular systems.

3.3.1 Inertial Frame

An Inertial frame is a frame where Newton Laws apply. In such a frame, an object is observed to have no acceleration when no forces are acting on it. If a reference frame moves with constant velocity relative to an inertial reference frame, it is also an inertial reference frame. All inertial frames are in a state of constant, rectilinear motion with respect to one another. An accelerometer moving with any of them would detect zero acceleration. The origin of an Inertial frame as well as the direction of its three orthogonal axis is arbitrary.

The Earth Centered Inertial (ECI) is noted as $\{I\}$. It has its origin at Earth's center of Mass. The $x-y$ plane coincides with the Earth's equatorial plane. The x axis point from Earth to the Sun at the vernal equinox. The z axis lies at a 90° to the equatorial plane and extends through the true North Pole. The y axis is simply chosen to conform to a right hand coordinate system. The ECI Coordinate system does not rotate with the Earth. Strictly, this is not a true inertial frame, as the Earth experiences acceleration in its orbit around the Sun, its spin axis slowly moves, and the Galaxy rotates. However, it is a sufficiently accurate approximation to an Inertial frame for navigation purposes. It can be consider as an Inertial Frame for the MAST/AM project, as when no force is applied to the tool it remains fixed with respect to the surface of the Earth.

In the MAST/AM project, $\{I\}$ serves as a global reference for the sub-aquatic domain, and typically it will be solidary with a buoy at the surface. The centre of the buoy accommodates the origin of that frame. However, $\{I\}$ is not exactly an inertial frame as the buoy is subject to the movement of the waves and, hence, it is allowed to rotate, but for the given speeds and accelerations, one can assume it as an inertial one. If one were to be faithful to its traditional designation, this system would be considered a Vechicle-carried North/East/Down (NED) frame. The latter will be defined following.

3.3.2 NED frame

NED is locally defined in relation to the geoid. The origin moves with the vehicle and is defined as the projection of the origin of the vehicle in the ellipsoid. The x axis points towards the ellipsoid north (geodetic north). The y axis points towards the ellipsoid east (geodetic east). The z axis points downward along the ellipsoid normal. Refer to Fig. 3.5a for visual representation, where λ is the longitude.

The origin of this frame moves with the vehicle and the axes directions vary with respect to the vehicle's movement. Consequently, NED is not an Inertial frame.

The local navigation frame is important in navigation because the user wants to know their attitude relative to the north, east, and down directions. For position and velocity, it provides a convenient set of resolving axes, but is not used as a reference frame [38]. A major drawback of the local navigation frame is that there is a singularity at each pole because the north and east axes are undefined there. Thus, navigation equations mechanized using this frame are unsuitable for use near the poles.

3.3.3 Body Frame

The body frame is fixed with respect to the tool. The origin is located at the center of gravity of the tool. The x axis points forward, lying in the symmetric plane of the tool. The y axis points to the right side of the tool and, lastly, the z axis points downward to comply to the right-hand rule. For angular motion, the x-axis is the roll axis, the y-axis is the pitch axis, and the z-axis is the yaw axis. Hence, the axes of the body frame are sometimes known as roll, pitch, and yaw. In this project, the Body Frame will be noted as $\{B\}$. $\{B\}$ is able to rotate, as a direct consequence of the diver's orientation. Visual representation can be found in Fig. 3.5b.

The body frame is essential in navigation because it describes the object that is navigating. All strapdown inertial sensors measure the motion of the body frame (with respect to a generic inertial frame) [38].

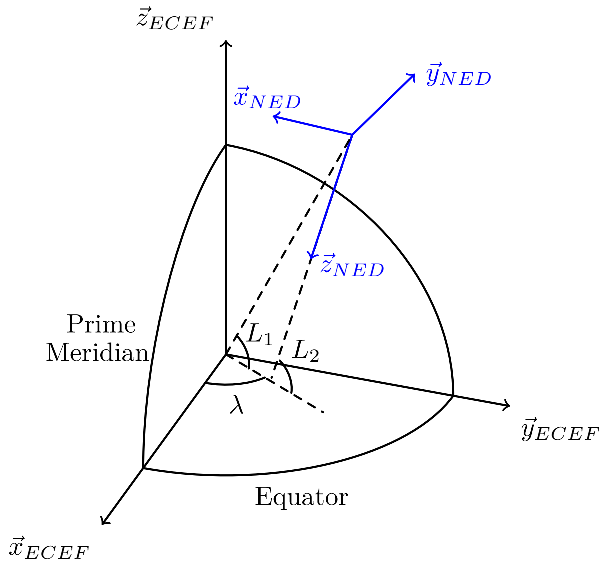

(a) NED.

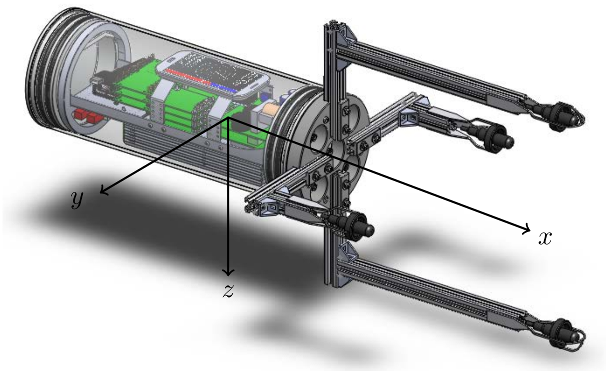

(b) Body Frame.

Figure 3.5: NED and Body Frame representation.

3.4 Inertial Navigation

A brief definition of an inertial navigation can consist on a system in which measurements by accelerometers and gyroscopes are used to track the position and orientation of a moving body, relatively to a known starting point, orientation and velocity. An INS consists on a IMU, instrument supporting electronics and some type of navigation processing unit.

The resort to inertial navigation has largely increased in the last decade, for the most part due to the development of the Microelectromechanical systems (MEMS) technology, which enabled the use of compact and lightweighted inertial sensors. Inertial navigation is now used in various applications related with aerial and nautical navigation. Before the onset of the MEMS technology, the resource to inertial navigation systems was limited to the usage of large and heavy inertial sensors.

From the previous statements, one can rapidly foresight recent studies and progresses made upon inertial navigation have resorted to MEMS sensors. Thus, the latter will be a constant presence in the following analysis. MEMS is a technology that can be defined as miniaturized mechanical and electro-mechanical elements that are made using techniques of microfabrication. This mainly entails structures, sensors, actuators, and microelectronics, which can all be merged onto a common silicon substrate along with integrated circuits. The most remarkable elements are the microsensors and microactuators, which are categorized as transducers. The main purpose of this technology was precisely the fabrication of small sensor devices, combined with small cost and consumption. This has enabled the resort to inertial navigation systems in applications heretofore impossible, due to high cost (expensive manufacturing, calibration and testing requirements), size and weight of conventional navigation devices. This technology has direct implications in the MAST/AM project, as otherwise a compact tool with an inertial navigation aid system would not be possible.

3.5 Inertial System Configurations

In a INS platform, the accelerometers are mounted on a platform which is connected to the INS casing by rotatable frames, known as gimbals (Fig. 3.6). At least three gimbals are required to isolate a subsystem from host vehicle rotations about three axis. The gyros may be mounted on the platform or at the gimbal axes. Each gyro outputs the angle through it has been rotated which corresponds the rotation of the host vehicle. These outputs are used to drive the gimbal rotation to keep the platform aligned with the reference frame as the host vehicle maneuvers. At initialization, the platform has to be rotated to physically align it with the reference frame axes.

As the accelerometer body frame is kept aligned with the reference frame, the velocity and position may be updated without the need to update the attitude or transform the specific force. This platform configuration also minimizes the effect of instrument errors excited by host vehicle maneuvers.

Based on [79], there are two basic types of INSs: stable platform and strapdown. There are defined following.

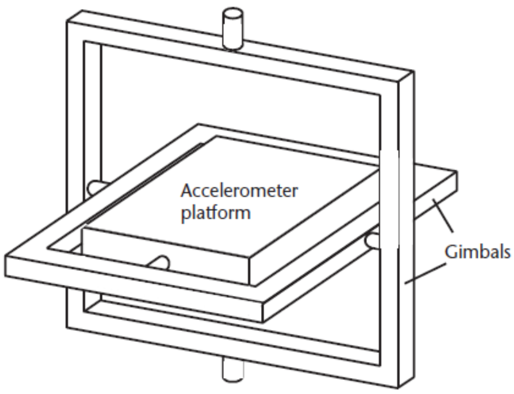

Figure 3.6: Gimbaled platform INS. Source: [38].

Stable Platform Systems In a stable platform system, the inertial sensors are set up in a stationary platform, which is mounted in a system of platform gimbals. The platform is free in all three axis, or, in other words, mechanically isolated from the rotational motion of the vehicle. For orientation estimation the angles between adjacent gimbals are read. For the device's velocity, the output of the accelerometers is integrated. Velocity, in turn, is integrated in order to obtain position. Knowing initial velocity and position, this data can be converted into distance and heading traveled. However, it is necessary to subtract vertical acceleration resulting from the gravity acceleration. The gyroscopes detect platform rotations. A visual representation is displayed in Fig. 3.7.

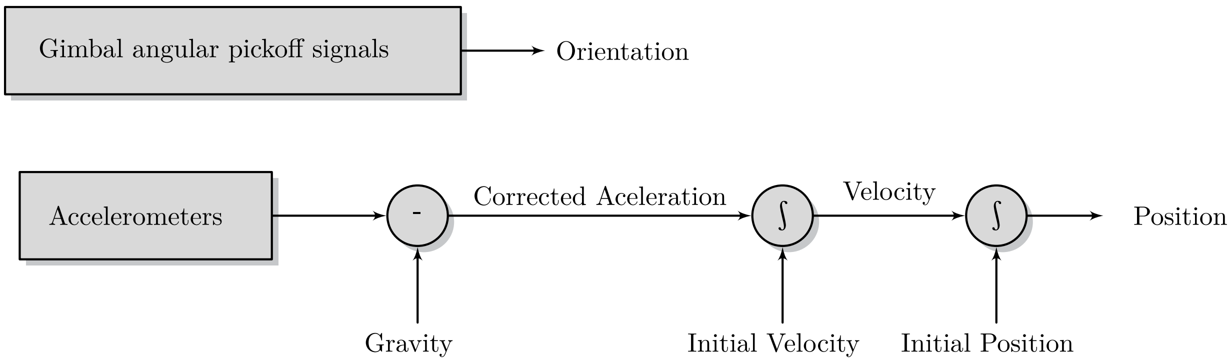

Figure 3.7: Navigation algorithm for a stable platform system.

Strapdown Systems In a strapdown system, sensor's outputs are measured in a body frame, as the inertial sensors are mounted on the platform and not at the gimbal axes. For orientation estimation, the gyroscope output is integrated. This orientation is then used to transform the accelerometers outputs from body frame to the reference frame in which the gyro made its measurements. Afterwards, the resulting signal is integrated in order to obtain velocity, which is, posteriorly, integrated for position. Once again, by knowing initial velocity and position, this data can be converted into distance and heading traveled. A visual representation is displayed in Fig. 3.8.

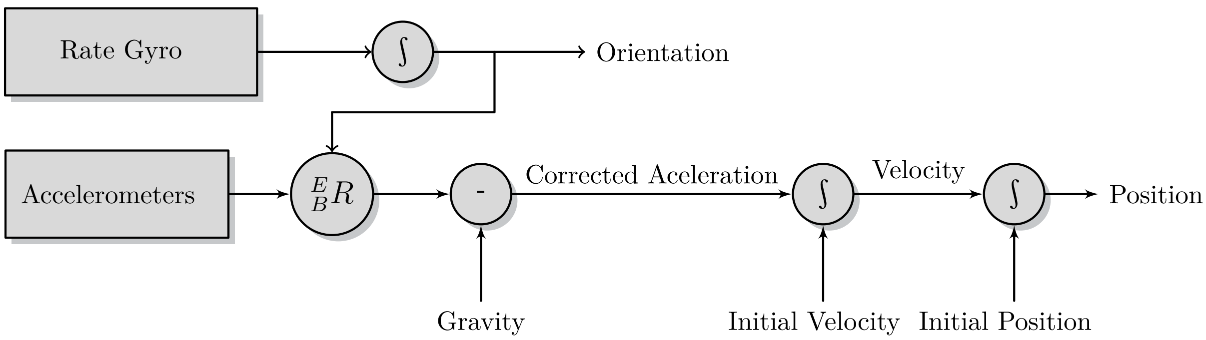

Figure 3.8: Navigation algorithm for a strapdown system.

In comparing the two systems previously expressed, a strapdown INS platform is somewhat preferable. It is smaller, mechanically simpler, and lighter than its platform equivalents, so is much cheaper to manufacture. Nevertheless it has the disadvantaged of computational complexity, and error building. An error in the rotation between frames affects directly the result of the position estimation. However, INS has followed a path for preferring computation complexity when conjugated with the most compact option as, nowadays, processor load is no longer a problem [38]. Platform INS are discussed in more detail in [45, 70].

3.5.1 Overview of Inertial Sensors

In the present section, sensors composing of the IMU will be analyzed in order to fully understand their behavior in orientation and position estimation.

3.5.1.1 Gyroscope

Gyroscopes are used to measure an object's orientation in three-dimensional space. Mechanically, a gyroscope is a spinning wheel mounted on three gimbals which allow the wheel to rotate in all three axes. Physically, a gyroscope is based on the principal of conservation of angular momentum, which states that the spinning wheel will resist changes in orientation. A wheel is used because disk shaped objects have large values of angular momentum, and are, consequently, more resistant to angular displacement. Theoretically, the wheel could spin forever, however, in reality it is not possible due to friction between mechanical parts. Consequently, a rotor must be used in order to keep the wheel spinning. When the gyroscope is subjected to a rotation, the wheel remains in a same attitude with an inertial frame forcing the gimbals to rotate. The orientation of the device is then obtained by measuring angles between adjacent gimbals. Older mechanical gyroscopes had notches on the gimbals to physically make measurements, whereas newer models use lasers to determine separation distance between rings, which can be translated into angles.

A mechanical gyroscope can be said to be of easy use, although its design is rather difficult to build. The main disadvantage of a mechanical gyroscope is the drift over time, consequence of the friction between the gimbals. Additionally, it requires a high energy input for the rotor. The latter, conjugated with the cost of high maintenances, makes an mechanical gyroscope quite expensive.

A MEMS gyroscope presents an important difference to a typical mechanical gyroscope. It does not measure orientation. Instead it measures angular velocity. Consequently, before proceeding with an analysis of the MEMS gyroscope, is of interest a brief definition of angular velocity, and posteriorly, of the Coriolis Force, concept whose knowledge will be necessary afterwards.

Angular velocity specifies the rotation speed of an object and the axis about which the object is rotating. In three dimensions, the angular velocity, $\vec{w}$, is a vector with a magnitude equal to the angular speed and with a direction which describes the axis of rotation. It is represented as follows:

$$\vec{w} = \frac{d\theta}{dt}\vec{u}, \tag{3.28}$$

where θ is the angle of the object regarding the axis of rotation, and $\vec{u}$ an unitary vector over the instantaneous rotation axis.

With respect to the Coriolis force, it can be considered to be a deflection of a moving object observed in a rotating reference frame. The existence of the latter is essential for the occurrence of the Coriolis effect. When an object is vibrating, it naturally tends to continue vibrating in the same plane. If this object is rotated while vibrating it will begin to oscillate outside of the plane of the original vibration. This effect is known as the Coriolis Effect. The Coriolis force acts only when the device is rotating, therefore gyroscopes measure only angular velocity, or the speed at which the device is rotating. When the device is stationary, regardless of which direction the device is pointing, all three axis of the gyroscope will measure zero. The Coriolis force, F_C, is defined as follows:

$$F_C = -2m(w \times v), \tag{3.29}$$

where m is the mass of the object, w the angular velocity, and v the velocity of the object in the rotating frame.

According to [2], majority of the micromachined gyroscopes use vibrating mechanical elements to sense angular rate by sensing the Coriolis accelerations in a vibration proof-mass system. Vibrating gyroscopes must be driven at resonance in order to function as angular rate sensors. This direction will be referred to as the drive direction. When the gyroscope is rotated along the rotation axis, a sinusoidal Coriolis Force is induced in the direction orthogonal to both the drive direction and the angular rotation axis. This direction will be called the sense direction (Fig. 3.9). The sense and drive direction can be viewed as a mass-spring damper system. As a consequence, a gyroscope can be viewed as a two degrees-of-freedom mass-spring-damper system: one degree of freedom in the driver direction, and the second in the sense direction (orthogonal to the first). One of the advantages of this system is that it is not affected by friction or wear, as it does not involve rotating parts.

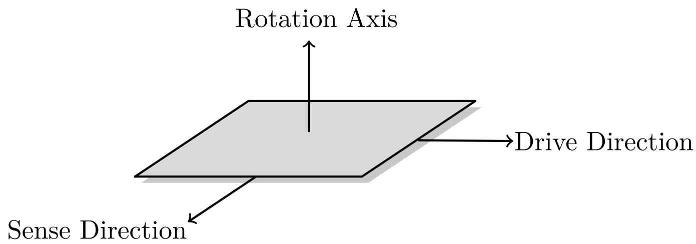

Figure 3.9: Model of a micromachined gyroscope.

The MEMS gyroscopes have the advantage of being of an extremely small size, inexpensive and not requiring much energy. However, they lose in terms of accuracy when compared to traditional gyroscopes.

3.5.1.2 Accelerometer

An accelerometer is an electromechanical device which measures the physical acceleration experienced by an object due to inertial forces or due to mechanical excitation. Mechanically, the accelerometer features a mass attached to a spring, and when the mass system is subjected to linear acceleration, a force equal to mass times acceleration causes it to deflect. The mass is hence displaced in the frame of reference of the accelerometer device. The acceleration is estimated by measuring said displacement, which is in turn measured by transforming this motion into an electric signal, resorting to devices such as piezoelectric and capacitive components. In most cases the system also includes a dashpot to provide a desirable damping effect. This dashpot is normally attached to the mass in parallel with the spring.

To compute the motion of the mass Newton's second law is used, where all real forces acting on the mass are equal to the inertia force on mass. Consequently, this dynamic problem can be treated as a static equilibrium problem and the equation of motion can be obtained by resorting to the following equation of equilibrium:

$$F_{applied} = F_{damping} + F_{spring} + m\ddot{x}, \tag{3.30}$$

where F represents the force applied in the different situations, m the mass attached to the string, and $\ddot{x}$ the acceleration upon the mass. As all the summation of all forces applied in the mass is equal to zero, $F_{applied} = 0$.

(3.30) can be transformed in the following:

$$m\ddot{x} + kx + c\dot{x} = 0, \tag{3.31}$$

where x is the mass displacement in the frame of reference of the accelerometer device, k is the spring constant, c is the damping coefficient and $\dot{x}$ is the velocity of the mass. The equation of motion is hence a second order linear differential equation with constant coefficients.

Relating (3.31) with the second-order differential equation:

$$\frac{d^2x}{dt^2} + 2\xi w_0 \frac{dx}{dt} + w_0^2 x = 0, \tag{3.32}$$

where w_0 is the undamped angular frequency of the oscillator and ξ is a constant called the damping ratio, the following result is obtained:

$$\begin{aligned} w_0 &= \sqrt{\frac{k}{m}} \\ \xi &= \frac{c}{2}\sqrt{km}. \end{aligned} \tag{3.33}$$

If the acceleration is steady and the mass displacement is steady, meaning any initial transient has died away, $w = 0$. Consequently:

$$m\ddot{x} = -kx, \tag{3.34}$$

that is, the inertia force is balanced by the opposite spring force, and x is a measure of the acceleration [48]. The scale factor will be $\frac{m}{k}$.

In case of dynamic performance, it is easier to consider the Laplace transformation:

$$\frac{x(s)}{a(s)} = \frac{1}{s^2 + \frac{c}{m}s + \frac{k}{m}}. \tag{3.35}$$

The sensor response is determined by damping present in the system. ξ between 0.6 to 1.2 results in high responde time, fast settling time, good bandwidth and linearity.

An accelerometer at rest on the surface of the Earth will measure an acceleration equal to g upwards, due to its weight. Consequently, an accelerometer measures both the force of gravity and linear acceleration. In free-fall, an accelerometer reports zero acceleration, as the both the mass and frame suffer the same acceleration, thus not deforming the spring.

Typical MEMS accelerometers are composed of movable proof mass with plates that are attached through a mechanical suspension system to a reference frame [5]. Movable plates and fixed outer plates representing capacitors are inserted. The deflection of proof mass is measured using the capacitance difference, between the movable plate and the fixed plates.

3.6 Earth's magnetic field

Magnetometer's output signals will be used in the MAST/AM project for attitude correction. It is then of importance to analyze Earth's magnetic field leading up to the functioning of a magnetometer. Magnetometers are used as an aiding sensor for INS. They allow for accurate attitude estimation by comparing the magnetic field vector observed in body frame, with the vector representation in Earth frame available from geomagnetic charts.

The origin of the Earth's magnetic field, is somewhat sill uncertain. However, many speculate that it is a result of the motion of molten iron alloys in the Earth's outer core. According to the "Geodynamo" theory, a rotating, convecting, and electrically conducting fluid acts to maintain a magnetic field. This fluid is the liquid iron in Earth's outer core.

The existence of this magnetic field is extremely beneficial, as it deflects most of the charged particles emanating from the Sun, protecting the ozone layer. It is similar to a magnetic field of a bar magnet tilted 11° from the spin axis of the Earth, as it is shown in Fig. 3.10a.

The magnitude of the Earth's magnetic field is greater near the poles and weaker near the Equator. The field ranges between approximately 25,000 nT and 65,000 nT (nT corresponds to nanoteslas). A graphical representation of this variation is presented in Fig. 3.10b.

3.6.1 Magnetometer

A Magnetometer measures the strength and, in some cases, direction of magnetic fields. Most magnetometers contain a magnetic device sensitive to an external magnetic field, such as a magnet or an electromagnet. Low cost magnetometers can be used for estimating the orientation with respect to the magnetic north, by measuring the components values of Earth's magnetic field in a specific location.

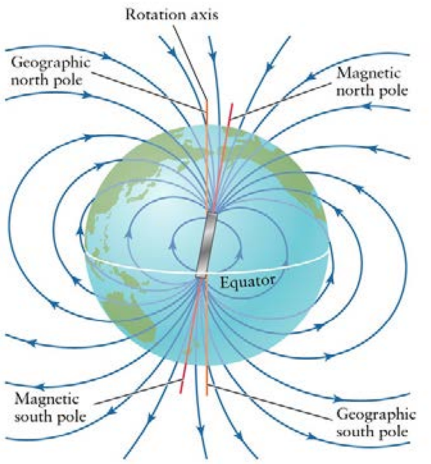

(a) Representation of Earth's Magnetic Field. Source: [7].

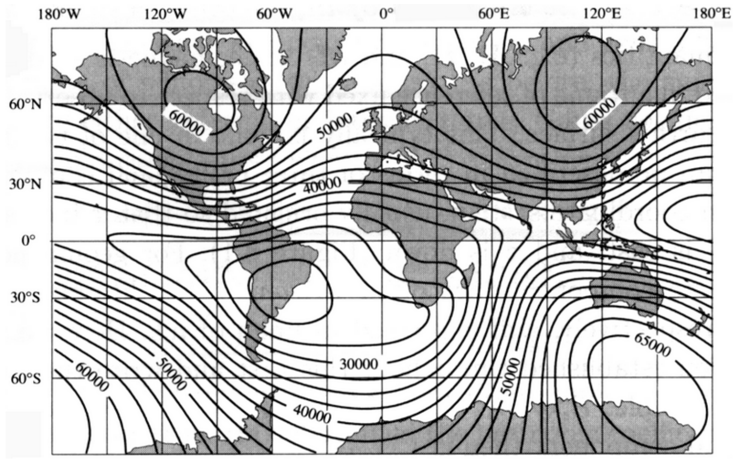

(b) Total magnetic field presented in nT. Source: [35].

Figure 3.10: Earth's magnetic field.

The main disadvantage of a magnetometer device is that it requires calibration techniques, as they are strongly influenced by magnetic perturbations produced by manmade infrastructures.

Some MEMS magnetometer are based on the Lorentz force acting on the current-carrying conductor in the magnetic field. Lorentz force, F, is the force on a point charge due to electromagnetic fields. It is expressed as follows:

$$F = q\left[E + (v \times B)\right], \tag{3.36}$$

where q if the charge of the particle, v the velocity, E the electric field and B the magnetic field. The mechanical motion of the micro-structure is sensed either electronically or optically. For the former, piezoresistive or electrostatic materials are employed.

Other MEMS sensor may be magnetoresistive sensors. These are made of thin strips of permalloy whose electrical resistance varies with a change in magnetic field. This change of values of the resistors, causes a bridge imbalance and generates an output voltage proportional to the magnetic field strength.

MEMS magnetometers measure values changes over time based on both the current local magnetic environment and the history of the device. The presence of a nearby metal object will distort Earth's magnetic field, resulting in readings that differ from the magnetic north and, as the sensors readings depend upon the device's history, the magnetometer may even report different values before the introduction of a nearby metal object or magnet compared with after its removal. The latter effect is known as "hysteresis".

3.6.2 AHRS and Orientation filter

In section 3.5, the INS system was introduced. This consisted of gyroscopes and accelerometers enabling the tracking of rotational and translational movements. With the addition of a magnetometer, based on [51], a Magnetic, Angular Rate, and Gravity (MARG) system, also known as Attitude and Heading Reference System (AHRS), is achieved. This is a hybrid IMU which incorporates a three-axis magnetometer, capable of providing a measurement of orientation relative to the direction of gravity and the Earth's magnetic field, whereas a simple IMU system can only measure an attitude relative to the direction of gravity and, in some cases, Earth's rotation. With the inclusion of a magnetometer, which measures the Earth's magnetic field, combined with the gravitational force it is now possible to compute absolute orientation.

However, the fusion of outputs from the three sensors (accelerometer, magnetometer and gyroscope), is not direct. An orientation filter is required, whose function is to compute a single estimation of orientation of the outputs, who may many times somewhat contradict each other.

When mentioning sensor fusion filter, it is direct to acknowledge the Kalman filter, as it has become the base of the majority of orientation filters. The Kalman filter is an algorithm that uses a series of measurements observed over time, containing noise, and produces estimates of unknown variables which tend to be more precise than those based on a single measurement alone. Based on [63], in an AHRS, the Kalman filter determines the optimum estimation of the Euler angles of roll (ϕ), pitch (θ) and yaw (ψ), by using two independent data sets:

- High-frequency values resulting of the integration of the angular velocities outputted by the gyroscopes.
- Low-frequency values outputted by the accelerometers and magnetometers.

As this thesis does not aim to implement an orientation filter, the Kalman filter is mentioned due to its importance in nowadays navigation, but a more detail analysis was not considered relevant.

3.7 Complementary Filter

As mentioned throughout this thesis report, the diver is responsible for handling the MAST/AM tool. The handle will be designed as to be closer to the gravity center of the tool as possible, in order to facilitate the tool's maneuverability. However, it is to be expected from the movement induced by the diver to be neither constant or projected on a single axis, which for this case only would be the x axis as the driver is swimming forward (Fig. 3.11). Most likely the diver will unintentionally induce a pitch and roll rotations, generating body frame tilting. When the diver performs these pitch and roll rotations, this tilt movement may generate dramatic changes in the position of the transmitter in $\{B\}$.

In an intentional movement the diver expects to see the direction of the transmitter shift. If the transmitter is directly in front of the diver, and the latter performs a yaw rotation to their right, he, the diver, would expect the transmitter's direction to shift to their left. However, if the diver does not realize its own rotation, the action will be assign to the transmitter. For example if the transmitter is at rest, in case of an non intentional movement, where the diver is unaware the tool has moved, he will have the impression that the transmitter is not stationary.

Although it may be possible for the diver to tilt the platform along x and y axes, the following filtering example will only try to solve the pitch rotation. A complementary filter for pitch estimation was implemented for the purpose of stabilizing the pitch rotation.

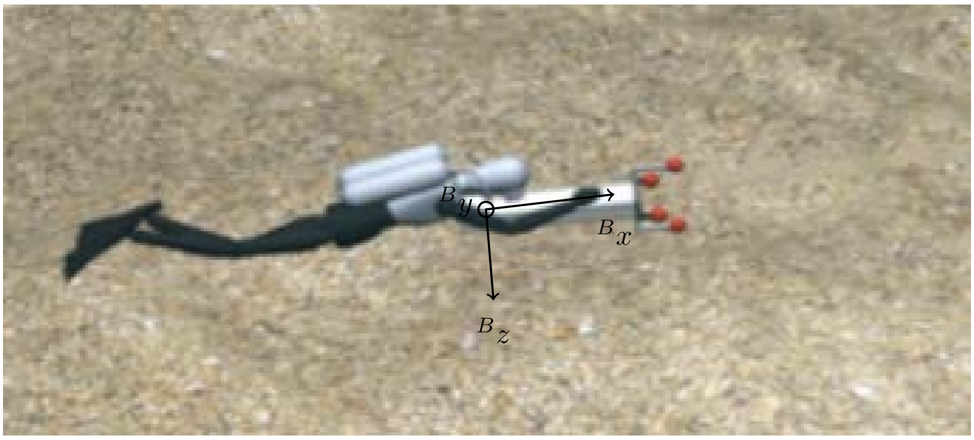

Figure 3.11: Movement of the diver handling the MAST/AM tool.

The present section will commence with an analysis of complementary filtering techniques, which was used as a theoretical basis for the implementation of a complementary filter for pitch estimation, merging values for pitch obtained from an accelerometer and complemented with a rate gyro. It is noteworthy that, by considering roll equal to zero, estimation of the pitch rotation from the rate gyro becomes linear. It is well known that this value is not null in reality, however, this filter must be seen as a direct application to a particular case with only unintentionally pitch rotation.The reader should acknowledge this filter as an example of inertial navigation filter developed for a single path followed by the diver where only pitch rotation is not negligible.

A simple estimation technique that is often used in navigation to combine measurements is the complementary filter. This filter was developed for explicitly addressing the issue of signal estimation based on measurements provided by sensors over distinct, yet complementary regions of frequency [59]. They do not consider statical description for the noise corrupting the signals, and their filter is obtained by a simple analysis in the frequency domain. This method successfully rejects the most noisy bands of the frequency spectrum and takes advantage of the bands where the signal information is stored. This filter is usually designed without any reference to Wiener or Kalman filters, although it is related to them. A complementary filter is equivalent to a general two input Wiener filter when one transfer function is the complement of the other [39].

A basic complementary filter is introduced in Fig. 3.12, where y_1 and y_2 are noisy measurements of a signal s. n_1 and n_2 correspond to the noise present in y_1 and y_2, respectively. $\hat{s}$ is the estimate of s produced by the complementary filter.

Each input signal will be filtered independently and the outputs of both transfer functions are summed. The result is the filter estimation of signal s, $\hat{s}$. Analytically:

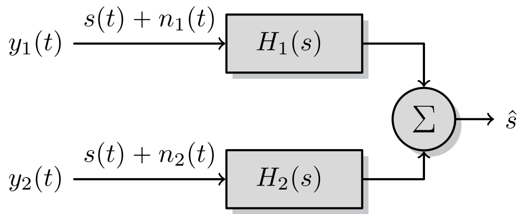

Figure 3.12: Complementary Filter.

$$\hat{s} = H_1(s)[y_1(t)] + H_2(s)[y_2(t)]. \tag{3.37}$$

Assuming that nearly all noise in y_1 is found in high frequencies and, on the contrary, in y_2 is mostly in low frequencies, the most appropriated form for $H_1(s)$ is to block high frequencies and for $H_2(s)$ to filter out low frequencies. $H_1(s)$ is then made into a low pass filter:

$$H_1(s) = \frac{k}{s+k}, \tag{3.38}$$

and $H_2(t)$ its complement, a high-pass filter:

$$H_2(s) = 1 - H_1(s) = \frac{s}{s+k}. \tag{3.39}$$

Considering $\hat{s}(s)$ the Laplace transformation of $s(t)$:

$$\begin{aligned}\hat{s}(s) &= H_1(s)(s(s)+n_1(s)) + H_2(s)(s(s)+n_2(s)) = H_1(s)(s(s)+n_1(s)) + (1-H_1(s))(s(s)+n_2(s)) \\ &= s(s) + (H_1(s)n_1(s) + (1-H_1(s))n_2(s)) = s(s) + \frac{k}{s+k}n_1(s) + \frac{s}{s+k}n_2(s).\end{aligned} \tag{3.40}$$

The break frequency is determined by the value assigned to parameter k. This choice is entirely dominated by the constraints of the sensor bandwidth.

Complementary filters are often used for attitude estimation based on data from INS [30, 29]. A complementary filter for attitude estimation performs low-pass filtering on a low-frequency attitude estimate, obtained from accelerometer data, and high-pass filtering on a biased high-frequency attitude estimate, obtained by direct integration of gyro output, and fuses these estimates together to obtain an all-pass estimate of attitude. Accelerometers only provide reliable data at low frequency, whereas gyros exhibit biases and drift phenomena at said frequency, being only useful at high frequencies. A basic block diagram is given in Fig. 3.13, for when using this method for pitch estimation.

The previous method will be used for pitch estimation during the diver's movement when handling the MAST/AM tool. Consequently, the break frequency and sensors characteristics (i.e noise, bias) were simulated as to resemble the IMU employed in the tool (refer to section 4.2.5).

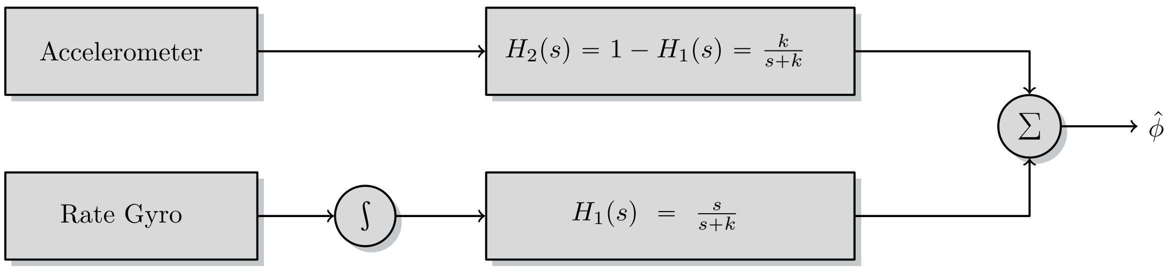

Figure 3.13: Pitch estimated based on data from IMU using complementary filters.

Regarding accelerometer and gyro signal, these were obtained by employing a mathematical model of a generic vehicle from previous work made under the scope of the MAST/AM project in [55]. The vehicle (represented in Fig. 3.14) is symmetrical and uniform in relation to the center of mass. Its dimensions and weight were introduced according to the characteristics of the tool. Six propellers were added to the vehicle, two per side allowing movement in any direction and rotations about any axis. The movement is induced by applying forces to this propellers, as the simulator then uses this forces to calculate the vehicle's path and the resulting output of the IMU, assumed to be coincident with the center of mass of the vehicle for reasons of simplicity. More details about this simulator can be found on annex B.

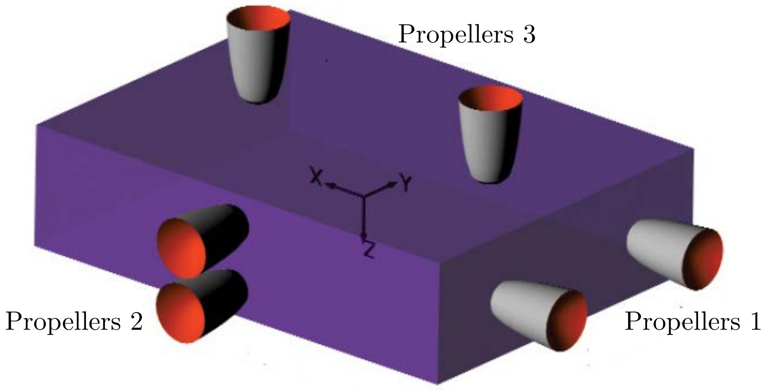

Figure 3.14: Vehicle's graphic representation. Source: [55].

The movement in Fig. 3.15 was simulated, illustrating the path of a diver. Three situations are represented in this path: in the first 30 seconds the is diver is stabilized. The tool is experiencing a slightly pitch rotation. From this point on, the diver moves forward. It is assumed that in motion the unintentional pitch rotation is of a higher value since the diver is inducing greater strength. Prior to 100 seconds the transmitter is motionless. Following this time period, the transmitter initiates its movement. Up to 120 seconds of the experiment, the transmitter movement is solely on the x and y axis. Afterwards, is also added position variation in the z axis.

The resulting rotation of the Euler angles is presented in Fig. 3.16. The output of IMU is displayed in Fig. 3.17.

The accelerometer and gyro signals simulated were used as input for the complementary

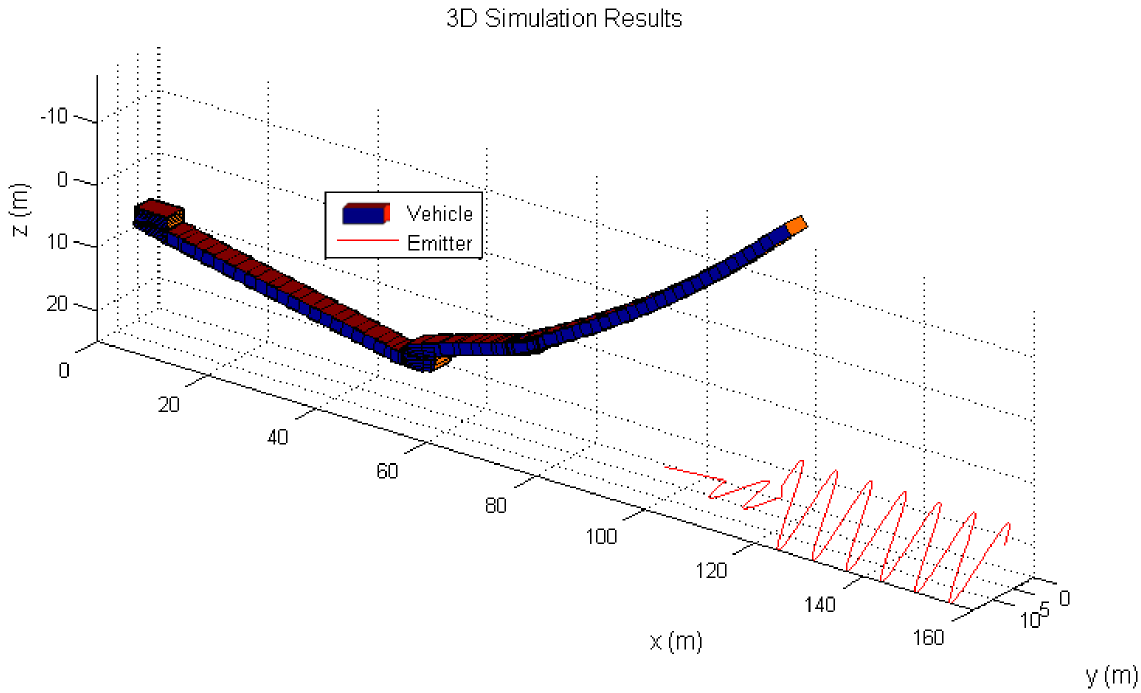

Figure 3.15: Diver's path simulated.

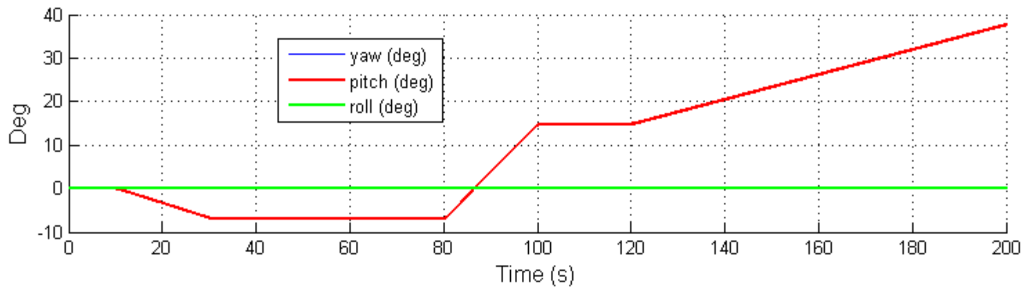

Figure 3.16: Simulation's resulting Euler angles.

filter for pitch estimation (see the *Simulink* model for this filter in annex C). From the outcome of the accelerometer pitch is equal to:

$$\hat{\theta}_{accel} = sin^{-1}\left(\frac{\mathbf{f}_x}{g}\right), \tag{3.41}$$

whereas pitch from the gyro is as follows:

$$\dot{\theta}\Big|_{\phi=0} = w_y \;\; ; \;\; \theta(t) = \int_{-\infty}^{T} w_y(\tau)d\tau + \theta_0. \tag{3.42}$$

The results of the pitch estimation is shown in Fig. 3.18, where the filter's output signal, $\hat{\theta}$, is compared to the simulated pitch rotation in the vehicle. For a more accurate analysis, the difference between the two signals is presented in Fig. 3.19.

By observing of the signals from both sensors before the filter, one can see that for the

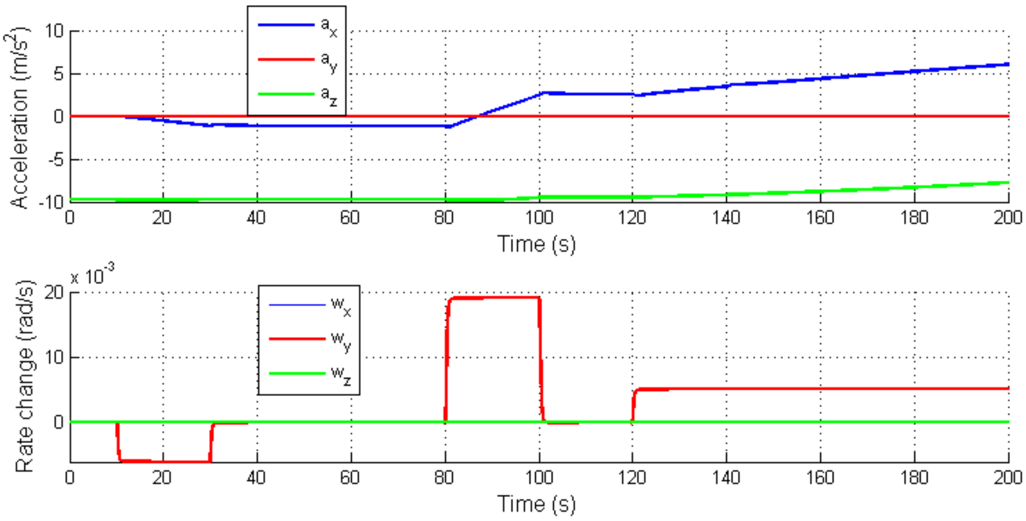

Figure 3.17: Simulation's resulting INS output.

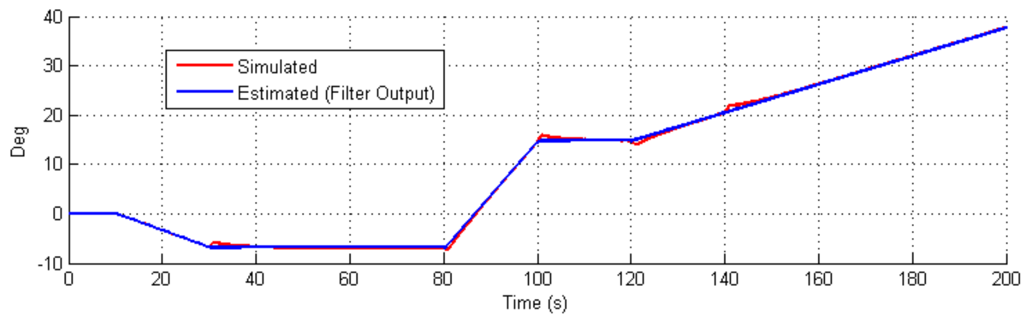

Figure 3.18: MAST/AM tool's pitch rotation estimated versus simulated pitch, in $\{B\}$.

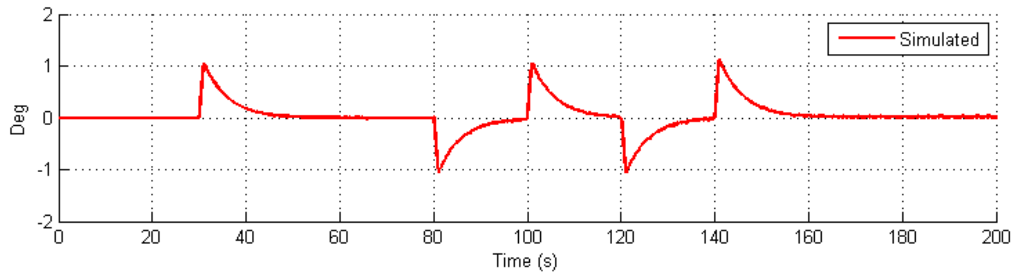

Figure 3.19: Difference between pitch estimated and simulated, in $\{B\}$.

accelerometer the filter has the effect of erasing the outliers visible in the signal. Regarding the gyro signal, it prevents the signal from increasing into infinite in open loop.

The results obtained for pitch estimation with the complementary filter are very satisfactory. However, to properly judge the improvement accomplished by using this filter, the advantages to the diver must be addressed. As will be further described in section 4.3, to the diver is displayed information concerning the direction and distance of the transmitter as well as the depth difference with respect to the transmitter. Notwithstanding the fact that the distance does not differ, both direction and depth difference suffer alterations when considering the tool's attitude. In Fig. 3.20 we see the direction and depth of the transmitter in $\{B\}$ with and without taking into account the pitch rotation the diver unintentionally induces in the tool. For comparison, the true transmitter's position in $\{B\}$ (considering the simulated vehicle's attitude) is added. The position of the transmitter simulated in $\{I\}$ (recall Fig. 3.15) was transformed to $\{B\}$ by using (3.2) with the rotation matrix (3.15).

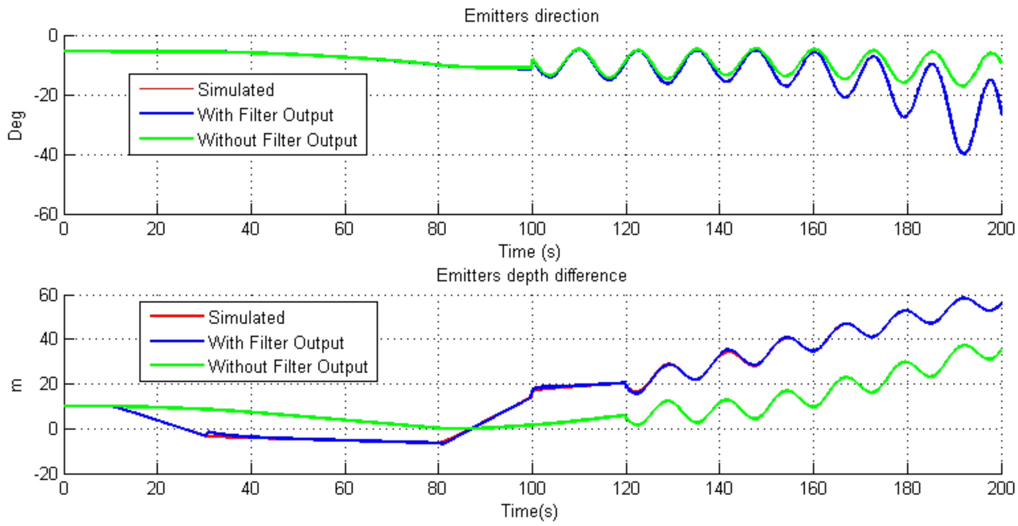

Figure 3.20: Results of the transmitter's distance and depth difference to the diver when using $\hat{\theta}$.

Based on the results obtained, it can be stated that the complementary filter has a very satisfactory behavior. Upon a path with single pitch rotation, the implemented filter successfully compensates for the non intentional variation in $\{B\}$ axes orientation. For direction estimation, it can be stated that complementary filter is only relevant when the transmitter's position in the z axis varies. However, it is quite remarkable the improvement in the calculation of the depth of the transmitter. In this case the complementary filter is highly beneficial.

4 | System Design

The present section aims to describe the implemented design for the portable underwater tool, developed and tested in the scope of the MAST/AM project. During the development of this architecture, the main factors taken into account in component selection were weight and power, given that the tool was intended to be as compact and small as possible to allow good handling from the diver. Low power consumption was also a priority, such that the lifetime of the battery would be as great as possible in order to enable a longer dive.

The proposed hardware and software architecture consists on an USBL array combined with an interrogator transducer and electronics responsible for signal acquisition and processing. The interrogator transducer is used when communication with a vessel at the surface is necessary. As a side note, there is no need for a propulsion or a depth control system, as the tool's movement is induced by the diver.

In order to facilitate the reading of this chapter, the system design is divided in three sections: Acoustic, Hardware Architecture and Software. The first will introduce the acoustic devices, namely the hydrophone, transducer and underwater tags. Hardware Architecture and Software is the most extensive, outlining the final prototype architecture. The software section presents the graphical interface designed to aid the diver, as well as the development which was necessary to be performed upon the Android device in order to enable communication with the DSP.

4.1 Acoustic

The present section introduces the devices required for signal acquisition and transmission, namely the hydrophone, transducer and underwater tag.

4.1.1 Hydrophone

The set of hydrophones selected were from HIGH TECH©, model name: HTI-96-MIN (Fig. 4.1a). They have a frequency response from 2 Hz to 30 kHz and can operate up to 500 m depth with no signal degradation.

4.1.2 Transducer

The interrogator transducer employed is the Model ITC-1042 (Fig. 4.1b). This is a spherical transducer which offers broadband omnidirectional transmitting and receiving response with efficiencies of over 50%. It is fabricated of Channelite-5400 lead zirconate titanate ceramic and is particularly well suited for noise sources as a broadband hydrophone and applications where an omnidirectional response is required [22].

(a) HIGH TECH© HTI-96-MIN.

(b) Transducer, model: ITC-1042.

Figure 4.1: Acoustic positioning system devices.

4.1.3 Underwater Acoustic Tags

Concerning the criteria used on selecting which tag version to acquire, one must start by addressing the preference over continuous or coded tags. Based on [61], in a continuous scheme, each transmission consists of a single pulse, whereas in a coded scheme each transmission consists of a series of pulses with the intervals between successive pulses representing a binary number. In a coded scheme the transmission interval duration implies that the transmitter is silent most of the times, which enables both a higher transmitter life, even when small batteries are used, and multiple transmitters to be simultaneously present, the idea being that a transmitter sends its signal when others are silent.

Both schemes have their advantages and disadvantages, but one must assess which one fits best the MAST/AM project. A coded scheme would allow the tool to be used with more than one target, however it is relevant to bear in mind that this project is still at a prototype phase, residing at an academic level. A scheme close to continuous, in which the algorithms implemented have the advantage of more samples, may increase their performance, and is hence preferable. Posteriorly, upon the decision of obtaining a continuous schemed tag, a compromise was reached between a scheme with a small transmission interval time, beneficial to the algorithms implemented, and a considerably good transmitter lifetime, profitable for this project as a product.

It was selected the VEMCO© $V16$ Continuous Transmitter model (Fig. 4.2), with 16 mm of diameter and 68 mm in length, and a data frequency of 63 kHz. For this model, VEMCO predicts a life-time of approximately 200 days.

Figure 4.2: VEMCO© V16 transmitter. Source: [74].

4.2 Hardware Architecture

The present section provides a detailed overview of hardware implemented in the MAST/AM tool, concluding with an analysis of the dimensions, weight and autonomy of the final system prototype.

4.2.1 Array

As mentioned previously in section 2.1.2.4, an USBL is used in the MAST/AM project as the acoustic positioning system. The USBL array was built using Bosch-Rexroth© aluminum rods and connections (Fig. 4.3), which allows for a highly configurable array structure, for optimal design during the evaluation and testing phases.

Figure 4.3: USBL array attached to the tool.

4.2.2 Signal Processing

Inside the watertight tool, a DSP acquired analog data samples through an ADC available on the D.SignT.Module.ADDA16, and generating an interrogator signal using Pulse-Width-

Modulation (PWM). The DSP should have sufficient processing speed to operate in real-time. The tool uses the D.SignT.Module.C6713, a high performance floating point DSP board. Furthermore, the DSP has an Ethernet interface [43], thanks to the D.SignT.Module.91C111, which is used as an outbound communication link for data analysis. The use of a DSP eliminates the need of an external CPU. Also it is considerable smaller than any small PC available in the market, which is beneficial for the project considering the intended small dimensions of the tool.

The DSP stack can be seen in Fig. 4.4. A brief description of each board, based on [28], is is shown below:

D.SignT.Module.ADDA16 Offers four differential input channels which are sampled synchronously by precision 16-bit 250 KSPS successive approximation ADCs. Also provided are four single-ended analog outputs, driven by 16-bit D/A converters with $2\,\mu$s settling time. It has a maximum sampling frequency of 250 kHz The architecture guarantees a very small delay from sampling to data availability: $4\,\mu$s, independent of sampling clock. It has a digital single power supply of $+3.3V$, and a analog dual supply equal to $\pm 5V$.

D.SignT.Module.C6713 Designed for embedded standalone applications requiring maximum performance and flexibility. The Setup Mode provides straightforward file upload for program and parameter updates via RS-232 terminal. Data acquisition and memory block transfers are handled in background by an enhanced 16 channel Direct Memory Access (DMA) controller. It has a single power supply of $+3.3V$. The D.Module.C6713 architecture provides 8 instruction units which operate in parallel, yielding a maximum performance of 2400 Microprocessor without Interlocked Pipeline Stages (MIPS), 1800 Million Floating Point Operations Per Second (MFLOPS). Up to 256 Kbytes internal memory and a two level cache architecture guarantee the memory bandwidth required to sustain high data throughput.

D.SignT.Module.91C111 Connects the DSP stack to an Ethernet LAN. Additionally, this board is equipped with a real-time clock (RTC) and a MultiMediaCard (MMC/SD) interface. It has a single power supply of $+3.3V$.

The hydrophones are connected to the AGCAMP stack, which in turn are connected to the D.Module.ADDA16's D/A converters. These converters send data to the DSP through DMA. A brief definition of this controller is hence called for. DMA enables data transfer without interrupting the CPU. The CPU has only to configure the DMA, but is then free to other processing even when DMA is transferring data. One must only be careful in such occasions when the CPU and the DMA are accessing the same memory position. In the MAST/AM project, the CPU will only access data once the DMA has finished storing it in memory.

Each hydrophone signal is routed through an Automatic Gain Control (AGC) signal amplifier (*AGCAMP*) board developed at ISR/IST (annex D.1), whose gain can either be let in automatic mode or overridden by an analogue voltage control from the DAC available on the DSP module. The DSP receives the data and stores it in memory without interrupting the core processor which is doing time-critical acoustic signal processing (Fig. 4.5). Additionally, if so is

Figure 4.4: DSP stack.

desired for the navigation filter, at specified instants of time, the DSP will send out a ping to the transponder, which in turn communicates with a vessel at surface.

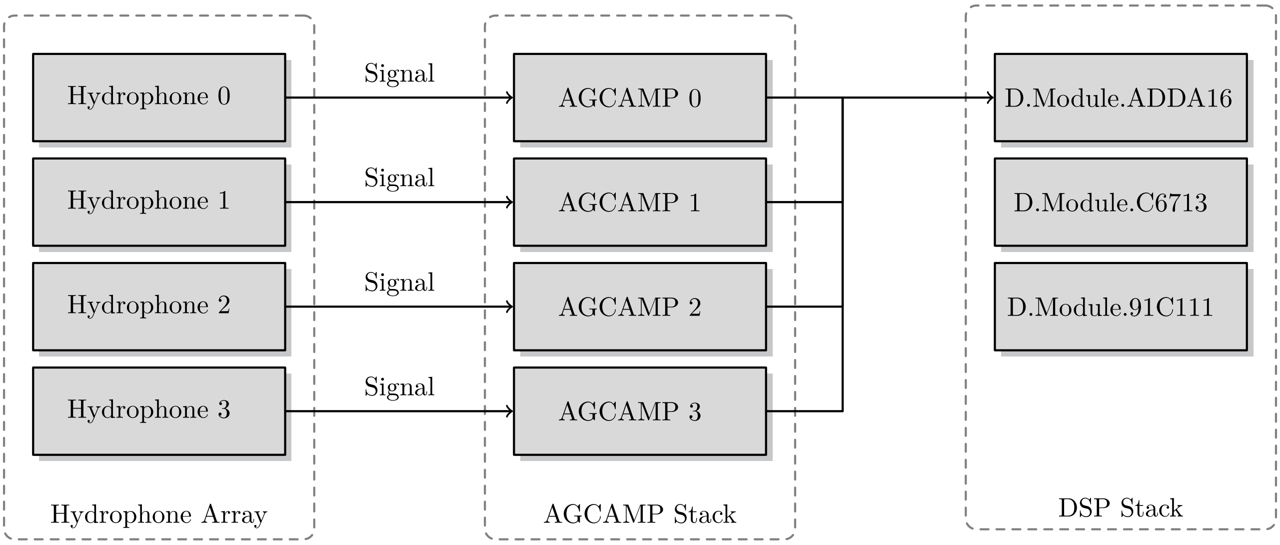

Figure 4.5: Architecture for signal acquisition and processing.

4.2.3 Interrogator System

An interrogator is added to the architecture for the purpose of communicating with an USBL system on the water surface, required when the implemented navigation algorithm calls for additional information concerning the diver's location. The PWM signal to the interrogator transducer passes through a Class D power Amplifier (PWRAMPD) board developed at ISR/IST (annex D.3) (Fig. 4.6). Other signal amplification architectures may involve a Class B power amplifier [83]. This is a widely used power amplifier whose efficiency is low in the low power state and high in the high power state, in which the maximum power efficiency reaches 78.5%, while the Class D amplifier can reach 100% no matter how much the output power is. These efficiency numbers are expected in theory, taking place some variations in practice. For the MAST/AM project, the efficiency superiority led to opt for the Class D power amplifier, however at the expense of a higher cost. Additional, the latter also offers the advantage of reduced size and weight, which was an advantage given the space limitations inside the tool.

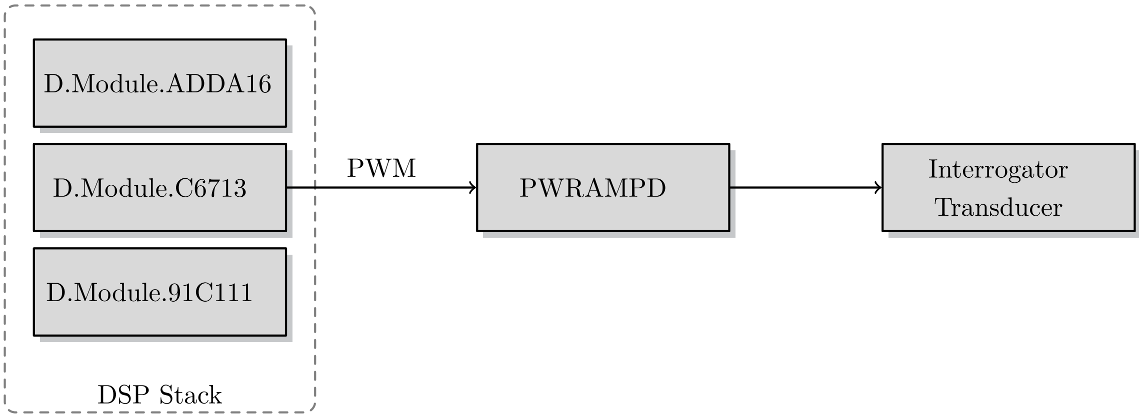

Figure 4.6: Interrogator system architecture.

4.2.4 Visualization Hardware

As part of the MAST/AM project, the diver handling the tool underwater must have some kind of visualization interface indicating which direction they must follow to further reach the target. At an initial phase of the project, it was decided to use an Android device as a visualization platform. Combining a high performance with a slim design, the Android [81] device fully meets the requirements of this project. The selected device was a Samsung© Galaxy SIII LTE [82], Android OS, V.4.1.2 (Jelly Bean) [36]. It is noteworthy that this device will render visualization of the computed data solely, hence it does not require real time processing like the DSP.

As mentioned before, a DSP is responsible for the data processing in real-time. After processing, the DSP must send the results to the Android device to be displayed to the diver, for which they must be connected. Apart from the four input channels of the D.Module.ADDA16, which are connected to the AGCAMP stack, the DSP has a RS-232 terminal and an Ethernet port left. However, the RS-232 is used for establishing communication with the INS device, as it will be described in section 4.2.5. This leaves out the Ethernet output interface for the Android device (Fig. 4.7).

For this connection to be enabled, the Android device must be able to detect that it has been attached to an Ethernet connection, and properly configure it to successfully receive data from this connection. As it is easily predicted, this type of drivers are not embedded in the device's initial firmware, as this is not a standard usage of an Android device. Additionally, as the only input port available in the Android device is a micro-B interface, it was necessary to resort to an USB[42]/Ethernet Adapter and an USB-A/micro-B On-the-Go (OTG) cable (OTG

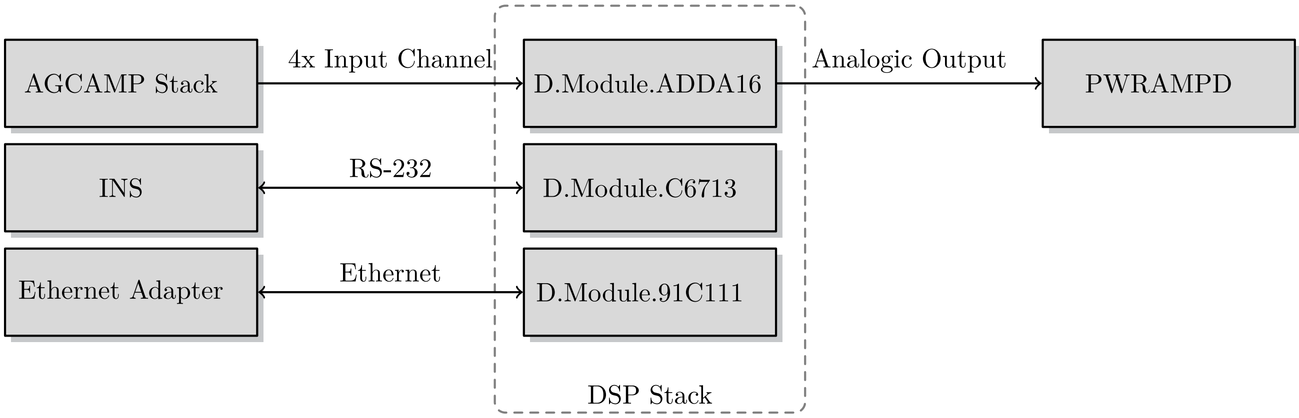

Figure 4.7: Connections established with input and output ports of the DSP stack.

enables the Android device to act as an USB host, the USB/Ethernet Adapter only functions correctly when connected to a host [58]). The procedure for installation of the required drivers for the USB/Ethernet adapter is described in section 4.3.1.

With the connection between the Android device and the DSP made possible with the USB/Ethernet adapter, the next step consisted on creating an interface which would show the diver's position relatively to the target's position. Within the written code for this application, error handling was introduced in such a way than the application will handle the constant connection and disconnection of the USB/Ethernet adapter, as it is only switched on when the battery pack is powered on. The Android device starts the application every time power is connected, which corresponds to the battery pack being switched on. However, the device must be already switched on, as this action in only possible by pressing the power button. The Android device is charged only when power is connected. Otherwise, the device is in discharge mode. If the device runs out of battery, unfortunately the tool will have to be opened in order for the home button to be pressed. In order to minimize as much as possible the need to remove the Android device out of the tool, it was made possible to send a message through Ethernet which will put the device in sleep mode. In this sleep mode, the Android device battery will run for approximatively one week. More on the visual interface can be found in section 4.3.2.

4.2.5 Inertial Navigation Systems

Initially, for navigation sensors, it was considered to use the Android device's sensors. These are made using MEMS technology. This way all sensors are part of the device's hardware. Tests were made in order to evaluate and assess the performance of the sensors. This was accomplished through the development of an application which recorded in real-time the raw data of the accelerometer, gyroscope and magnetometer. The specifications of the sensors are displayed in Table 4.1 . This experiment was made with the Android device stationary on lower floors as to avoid structural vibrations. Analysis of the Android sensors showed a large presence of jitter (deviation from the appointed periodicity), as can be seen in Fig. 4.8 which is not appropriate for the use in navigation systems.

Sensor	Resolution	Maximum Range	Maximum Frequency
Accelerometer	$0.009576807\,\mathrm{m/s^2}$	$\pm 19.6133\,\mathrm{m/s^2}$	100 Hz
Gyroscope	$0.0175\,°/\mathrm{s}$	$\pm 500\,°/\mathrm{s}$	100 Hz
Magnetometer	$0.06\,\mu\mathrm{T}$	$\pm 2000\,\mu\mathrm{T}$	100 Hz

Table 4.1: Sensors available at Samsung Galaxy SIII LTE. Acquired by direct request from the sensors. The API provides several classes and interfaces, which allow to request values for maximum range, manufacturer, power requirements, and resolution [37, 53].

A comparison was made with the device Microstrain 3DM-DX3©-35, available at ISR. The 3DM-DX3©-35 is a high-performance, miniature AHRS, using MEMS sensor technology. This instrument is a strapdown system responsible for providing data from a triaxial accelerometer, a triaxial grate-yro and a triaxial magnetometer with a 16 bit A/D resolution. All of these sensors are wired via an analog-to-digital converter to the Microstrain's Main Control Unit (MCU). Data output rate is up to 1 kHz [19]. Specifications are further described in table 4.2.

Sensor	Resolution	Maximum Range	Sampling Rate
Accelerometer	$0.0113\,\mathrm{m/s^2}$	$\pm 49\,\mathrm{m/s^2}$	30 kHz
Gyroscope	$< 0.1\,°/\mathrm{s}$	$\pm 300\,°/\mathrm{s}$	30 kHz
Magnetometer	$0.1\,\mu\mathrm{T}$	$\pm 250\,\mu\mathrm{T}$	7.5 kHz max

Table 4.2: Microstrain's INS specifications. Source: [19].

The Microstrain device showed a considerable lower jitter, as show in Fig. 4.9. Accordingly, it was preferred to use this instrument as IMU.

Afterwards, it was tested the possibility of connecting the Microstrain 3DM-DX3©-35 to the Samsung Galaxy SIII. This would have the advantage of freeing one of the DSP interfaces. However, it was found that the Android API does not recognize this instrument, due to the fact that the Microstrain connects through Abstract Control Model (ACM) for which the SGSIII does not have drivers.

The Microstrain 3DM-DX3©-35 will be IMU of the portable underwater tool, which is connected to the DSP's RS-232 serial link, with a baud rate of 115200 bps. From the Microstrain it is requested data output from the accelerometer, magnetometer and gyros, as well as data concerning Euler angles and rotation matrix. The DMA stores the data from the Microstrain. Hence it does not interrupt the real time acquisition and processing of the acoustic signal from the hydrophones. The DSP processes this stored data when it is most convenient.

4.2.6 Outbound connection

An outbound connection was added to the architecture of the tool for the purpose of analyzing the system's performance. An Ethernet connector was used in the tool for outbound

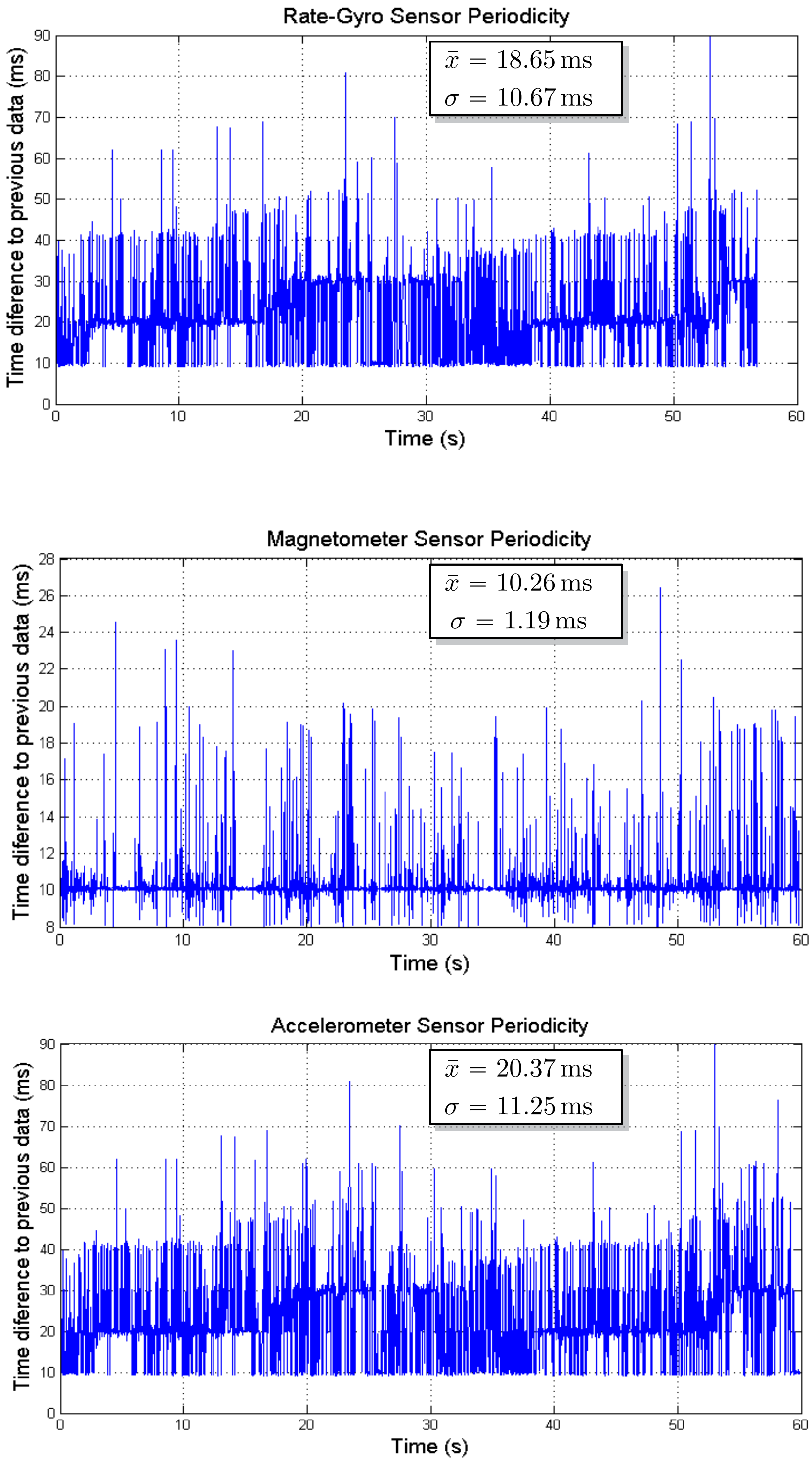

Figure 4.8: Jitter from Android Device Sensors.

communications. In the end of the tool (opposed to the end with the hydrophones), an Ethernet interface was included, thus allowing a PC to receive data from the signal processing architecture. For the purpose of constructing a “three intervening” connection, between the DSP’s Ethernet interface, the outbound connection and the Android device through the Ethernet/USB adapter, an Ethernet switch was added to the architecture (Fig. 4.10).

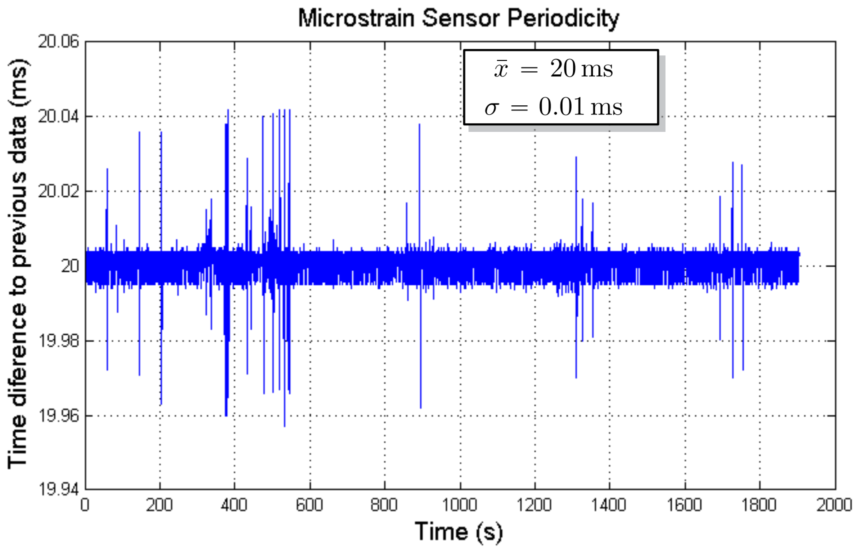

Figure 4.9: Jitter from Microstrain's Sensors.

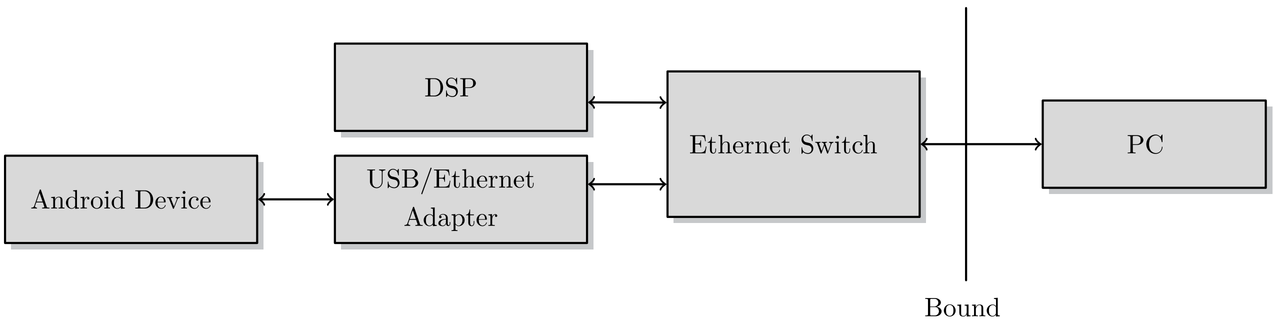

Figure 4.10: Outbound Connection, DSP and Android's device connected through an Ethernet switch.

A mission profile where this outbound communication might come in handy, could be, for example, one where the tool, driven by a diver, is connected to a support vessel through an umbilical cord and the vessel has access to the results processed by the tool. A situation in which the tool is attached to a vessel and is sending data to its crew members can also consider.

4.2.7 Temperature Reading

The performance of electronic devices is affected by temperature. At a high temperature errors may occur, or even destruction of the device. During operations devices naturally tend to increase their temperature over the course of its operation. In confined spaces, if no device is added to transfer heat elsewhere, the temperature may increase considerably. In some cases, there is a need for counteracting this buildup of heat if it is considered that the temperature will naturally reach a value prone to electronics damage. Such can be done by adding a fan, preferably located near the devices which produce more heat. The fan dissipates heat into the surrounding medium, and hence should be placed around the area most prone to build up heat in order to dissipate heat to regions with a lower temperature.

The employed sensor for temperature reading, inside the tool, is the Bosch Barometric Pressure Sensor (BMP) 085 [17]. This device excels in its small size and ease usage. It offers a measuring range of 300 to 1100 hPa with an absolute accuracy of down to 0.03 hPa. A Sparkfun© breakout board for the BMP085 is used [64].

A microcontroller board AVRCAN128 (annex D.4) developed at ISR, is interfaced with the BMP sensor. This microcontroller acts as the "brain" that controls the sensor. The AVRCAN128 board is connected to a Sparkfun©'s XBee Explorer USB [65], which enables communication with an USB device (Fig 4.11).

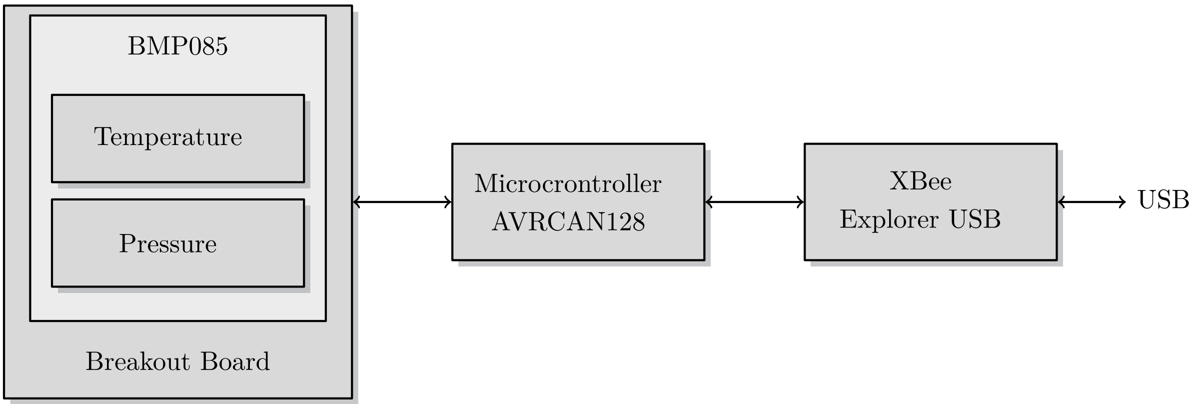

Figure 4.11: Architecture for control and communication with the BMP085 sensor.

The Android Device acts as an USB device, which makes it possible for it to be attached to the XBee Explorer. Taking into consideration the fact that the Android device is also intended to be USB/Ethernet adapter, a small USB was added to the architecture to couple both devices to the Android device (Fig. 4.12).

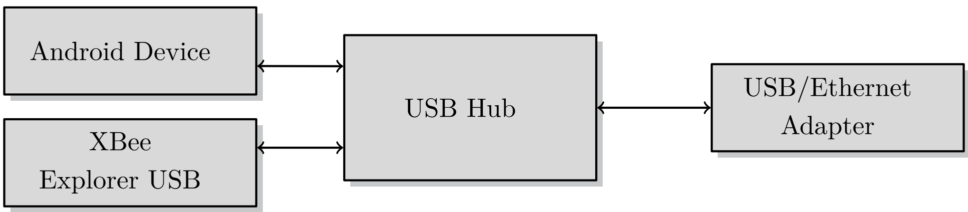

Figure 4.12: Connections established with the Android device.

For analysis purpose, a feature was implemented in the Android device which acts as recorder for the data outputted from the Sparkfun© BMP085 sensor. Fig. 4.14a shows the result of an experiment where the tool was sealed and all the electronics powered. The tool was connected to a constant power source which enabled the experience to be conducted for an amount of about 5.15 hours in order for a point of thermal equilibrium to be observed. In the 5.15 hours recorded, the temperature increased from $27°C$ to $31.2°C$, resulting in a variation of $4.2°C$. At the end of the experiment, the values present a tendency to stabilize. This fact coupled with the small variation observed led to consider that a fan was not required, specially when considering that the testing environment (out of the water at room temperature) was nearly the worst case scenario, only surpassed by a situation where the tool is exposed to direct sunlight. Under water the temperature inside the tool is not expected to reach the values observed.

4.2.8 Pressure Reading

Inside the tool, pressure grows as a result of the temperature rise. The tool requires low pressure to enable sealing O-Rings (Fig. 4.13a) in the tool's lid and to maintain the tool watertight. The O-Rings are used for the two static seals on the tool, as they provide a simple and reliable method. In addition, they require very little-structure and mechanics to implement.

A style of male piston was used in the implementation of the O-Rings. In this sealing method the O-Ring is placed in a gland on the male part, which is inserted into the female part. The O-Ring seals against the inner diameter of the female part and the outer diameter of the male part. According to [20], the use of a piston seal is favorable since the O-Ring stays in place better during installation due to being stretched over the male part.

The BMP085 sensor is also used for pressure reading. At the closing of the tool, pressure is set at a value of 0.5 bar, by resorting to an air pump connected to the tool's pressure port (Fig. 4.13a). The pressure port is sealed with a pressure port screw (Fig. 4.13b), which has a small O-Ring to ensure proper seal of the port.

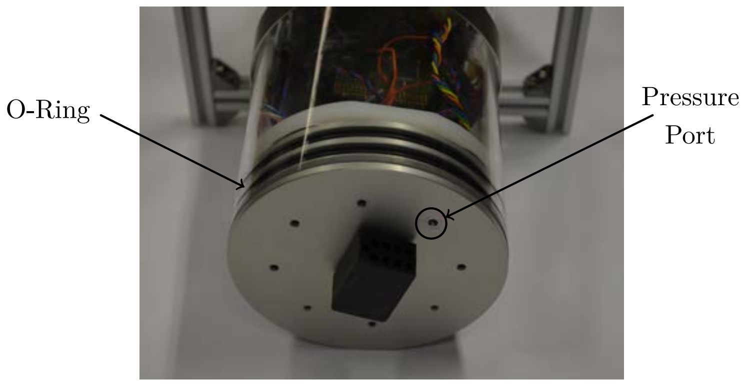

(a) O-rings at one end of the MAST/AM tool.

(b) Pressure port screw.

Figure 4.13: MAST/AM tool's sealing method and pressure port.

Throughout the mission, it will be considered a threshold of safety equal to 0.65 bar. From the moment at which the pressure value exceeds this value, both a warning sound and a visual sign generated by the Android device will go off.

Fig. 4.14a presents pressure values of the experiment previously mentioned in section 4.2.7. One can see in the figure that the pressure values remain between the desired thresholds. Fig. 4.14b displays the relation between pressure and pressure values. Values grow proportionally to one another.

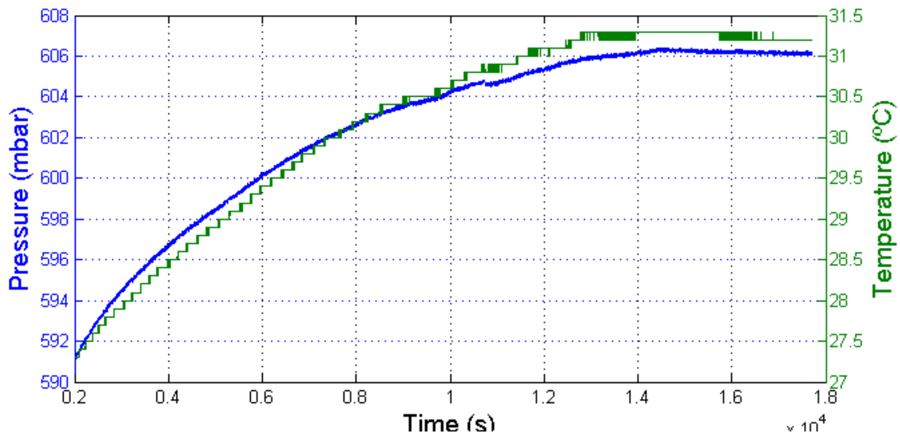

(a) Evolution of pressure and temperature values inside the MAST/AM tool.

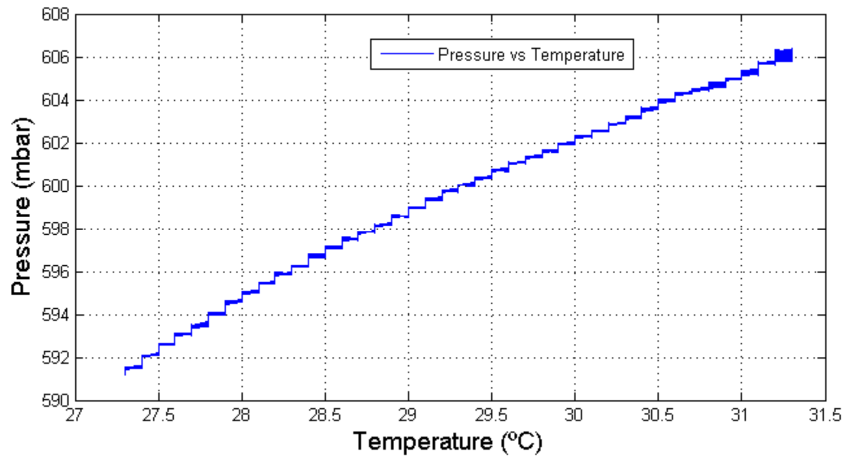

(b) Relation between pressure and temperature values inside the MAST/AM tool.

Figure 4.14: Experiment: pressure and temperature rise inside the MAST/AM tool.

4.2.9 Power Source

For batteries, it was chosen to use a 230 Wh Lithium-Polymer rechargeable battery pack, assembled from four Kokam© High Energy Density Cells [47], of 16 Ah each, with a nominal pack voltage equal to 14.8 V. The batteries are located at the inferior half of the tool, in order to lower the center of gravity. A Battery Monitor (BATMONIT) board, developed at ISR (annex D.2) is used in order to control a switch which allows to transition between states on, off, and charging state. Furthermore, it monitors charge and discharge voltage and current. To be noted that the available time for each dive depends on the batteries' life time. The battery pack powers the entire system. All electronics, except for the Android device, are powered up when the battery pack is switched on.

The electronics are not powered directly by the battery pack as their voltage value is not constant, as their values tend to decrease. There must be a power conversing between battery pack and electronics in order to guarantee a constant voltage value, and also to provide galvanic isolation between battery packs and electronics. Three boards were used as power conversing. Two developed at ISR: a Power Supply/Can opto-isolation and termination/RS-485 board (PWROPT0485) (annex D.6) and a Switching Low Noise Power (SWLNPWR) (annex D.7), plus a DC-DC converter board with a TRACO POWER© [3] TEN 15-2411 which outputs +5 V. The division of power from the battery pack to all three boards is made by a Power Distributor Board (PWRCONN) (annex D.5).

The PWROPT0485 board has two high performance DC-DC converter modules: TRACO POWER© TEN 15-2410 and TEN 10-1221, which output a voltage of $\pm 5V$ and $3.3V$, respectively. The SWLNPWR board will generate a regulated voltage of $12V$. PWRCONN is again used for power splitting at the output of both boards.

Concerning the Android device, experiments showed that it required power to be directed to the battery terminal in order to be switched on. As connecting cables to this terminal or changing the electronics would always be more troublesome compared to leaving the battery in the device, the latter option was preferred. The Android device is, hence, powered through its micro-B interface, which transmits both power and data. The minimum voltage found to enable the normal running of the device was about $+3.8V$. It was decided to power the Android device with $+5V$. To be noted that for the purpose of lowering energy consumption, this device is set to work in “Airplane mode”, and all utilities not strictly necessary for the performance intended from the device (i.e WIFI, Global System for Mobile Communication (GSM), bluetooth) are disabled.

It was previously stated that the micro-B interface of the Android device would be used as power supply. However, the reader may recall that this micro-B interface was also necessary for establishing host communication with the USB Hub. Additionally, in these devices the port for communication with the host is also the power supply. As a result, both the micro-B interface of the Android device and the input port of the previous devices require data exchange and power supply. The obvious solution was to try to implement a three way connection between the Android device, a charger and the USB hub (the USB/Ethernet adapter and the XBEE explorer USB are powered through the USB hub), where the charger would power the other two ends and data exchange between the Android device and the USB hub would be enabled.

In section 4.3 it was mentioned that an Android device must be connected through an OTG cable in order to act as host. The common OTG cables available on the market receive only data and are fabricated in a way that the Android device is responsible for powering the device to which it is connected. It was then necessary to make an OTG cable with charging enabled. To make such cable, a normal micro-B/USB-A cable was used for connecting the Android device to the USB/Ethernet adapter. However, both the V_{CC} and Ground cables were connected to the DC-DC converter and the Sense/ID pin was connected to the Ground cable through a 68 kΩ resistor (a schematic of this circuit can be seen in Fig. 4.15). The result was that both the Android device and USB/Ethernet adapter were powered by the DC-DC converter and the Android device acted as host and exchanged data with the USB/Ethernet adapter. The $68k\Omega$ is not a standard value which may be applied to all devices. The correct value for the resistor which allows such cable to work varies according to the device. The $68k\Omega$ value was found by testing the range of possible values of the USB standard, and this value was the only one that worked.

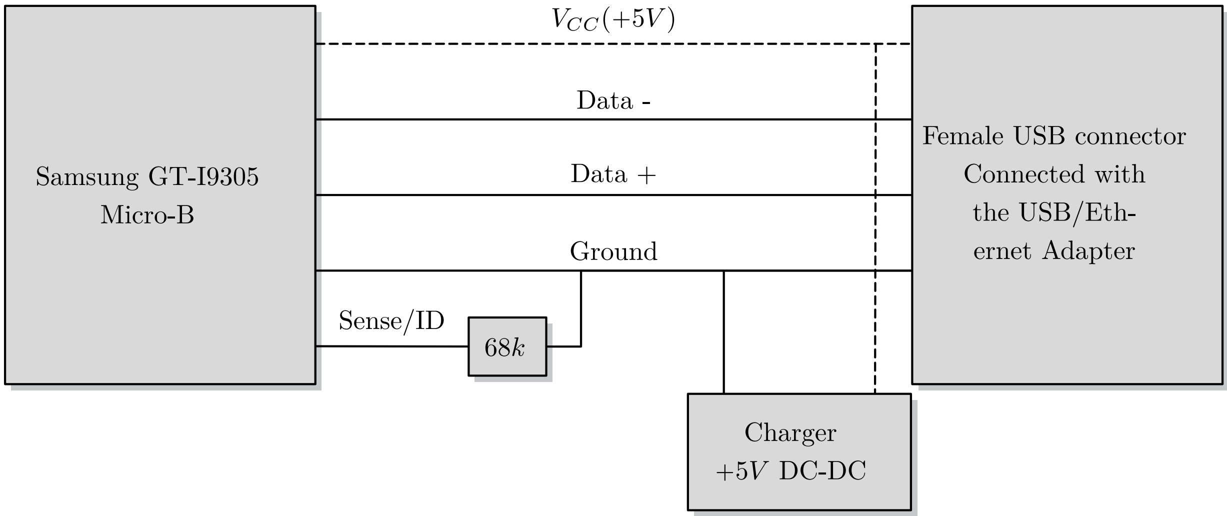

Figure 4.15: OTG Y cable with charging enabled.

A complete block diagram of the prototype architecture with power supply information is displayed in Fig. 4.16.

4.2.10 System Autonomy

Determining system autonomy is vital for determining the dive total duration, as the lifetime of the battery pack has direct influence in the time the electronic devices are operational and consequently the time the diver is able to visualize data concerning the target's position.

A power budget analysis will be used to determine how long the MAST/AM tool will operate without recharging. At a first approach, all elements which compose the electronics inside the tool were studied regarding the amount of energy that they would require when working in the desired conditions. In other words, the total consumption of the system. This estimation was made under the assumption of the largest consumption, that is, under the worst efficiency. Therefore, it is expected that this estimation differs for the worst from the results obtained in experiments in real scenario.

During this analysis, certain elements were not included, as they consume negligible currents, in the order of few mA. These elements are the BATMONIT, and SWLNPWR boards. The PWRAMPD power consumption depends on the periodicity of which the interrogator transducer produces signal. The periodicity was not study during the work of this thesis as it will depend of the requirement of the navigation filter implemented in the MAST/AM tool. Consequently, the PWRAMP will not be added to the system autonomy analysis. However as this analysis will be based on the largest consumption and the PWARAMPD has low consumption, the lack of this device does not affect significantly this estimation. The result of the latter analysis can be found in Tables 4.3 and 4.4. For Table 4.4 the values correspond to the maximum power consumption available in the devices' specifications. For table 4.3 the assumptions made for finding the power consumption are presented below.

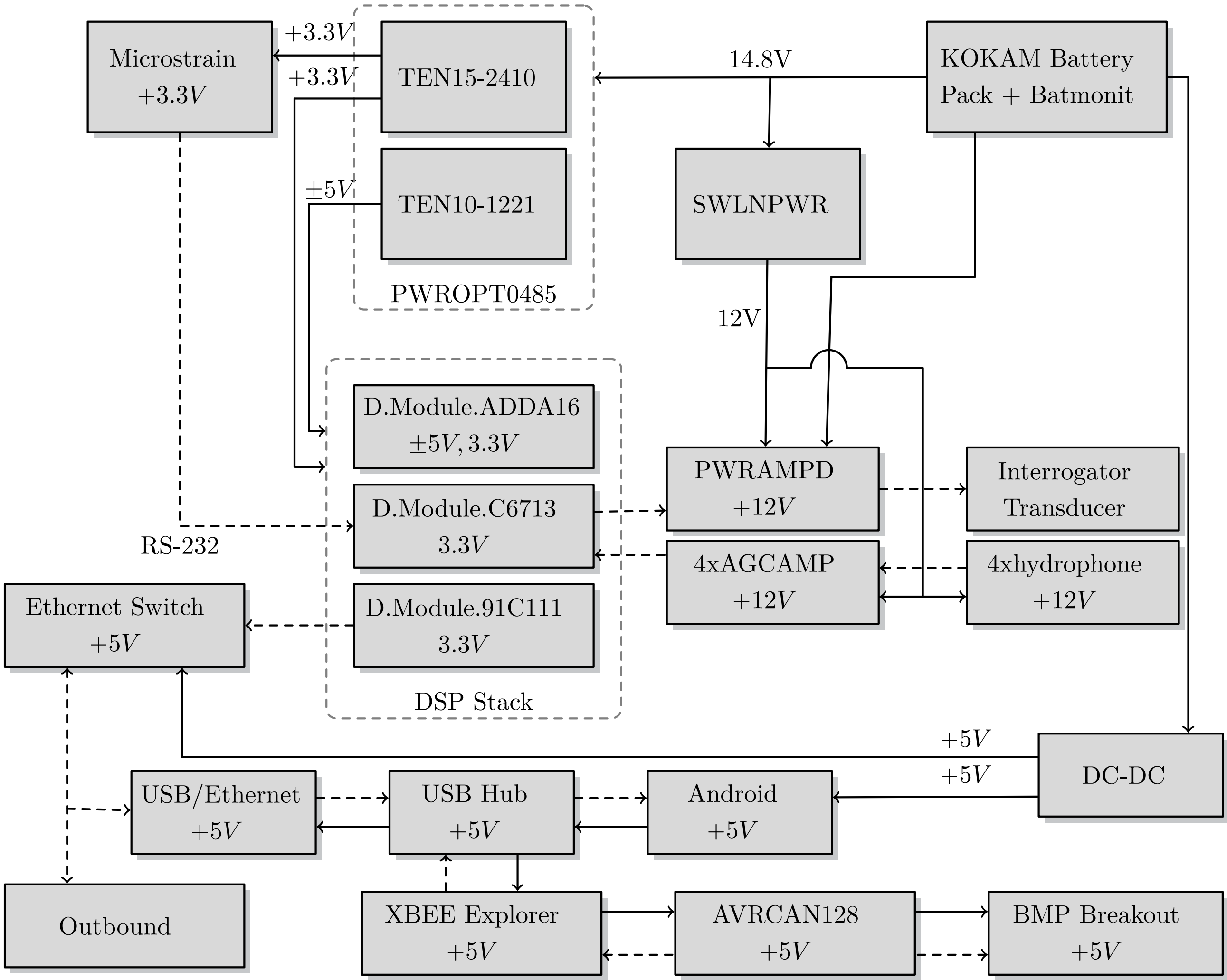

Figure 4.16: Architecture of the prototype for the MAST/AM tool.
—— power, – – data

	PWROPT		DC-DC	AGCAMPstack
	TEN10-1221	TEN15-2410	TEN15-2411	
V_{CC}	$+14.8V$		$+14.8V$	$+12V$
W	0.96 W	7.66 W	1.49 W	0.14 W

Table 4.3: Consumption of devices inside the MAST/AM tool found by assumption.

A brief note regarding Table 4.4: the value of $2.06A$ may seems exaggerated but it is necessary to recall that this corresponds to the max power consumption of the DSP boards: $1.5A$ from the D.SignT.Module.C6713, $0.4A$ from the D.SignT.Module.ADDA16 and $0.16A$ from the D.SignT.Module.91C111. Both the PWROPT and the DC-DC were developed around TRACO POWER cells. According to their specification, the TEN 15-2410, TEN 15-2411, TEN 10-1221 have a efficiency equal to 80%, 84% and 78%, respectively. Assuming these values, this cells have a power consumption of:

	DSP stack			Microstrain	Android + USB Hub + Connecting Devices	Ethernet switch
V_{CC}	$+5V$	$-5V$	$+3.3V$	$3.3V$	$+3.3V$	$+5V$
I	$0.08A$	$0.07A$	$2.06A$	0.25	$1A$	$0.5A$
W	0.40 W	0.35 W	6.798 W	0.825 W	3.3 W	2.5 W

Table 4.4: Consumption of devices inside the MAST/AM tool found experimentally.

$$\begin{aligned} W_{TEN10-1221} &= \frac{0.4\,\mathrm{W} + 0.35\,\mathrm{W}}{0.78} = 0.96\,\mathrm{W} \\ W_{TEN15-2410} &= \frac{6.633\,\mathrm{W} + 0.825\,\mathrm{W}}{0.8} = 7.66\,\mathrm{W} \\ W_{TEN15-2411} &= \frac{1\,\mathrm{W} + 0.25\,\mathrm{W}}{0.84} = 1.49\,\mathrm{W}. \end{aligned} \tag{4.1}$$

Each AGCAMP has a Quiescent Supply Current of $2mA$. With a supply voltage of $12V$, gives $W = 0.096W$ for the AGCAMP stack. By considering that the DC/DC which powers this device has a performance of 70%:

$$W_{AGCAMP} = \frac{0.096\,\mathrm{W}}{0.7} = 0.14\,\mathrm{W}. \tag{4.2}$$

By adding the values of power consumption previously presented, the MAST/AM tool has a total power consumption of 24.414 W.

According to the battery pack specifications, it has a capacity, C, value equal to $16Ah$ and a nominal package voltage of $14.8V$, which results in a energy of 230.4 Wh. In practice, a Lithium-Polymer battery cannot be repeatedly 100% discharged. Therefore, it is necessary to de-rate the battery by some amount. Considering that a maximum of 60% of the battery power will be used continuously, results in a energy of 138.4 Wh. Consequently, the practical time between recharge is approximately:

$$T = \frac{138.4\,\mathrm{Wh}}{24.414\,\mathrm{W}} \approx 5.67\,\mathrm{h}. \tag{4.3}$$

The power consumption was tested by connecting the MAST/AM tool to a constant power source of $14.8V$ through the Subconn©. It was observed that the tool consumed a power equal to $19.24W$. As expected this is below the maximum power consumption estimation. Hence is guaranteed the estimation of a time between recharge differs for the worst from the results obtained in experiments in real scenario. A time duration of 5.67 hours for a continuous operation is considered to be a very satisfactory value.

4.2.11 Dimensions and Weight

Prior to its implementation, the design of the *MAST/AM* tool, and the electronic devices inside, were designed using the SOLIDWORKS© software. Hence, it was possible to automatically conjugate the decision of adding a device to the tool's interior with the validation that said device was liable to be installed. The dimensions of the MAST/AM tool are presented in Fig. 4.17. The designed disposition of all electronic devices inside the tool can be seen in Fig. 4.18a. The ACGAMP, BATMONIT, SWLNPWR, DSP stack, PWRAMP, PWRCONN, O-Rings, the tool's lids and the battery pack were developed by DSOR/ISR researchers. The parts modeled by this thesis author can be found in annex E.

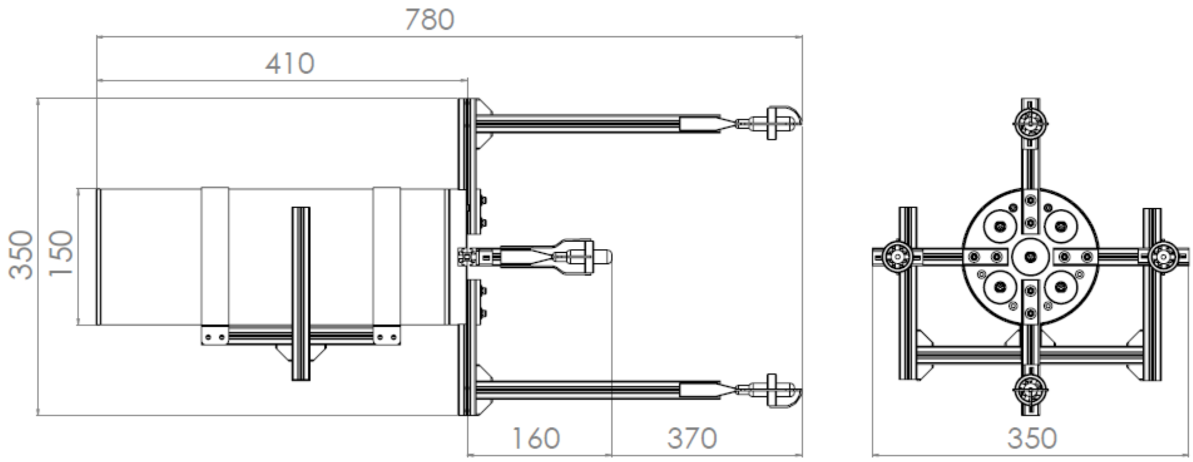

Figure 4.17: MAST/AM tool dimensions (mm).

For handling by the diver, a system with two vertical bars is assembled to the tool, each to one side of the tool, which the diver will use in order to maneuver the tool.

The final implemented prototype in Solidworks© of the MAST/AM tool is shown in Fig. (4.18b). The real prototype is displayed in Fig. 4.18b. Upon the implementation of the prototype it was seen that the tool weighted approximately 6 kg.

4.2.12 Connectors

During the description of the implemented design for the portable underwater tool, three forms of data communication from an outside source to the inside of the tool were reported: the signal received from the hydrophone array, signal sent to the transducer and the outbound Ethernet connection through the Ethernet switch. Such connections were only possible by resorting to connectors specially designed for underwater applications, able to withstand the hazardous conditions the underwater environment can produce.

Connection of the hydrophone array and transducer to the tool was implemented through an Impulse IE55 Connectors (Fig. 4.19a) [40]. This connector is used for power transmission and signal telemetry. Body and engaging nut are 316 Stainless Steel. The female of this connector is inserted at one end of the tool's (Fig. 4.19b).

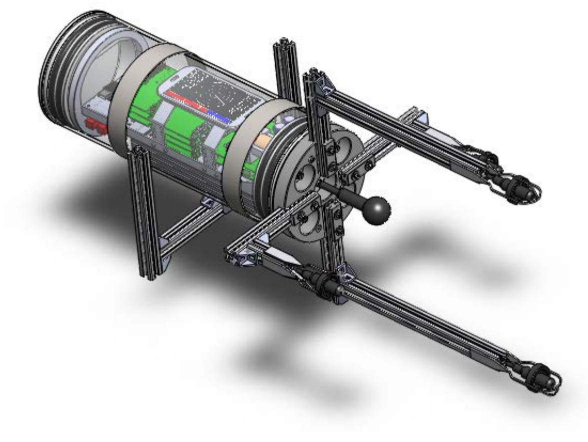

(a) Final prototype of the MAST/AM tool made in SOLIDWORKS©.

(b) MAST/AM portable underwater tool.

Figure 4.18: MAST/AM tool final prototype.

(a) IE55 connector and dummy.

(b) Hydrophones connected through the IE55 connector.

Figure 4.19: IE55 connector and pinout.

The pinout of the IE55 connector, according to Fig. 4.7, is presented on Table 4.6. Tho be noted that the transducer uses the central connector with pins 1&4 joined for GND and pins 2&5 joined for +Vtx. Pin 3&6 are not connected (NC) to avoid high arches.

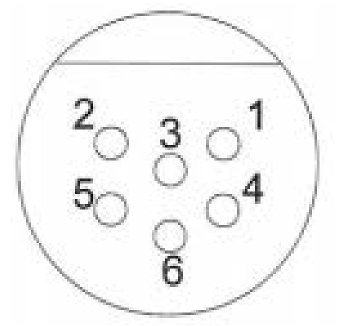

Table 4.5: IE55 connector pin.

Pin No.	Inside Tube	Hydrophone
1	$+Vdc$	Power ($5Vdc$ to $15Vdc$)
2	GND	GND
3	Signal	Signal
4	NC	NC
5	NC	NC
6	NC	NC

Table 4.6: IE55 pinout.

The Ethernet connection is made possible through a SubConn© 9 Contacts connector

(Fig. 4.20a) [67]. A SubConn© connector is designed to help prevent cathodic de-bonding caused by a difference in potential between the connector and surrounding equipment. The hard anodised aluminum is non-conductive and is stronger than other non-conductive materials. This connector enables an Ethernet connection, a Pulse Per Second (PPS) connection and power transmission, which may be used as power source for the tool. The female connector for the Subconn© is inserted in the opposite side of the hydrophone array (Fig. 4.20b).

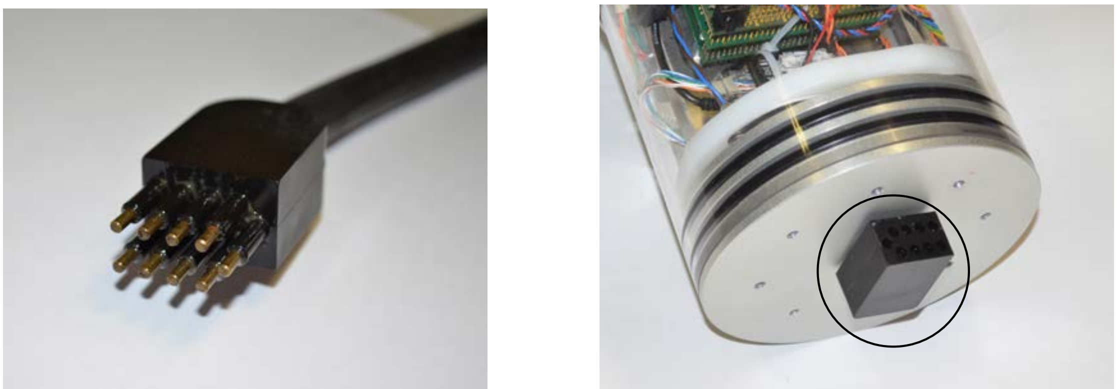

(a) SubConn© 9 Contacts connector.

(b) SubConn© female connector.

Figure 4.20: SubConn© connector and pinout.

In Fig. 4.20b, the pinout of the SubConn© connector is displayed, according to Fig. 4.20b.

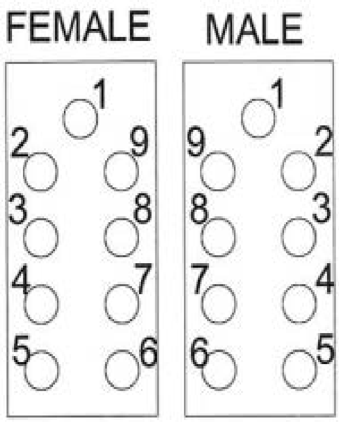

Table 4.7: SubConn© connector pin.

Pin No.	Description
1	TX+
2	TX-
3	PPS+
4	RX+
5	GND
6	SWITCH
7	RX-
8	PPS-
9	12.6 V(CHG)/11.1 V(BAT)(15VDC max)

Table 4.8: SubConn© pinout.

4.3 Software

The present section addresses Android development made in order to enable the Android device to be used in the MAST/AM tool and to implement an application which displays the result of the signal processing.

4.3.1 Android's Kernel replacement and driver installation

The present section addresses very specific details of the work that was necessary in order to make the Android device capable of being used in this architecture. The issues herein described deviate from the architecture, but are considerable relevant as they were essential for integrating the Android device in the MAST/AM tool. However, as they are extensive and not directly necessary for an overview comprehension of the tool, the reader is advised to proceed to the next section if he does not find the subject of Android development of interest.

In order to establish a connection between Android device and the DSP stack, it was necessary for the Android device to detect an Ethernet connection and attach an Internet Protocol (IP) address to it.

At first it was decided to use an Ethernet/USB adapter with an ASIX© [8] Integrated Circuit (IC). ASIX© is an electronics corporation whose ICs are widely commercialized, and thus, could be expected to provide a good database and possibly have a larger number of users who have dealt with making compatible drivers for Android.

The first attempt at compatibility between the ASIX© IC and the Android Device was to install, on the Android device, modules which usually come with the kernel [52] versions which make the kernel host compatible with this type of ICs, specifically, the "usbnet.ko", "asix.ko" and "mii.ko" modules. The "usbnet.ko" module acts as a driver for several kinds of network links over USB. This module is mandatory for acting as an USB host. "asix.ko" is a module which allows the device to detect an ASIX IC and establish a successful connection with the carrier of this IC. "mii.ko" gives support for Media Independent Interface (MII), which is the standard interface used to connect to a Fast Ethernet, which in turn is a term for Ethernet carrying traffic at the nominal rate of 100 Mbit/s. In this project, the kernel version used to compile said modules was an Android kernel source available at the Samsung© open source release center website [62] (device model: GT-I9305). Unfortunately, at the moment of installation of said drivers, a specific error occurred evidencing that the source code available did not exactly match the available GT-I9305 version even if it was the same model. Numerous baseband versions are available for each model, consequently the baseband of the source code available simply did not match the baseband of the available device. Without a compatible source code, any compiled module is ineffective.

The second step was to replace the available GT-I9305 running kernel with the one obtained from [62]. This operation was made possible by installing applications which would create a backup file of the Android device system. This backup file could be divided in two files: one with the current Kernel image (Kernel image is used for the first installation of the guest), and a second with user modification data (i.e installed applications, memory files). Afterwards, by replacing the first file with the outcome "bzImage" file (compressed Kernel image) of the Kernel downloaded from [62], it was possible to replace the Kernel version in the Android Device by rebooting the Android device from the new backup file (with the new "bzImage" file and the same data file). With the new kernel plus the modules defined in the previous paragraph, when connecting the Android device to the Ethernet/USB adapter, the Android device recognized the adapter. However, when connected to a PC, pings [50] would not be received and/or sent. The first explanation explored was that perhaps the ASIX© embedded in the new kernel was not working correctly. It is not available by default in the standard installation of the kernel and so one might suspect it is not yet fully functional, at least for the source code applied.

In order to validate the option presented in the end of the last paragraph, efforts were then directed to the installation of a standalone ASIX© driver: “Linux kernel 3.x/2.6.x Driver” [9], which is different from the ASIX© driver in the kernel. As a requirement, this standalone driver would have to be compatible with Android 4.x, as the firmware of the available Android device is version 4.1.2. Searching in the ASIX© database, it was found that only the AX88772 IC had drivers available for Android 4.x. Consequently, a Ethernet/USB adapter was obtained with said IC. With the new AX88772 IC device in hand, the driver was installed in the Android device. It is worth noticing, that this driver must be compiled upon the compiled kernel source code in order for them to be compatible. In practical terms, the compiling process of the driver must be directed to the location of the“bzImage” of the kernel in order to make settings compatible. More information about this process can be found at [71].

Although installation of the standalone driver in the Android device was successfully, the connection was still not working properly. However, this is probably not due to the driver, as it has been validated by ASIX©. Instead, this error was considered to be consequence of some difference in configuration between the replaced kernel and the new kernel, causing the new system in the Android device to show some flaws. As a matter of fact, some failures occurred in the normal use of device with the new kernel. Foremost the “Menu” and “Back” buttons embedded in the device were not functional and activating a Wireless Internet (WIFI) [18] connection was not possible. Despite the fact the kernel source code was distributed by Samsung© for this model, and thus bugs should not be common, one must recall that the source code acquired was for a different baseband version, not for the specific device available, and, consequently, it may very well be the case of a non adequate configuration. The kernel configuration file defines the type, the number and the characteristics of the devices supported by the kernel as well as several kernel configuration options.

When replacing the kernel of an Android device, the first advice to be given is to pull the configuration file of the kernel embedded on the device factory settings and apply it to the new kernel source the user might wish to install. Although the source code already has a standard configuration file, it may not be the correct one to said device. Given that most international versions of the produced devices often present some changes, this is a common cause of error. One may ask why was is then that this procedure was not done for this project. However, the configuration of the default kernel of the device is only possible to be uploaded (usually from “/proc/config.gz”) in case upon configuration of the said kernel the option “IKCONFIG_PROC” was enabled. Hence, only some Android devices have this file. Unfortunately, for the available Android device this was not the case, and the proper configuration was not possible to be obtained.

Taking into account the limitations of the Samsung© open source website, given only one configuration was available, which produced an incorrect result, efforts were directed towards other Android kernel versions. The aim was to obtain a GT-I9305 source code version fully compatible with the available device. These non official versions are often produced by enthusiasts of the Android operating system not related with any brand, which intend to develop aftermarket firmware based on the open-source Android operating system, adding and modifying features from the official Android based firmwares. Opposed to companies such as Samsung©, which may release some standard version of their kernel for the potential of some of their most critical bugs being resolved by developers outside the company, but are not committed in releasing all code for market reasons, this independent sources are fully committed in releasing their products as their profit is a direct result of it. Accordingly, their products are expected to cover a much larger number of users and devices. The firmware distributions considered were the ones which are, nowadays, the most popular among the android community, specifically Boeffla-Kernel© ([16]) and CyanogenMod© ([24]). The former was intended and produced for the GT-I9300 model (Samsung© Galaxy SIII previous version of the GT-I9305 model), and, unfortunately, did not behave in the best way for the GT-I9305. However, CyanogenMod© functioned properly in the device, and after installation of the ASIX© standalone driver "Linux kernel 3.x/2.6.x Driver", connection with the USB/Ethernet adapter was established successfully.

The correct behavior of the circuit comprising the USB/Ethernet adapter and the Samsung© Galaxy SIII GT-I9305 was tested by connecting the adapter to a router. Having established the connection, it was observed that the GT-I9305 was able to ping any PC within the network, as well as receive any ping from any PC. Afterwards, an Android application was designed in which the GT-I9305 would behave as a client, establish connection to a server and exchanging packets. Selecting the GT-I9305 as the client end was intentional, as the DSP behaves as a server, and given the fact that the GT-I9305 connects to the DSP it will act as a client. Hence, this application was already a preparation of what would happen in the final prototype. The application performed as expected, and data was received and sent from the GT-I9305 successfully.

4.3.2 Visualization Application

For visualization of the target's position, a graphical application to run in the Android device was developed. Said application used the software "ECLIPSE" [33] and the code was written both in Java and Android Application Programming Interface (API), protocol intended to be used as an interface by software components to communicate with each other.

The main goal of the design phase was to create an *user-oriented* interface which could be correctly interpreted without the need of previous training. Additionally, the interface employs colors with a clear contrast between them, so the displayed information could somewhat be interpreted with peripheral vision.

The screenshot of said application can be seen in Fig. 4.21. In the left side of the screen, the diver can visualize an object very similar to a compass which will point the direction of the transmitter in the same plane as the diver. The distance in the previous plane is also visible through red circumferences. The farther the diver is from the transmitter, the larger is the radius of the red circumference, and vice versa. In the right side, a vertical bar displays the distance between the diver's and the transmitter's depth. If both are at the same depth, the percentage of blue and red in the bar will be equal. If the diver is at a higher depth, the percentage of red will be bigger, denotative that the diver must lower its depth. As the diver decreases its depth, the red bar decreases in size, meaning the diver's depth is getting closer to the transmitter's depth. If the diver is at a lower depth, the red bar will be smaller than the blue bar, meaning the diver must increase its depth. In the bottom of the screen, is also visible a written information concerning the angle, distance and depth difference towards the transmitter.

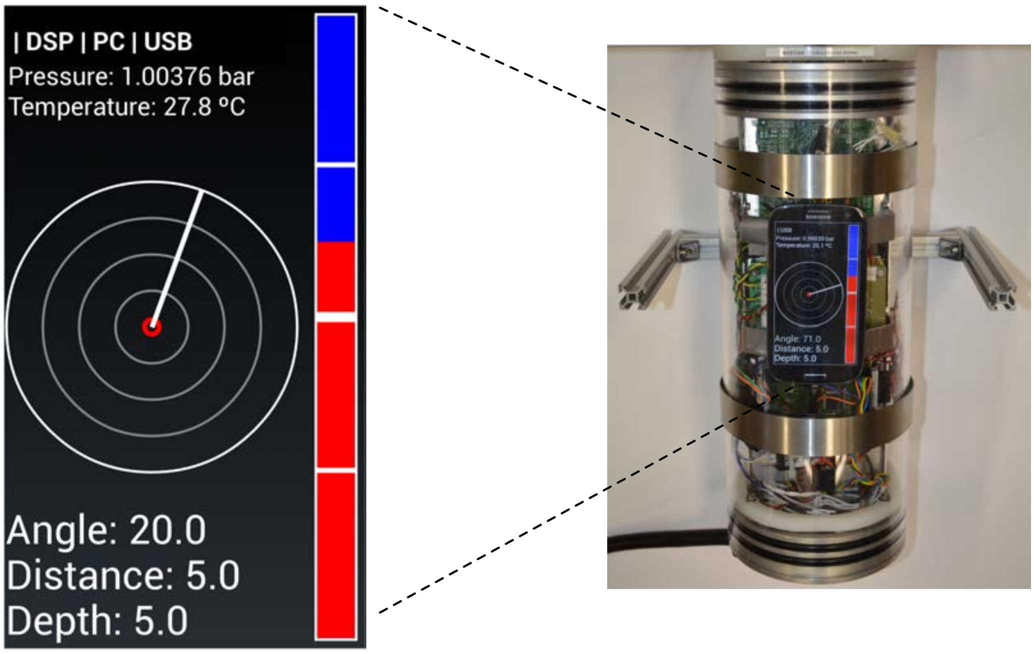

Figure 4.21: Diver graphical user interface.

5 | System Validation and Assessment

This chapter addresses the validation of the portable underwater tool prototype created for the project MAST/AM. At the time of the first sea trials, the hardware had already been validated at the laboratory, and the overall system worked as expected. The hydrophones successfully acquired the signal. The Android device received data from the DSP, from the outbound Ethernet connection and from the BMP05 sensor, displaying it on the screen in the most convenient way for the user. The interrogator was also tested, and a signal was produced. It can be considered that, at this time, the results which were under the scope of this thesis were successfully accomplished. However the system altogether could not be tested at sea monitored by a diver for reasons outside the extend of this thesis although concerning the ambit of the MAST/AM project.

The first experiment at sea was conducted at Albufeira Bay, Portugal, July 19^{st}. On this date, reluctance still existed on the possibility of computing direction with the signal originated by the VEMCO© tags. The main restriction laid on the properties of the signal (recall 2.1.4. As software was still not validated, during the experiment the tool was not immersed, as it was preferred to use this experiment for recording signals received through the hydrophone stack and afterwards processed them in laboratory. The tool's electronics were aboard the vessel (Fig. 5.1a), with the tag in a known position at sea. The hydrophone array was securely attached to the starboard of the vessel (Fig. 5.1b), submerged under approximately 2 m of water. The movement of the array was restricted, but not entirely as to avoid structural stress, damages and unwanted vibrations. The movement of the vessel was recorded through GPS and is displayed in Fig. 5.2.

The experiment results showed a successfully acquisition of the signal, including at a distance to the transmitter of over 220 m. However, unfortunately,the outcome of said estimation showed both a large variation from correct values and randomness throughout the entire experiment duration. Theoretical analysis upon sinusoidal signals, confirmed that for direction results with a reasonable degree of certainty to be obtained, a higher SNR was required. However, it also also observed that the AGCAMP introduced a high amount of noise. In order to assess the culpability of the AGCAMP in the poor results of the experiment, efforts were redirected at experimenting with different signals with greater evidence of success, namely resorting to SS methods (recall section 2.2), where the output of the AGCAMP would be compared to the output of another signal amplifier.

For the second experiment set, a signal producing system was connected to a transducer

(a) Tool electronics aboard the vessel. (b) Hydrophone array attached to the bow.

Figure 5.1: Albufeira experiment.

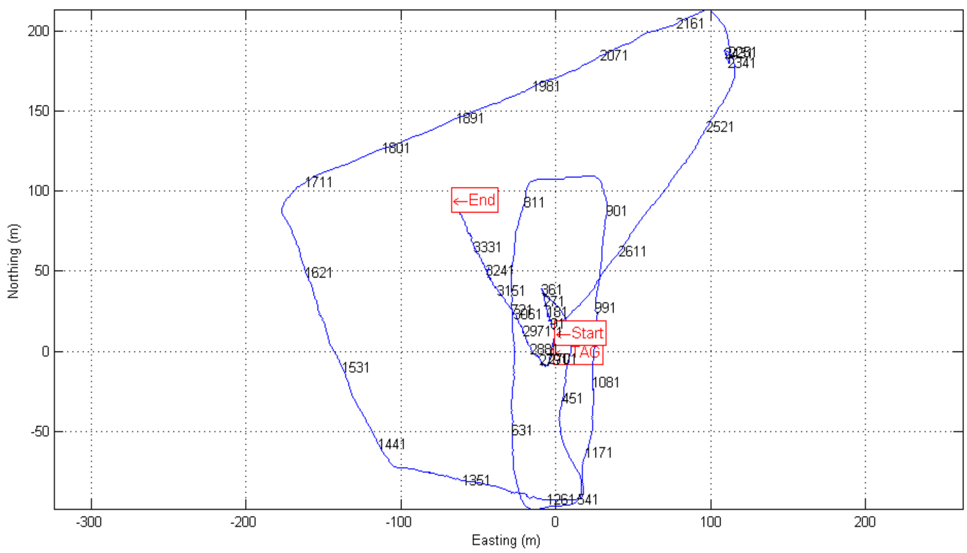

Figure 5.2: Trajectory of the boat during experiment at Albufeira Bay, Portugal.

for generating the transmitter signal. Nevertheless it is necessary to state that due to the reduced amount of time remaining, the new experiment followed the same procedure of data recording and subsequent analysis in the laboratory. This experiment was conducted at Belém dock, Portugal, October 4^{th}.

Fig. 5.3 display the various locations where the transducer was positioned with respect to the hydrophone array at the origin of the arrows. Each location will be designated by the number adjoining the arrow targeted to said location. It is admitted that all positions are at the same altitude. The distances between positions were calculated according to their GPS positions. The signals produced by the transducer, at each location, were analyzed. Different directions of the USBL array were considered for each experiment. The reader must take into consideration that the placement of the array in a given direction was carried out manually. Hence when we expect, for example, a $0°$ by positioning the array directed to the transducer, this is a $0°$ read by the human eye. In reality, this may easily be an angle of a small value, but not null.

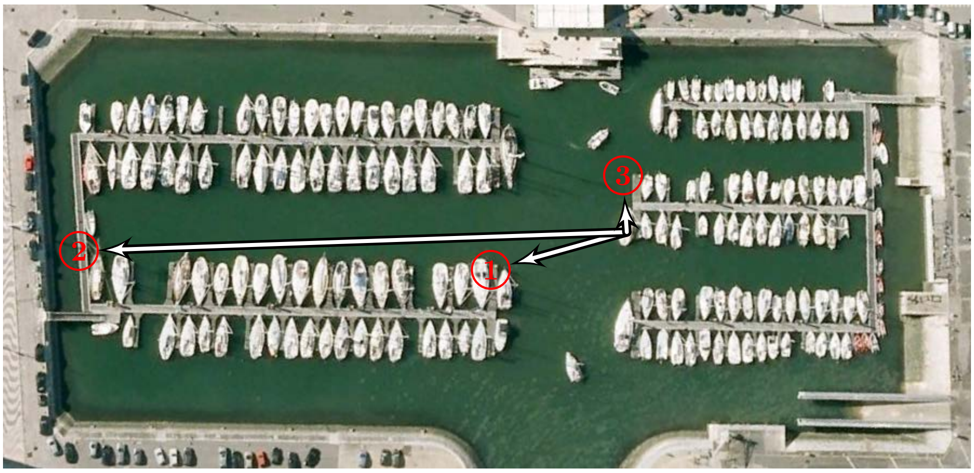

Figure 5.3: Belém dock sea trials setup.

Results showed signal peaks clearly outline, as opposed to the experiments with sinusoidal signals, which improves the probability of success in calculating directions and distances. Table 5.1 presents the outcome of the direction and distance calculation when the transducer was at the position indicated. The values presented are the output of a median filtering of the raw signals in order to lessen the effect of outliers.

Transducer Position	1		2		3	
	Mean	σ	Mean	σ	Mean	σ
USBL Heading **(expected)** (°)	8.1536 (**0**)	3.67	2.46 (**0**)	1.59	23.29 (**0**)	9.09
Distance **(expected)** (m)	39.9 (**38**)	2.23	135.85 (**132**)	2.86	11.04 (**12**)	1.44

Table 5.1: Results from the experiment at Belém dock.

The results are very satisfactory considering the high probability for measuring errors is such location. Firstly, the depth is diminutive which results in a continual multipath caused by reflections from both the surface and ground of the water column. Secondly, the existence of several vessels also gives rise to additional reflection. It should also be taken into account that the placement of the array in a desired direction for testing was carried out manually, and hence a constant random error must be accounted for. Additionally, an irregular deviation is accredited due to the undulation of the water column (waves), which displaced both the hydrophone array and the transducer. It is also worthy of mention that the poor quality of position 3, regardless of its close proximity, is probably due to to reflections induced by a vessel stationed between position 3 and the hydrophone array at the time of the experiment. Lastly, it must be noted that for the propagation velocity of sound in water an overall value was used. It can be expected that this value differs from the one at the test site, affecting the accuracy of the results.

During experiments the AGCAMP performance was tested against the performance of a Voltage Gain Amplifier with Band-Pass Filter (VGAMP) (annex D.8), which is a low noise amplifier/filter board, whose gain is assigned by the user directly in the card. This test was performed with both amplifiers acquiring the same signal in order to fairly compare the two cards. Two hydrophones in the same position of the xy plane of $\{B\}$ were used. Each card was connected to a different hydrophone. Fig. 5.4 show the output of the AGCAMP ant VGAMP, respectively. Based on the results obtained it can be stated that the VGAMP card has a better SNR, however at the expense of a greater power consumption, which results in a reduced battery life. Weighting on which card to employ should be made based on the mission profile. With respect to the VGAMP card, it is worth noting that it differs from the AGCAMP in terms of power supply. The latter requires a power supply of 12 V, whereas the VGAMP requests one of ±5 V. Consequently, in mission profiles where the VGAMP is preferred, another SWLNPWR card is to be added to the tool's architecture with an output power of ±5 V in order to power the VGAMP stack through which the signal acquired by the hydrophone array will be amplified.

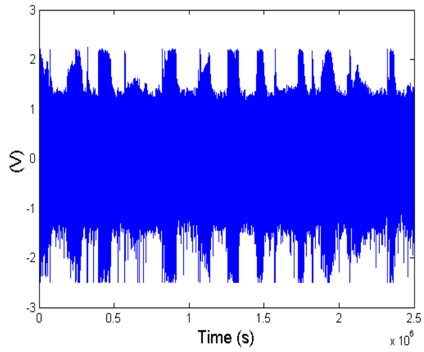

(a) Output of the AGCAMP.

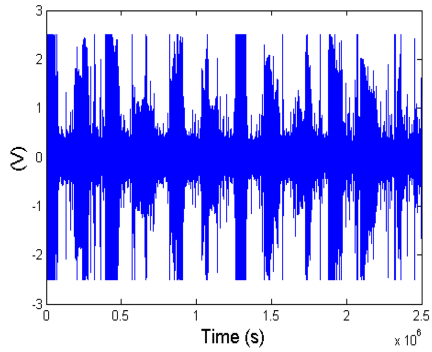

(b) Output of the VGAMP.

Figure 5.4: Comparison between signal output of AGCAMP and VGAMP.

Overall, regarding the implementation of the designed prototype, experiments often conducted in laboratory of the complete system and of the signal acquisition system tested in real environment were successful. The objectives initially set for the portable underwater tool were accomplished as the tool intended performance was implemented successfully. Unfortunately, initial guidelines for the MAST/AM project were not met in full, as with VEMCO© tags results obtain were far less satisfactory. The initial intention of designing a prototype was attained with the slight misfortune of requiring transmitters dissimilar of the ones assembled by the VEMCO© brand.

The latter cannot however be seen as a flaw of the MAST/AM project. The project aimed at producing a low-cost tool portable underwater tool capable of tracking tags inserted in marine animals. Such was accomplished as proven by the latter results. Unfortunately, results with the VEMCO© were not satisfactory, due to the signal properties. However, it was proven that with a different signal, the processing of the signal done by the MAST/AM tool was successful.

6 | Conclusion and Future Work

This thesis addressed the design of an USBL/INS prototype system architecture to be inserted in a cylinder tool of small size and weight so it may be carried by a diver underwater. The work was carried out and tested in ISR/IST in the scope of the MAST/AM project. The main contributions of this thesis are associated with the development of a tool, not available in the market, to be used in the framework of marine biology.

Regarding surveillance and tracking missions of marine animals, nowadays these are conducted with the single information of the marine animal being within a large area, around and with origin on the receiver, given the transmitter signal is received. This uncertainty as to the location of the transmitter causes several limitations in the progression of tests and studies. This projects now offers a tool can be easily carried and is capable of presenting direction and distance of the transmitter in real-time.

The prototype is capable of acoustic signal acquisition, being assembled with an acoustic array, and processing provided by a DSP. The computed results are delivered to an Android device which will display the data to the diver, along with pressure and temperature values inside the tool. The tool is also equipped with an underwater acoustic interrogator unit, required for certain navigation filters for communication with a vessel at surface. The final architecture prototype was successfully validated with experimental data obtained at sea. It proved to be fully functional, low cost and and low power enabling continuous operation of approximately 5.6 hours.

Before providing comments on future directions of work, it is important to point out current technical limitations of the initially proposed project. Initially, the MAST/AM tube was intended to be compatible with VEMCO© tags, as said tags were widely adopted by the scientific community. The preference for said tags relies on their diminished size, which enables them to be inserted in marine animals. By ensuring that the tool could be used with this tags, it would not be necessary to purchase new emitters thereby increasing the range of applications of this prototype. However, satisfactory results with these tags were not obtained. It was hence necessary to limit the range of uses of the tool to certain transmitter signals with more distinct variations over time. Nowadays, tags of similar size with different signal features are still not available on the market, which leads the tool to be only compatible with emitters of larger dimensions.

Despite the previously described limitation, the final prototype is nonetheless a tool of surplus value given the innovation it represents and the benefits it provides for underwater tracking missions. It is expected that with the continuous development of minimum size tags, the potential of this product will grow proportionally. Additionally, given the growing interest in the development of tools for applications of similar operating scenarios, the MAST/AM is undoubtedly a relevant project.

Concerning future work, efforts would certainly be directed towards the development of practical and small dimensions emitters with different signal properties that the ones observed in VEMCO© transmitters, or even development of processing and signal acquisition techniques which would eventually allow the use of the existent VEMCO© tags. It is also of importance to bear in mind that the project was conducted under academic purposes, it is still at a prototype phase, and all individual components were assembled together. If it were to be applied to a more commercial environmental, fabrication of components specific for this tool would certainly avail to diminish both size and weight of the tool further increasing its potential use.

A Matched filter and Correlation Function

The present chapter addresses the prove of proportionality between the output of the matched filter and the input signal cross-correlation with a replica of the transmitted signal, except for the time delay T.

The cross-correlation function $R(t)$ of signal $y(t)$ and $g(t)$ is as follows:

$$R(t) = \int_{-\infty}^{\infty} y(\lambda)s(\lambda - t)d\lambda. \tag{A.1}$$

Both $y(t)$ and $g(t)$ have a finite duration.

Considering $y_{out}(t)$ the output of a filter with impulse response $h(t)$ and input $y_{in} = s(t) + n(t)$:

$$y_{out}(t) = \int_{-\infty}^{\infty} y_{in}(\lambda)h(t - \lambda)d\lambda. \tag{A.2}$$

If said filter is a matched filter: $h(\lambda) = s(t_1 - \lambda)$, and equation (A.2) becomes:

$$y_{out}(t) = \int_{-\infty}^{\infty} y_{in}(\lambda)s(t_1 - t + \lambda)d\lambda = R(t - t_1). \tag{A.3}$$

The output of matched filter corresponds to the cross correlation between the received signal corrupted by noise and a replica of the transmitted signal.

B | Vehicle INS simulation

Fig. 3.16 displays the *Simulink* model for the implementation of the vehicle's simulation presented in section 3.7.

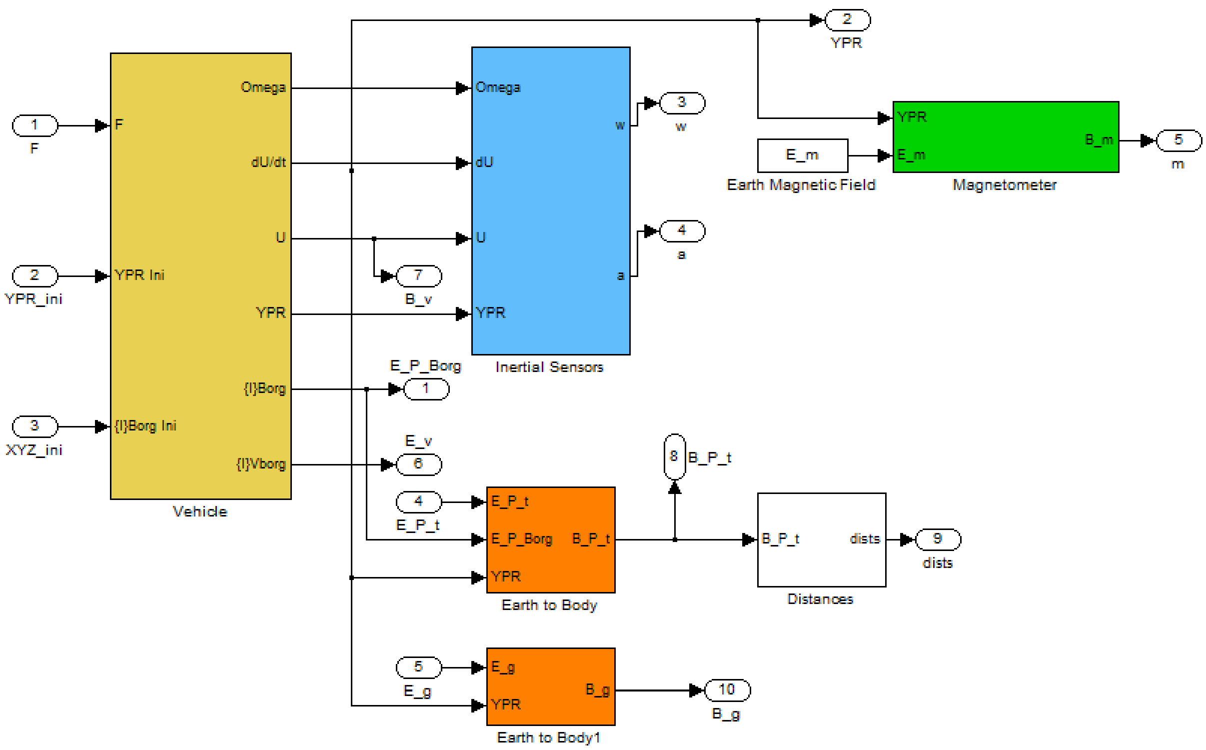

Figure B.1: *Simulinks* block diagram for the vehicle's simulator implementation. Source: [55].

In block "Vehicle", the vehicle's movement is simulated taking into account the forces applied to the six propellers. Table B.1 displays the vehicle's dimensions and weight, which were introduced according to the characteristics of the MAST/AM tool. The IMU's position is assumed to be coincident with the center of mass of the vehicle for reasons of simplicity.

Block "Inertial Sensors" simulates the signals produced by the IMU system. Noise was added according to the specifications of the strapdown system employed in the MAST/AM tool.

Block "Earth to Body" transforms a simulated movement of the transmitter in Inertial Frame into the Body Frame. In combination with the Euler angles of the vehicle, and its position in Inertial frame, the position of the transmitter in $\{B\}$ is attain.

Foremost, for calculation of the position of transmitter in $\{B\}$, to the transmitter's position

Mass (kg)	13
Height (m)	0.15
Width (m)	0.15
Length (m)	0.41
Propellers 1 (m)	$[-0.205, \pm 5{,}0]^T$
Propellers 2 (m)	$[0, -0.075, \pm 5]^T$
Propellers 3 (m)	$[-0.15{,}0, \pm 0.075]^T$
Sensors' position (m)	$[0{,}0{,}0]^T$

Table B.1: Vehicle's characteristics.

in Inertial Frame is subtracted the position of the vehicle in Inertial Frame. Following, it is the necessary to recall the rotation matrix (3.15) used for transformation between frames. Considering (3.2):

$$^{E}P = ^{E}_{B}R\ ^{B}P. \tag{B.1}$$

The Euler angles are used in $^{E}_{B}R$. ^{B}P is obtain by multiplying ^{E}P by the transpose of matrix $^{E}_{B}R$.

C | Simulik Model for the Complementary Filter for Pitch Estimation

Fig. C.1 illustrates the *Simulink* model used for pitch estimation through a complementary filter. The inside of block "Complementary Filter" is displayed in Fig. C.2.

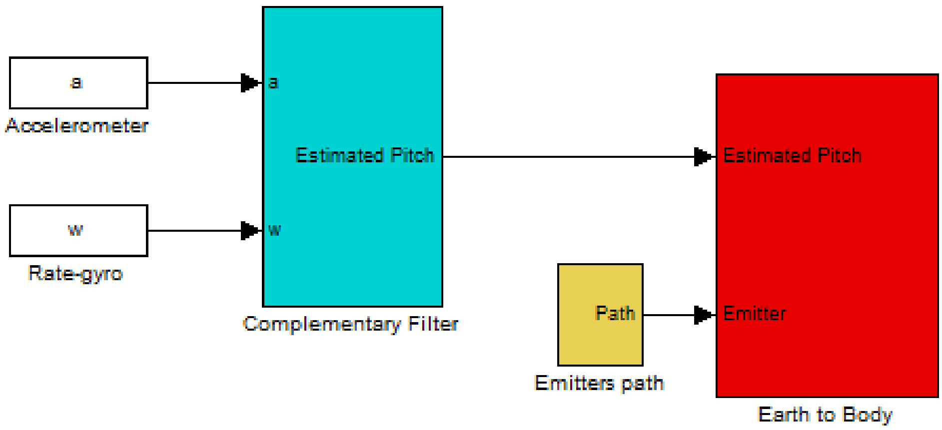

Figure C.1: *Simulink* Model for Complementary Filter for Pitch Estimation.

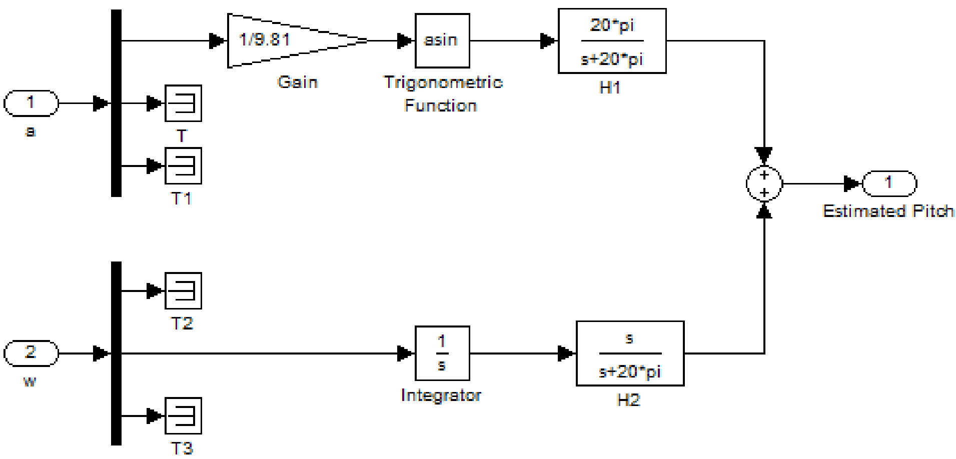

Figure C.2: *Simulink* Model for Complementary Filter for Pitch Estimation.

The pitch rotation (θ) from the accelerometer is calculated through the acceleration felt in the x axis. Fig. C.3 displays the relation between $\{B\}$ and NED frame.

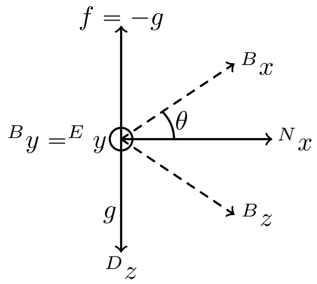

$$\mathbf{f}_x = g \times cos\left(\frac{\Pi}{2} - \theta\right) = g \times sen(\theta), \quad \text{(C.1)}$$

Figure C.3: Acceleration forces in $\{B\}$.

In (C.1), $\mathbf{f}$ corresponds to the acceleration measurement in $\{B\}$, and g is the gravity force. In turn, for the rate-gyro:

$$\dot{\theta}\Big|_{\phi=0} = w_y \;\; ; \;\; \theta(t) = \int_{-\infty}^{T} w_y(\tau) d\tau + \theta_0, \quad \text{(C.2)}$$

where w is the rate-gyro measurement and ϕ is the roll rotation.

D | Hardware developed at ISR/IST

D.1 Automatic Gain Control Amplifier (AGCAMP)

The AGCAMP board (Fig. D.1) is a very low noise, low power and single supply automatic gain control amplifier with a user selectable maximum gain and dynamic gain range.

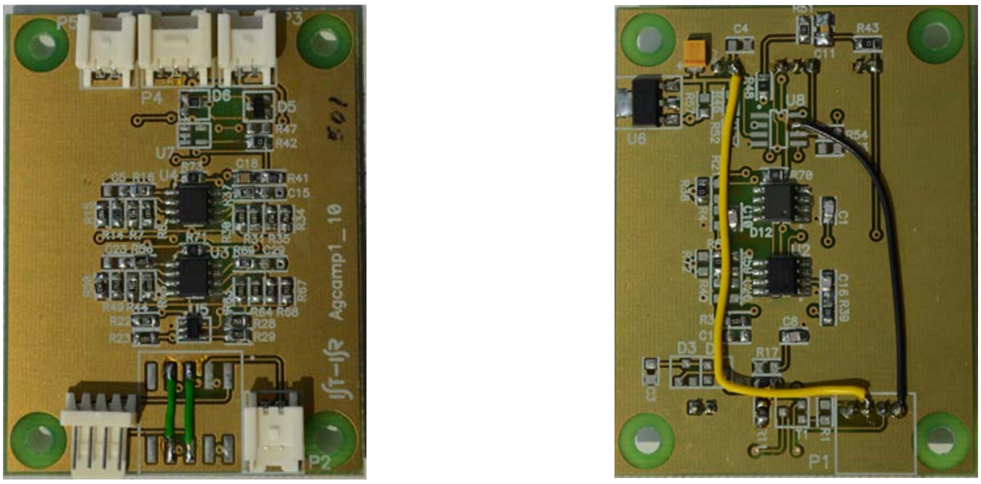

(a) Upper layer. (b) Bottom layer.

Figure D.1: AGCAMP board.

A block diagram of the AGCAMP board is shown in Fig. D.2. The AGCAMP board consists of an input passive band-pass filter stage, a preamplifier, and four equal automatic gain control amplifier stages. Each stage consists of a voltage controlled attenuator, an amplifier and a feedback loop composed by an envelope detector and a low pass filter.

D.2 Battery Monitor (BATMONIT)

The BATMONIT board (Fig. D.3) main function is the monitoring of both charge and discharge of a battery. Additionally, it is capable of detecting hazardous charge and discharging conditions. In said conditions, this board disconnects the charger or the load to which it is connected, thereby protecting the battery.

The BATMONIT board has two main circuits: microcontrollers Atmel AVR AT90CAN128 [12] and Fuel Gauge Maxim max1660 [11]. The latter executes two essential functions for

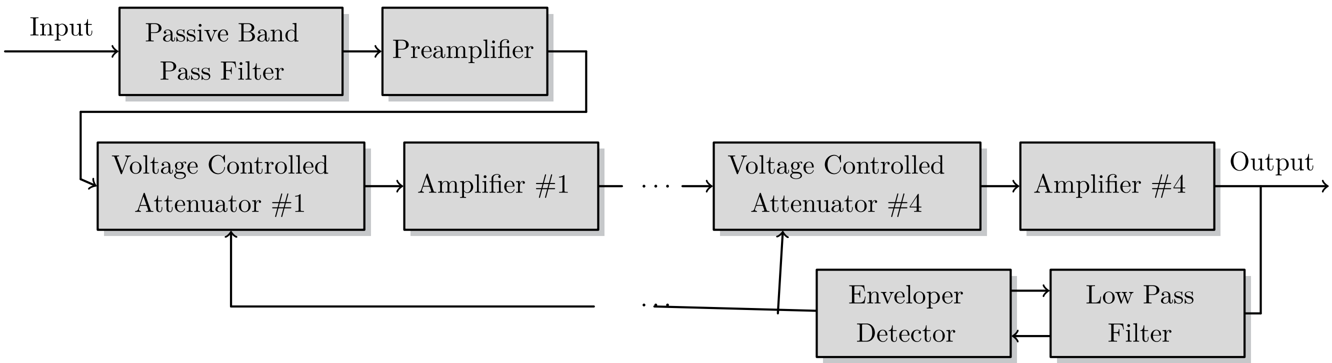

Figure D.2: AGCAMP block diagram.

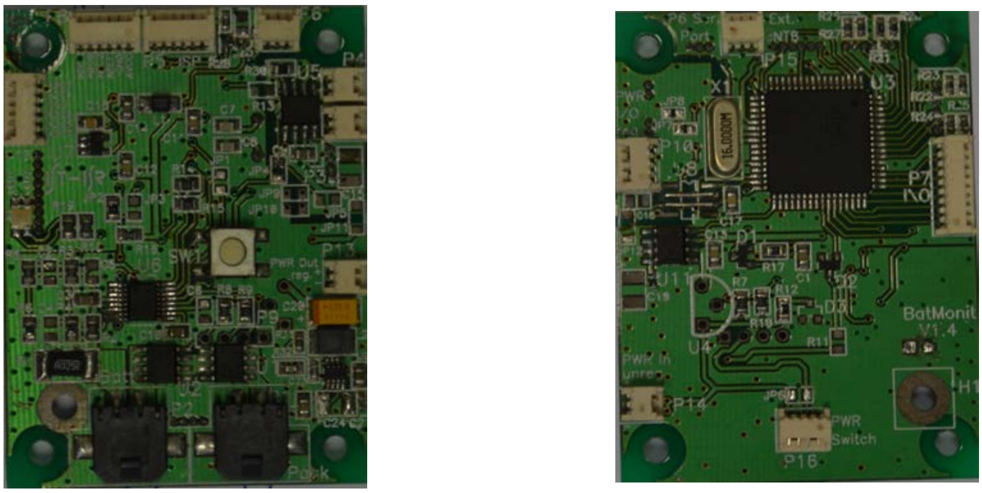

(a) Upper layer.

(b) Lower layer.

Figure D.3: BATMONIT board.

rechargeable battery-pack management: fuel gauging and pack overcurrent protection. It accurately monitors a battery pack's charge and discharge current flow, and records each using two independent, on-board Coulomb counters. Further specifications of the Fuel Gauge max166 are as follows:

- 1% Accuracy over a $600\,\mu$A to $4A$ Current Range ($R_{SENSE} = 30\,\text{m}\Omega$)
- $5\,\mu$V Input Offset Voltage ($28\,\mu$V max)
- SMBus 2-Wire (plus optional interrupt) Serial Interface
- $2V$ Precision System Reference Output
- $3.3V$ Linear-Regulator Output Powers External Circuitry
- Two Micropower Shutdown Modes
- Independent 32-Bit Charge and Discharge Coulomb Counters
- Battery-Overcharge/Overdischarge Protection

- Battery Short-Circuit/Overcurrent Protection
- On-Board Power MOSFET Drivers
- 80 μA Quiescent Current

D.3 Class D Power Amplifier (PWRAMPD)

The PWRAMPD board (Fig. D.4) is a highly efficient class D switch mode amplifier board in a full bridge configuration. This form of amplifier technology provides particular benefit in the high power ranges where operating efficiencies as high as 90% can be achieved to dramatically reduce heat sinking requirements. This board is optimized to drive acoustic transducers and to be driven by a PWM waveform with a maximum frequency of 1 MHz.

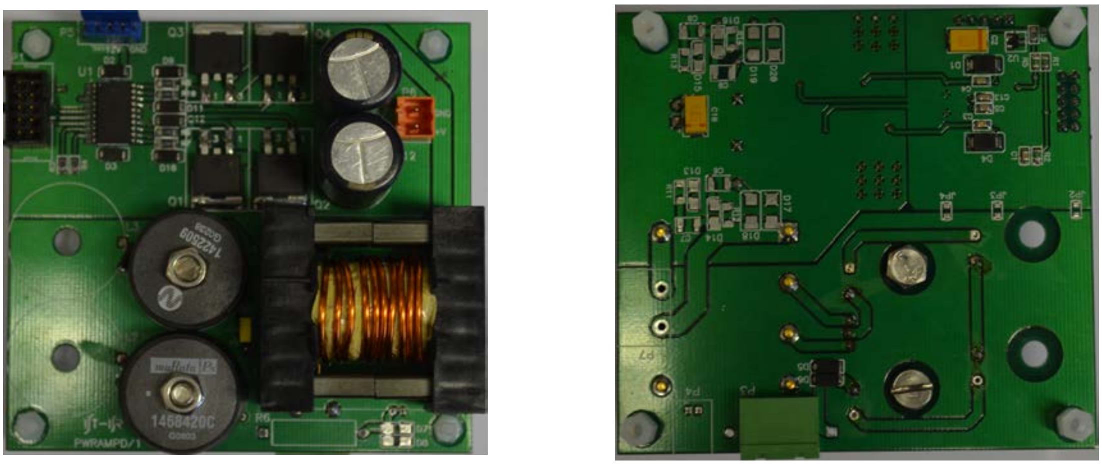

(a) Upper layer.

(b) Lower layer.

Figure D.4: PWRAMPD board.

A block diagram representative of the PWRAMPD board can be seen in Fig. D.5. The PWRAMPD board consists of an input H bridge driver, an H bridge N channel MOSFET, a Snubber circuit, a voltage step-up circuit and an impedance matching circuit. The input H bridge driver is implemented by a high frequency, medium voltage Full Bridge N-Channel FET driver IC, the HIP4080A from Intersil Corporation, the H bridge N channel MOSFET consists of four N channel low voltage and low resistance gate to source MOSFET, the IRF3205 from International rectifier. The step-up circuit and impedance matching circuit are implemented by a voltage transformer and a power inductor. The Snubber circuit consists of a simple resistor capacitor diode network.

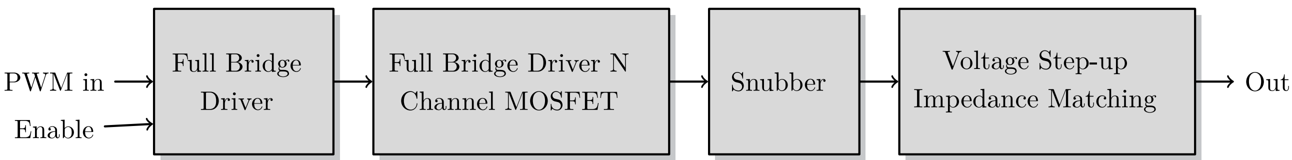

Figure D.5: PWRAMPD block diagram.

Further specifications of the PWRAMPD are as follows in table D.1.

Supply Voltage	$+12V$
Maximum Supply for power stage	$+80V$
PMW signal input	$+5V$ up to $+12V$
Disable input	$+5V$ up to $+12V$
Power Loss at $10A$	$1.6W$
Efficiency at $10A$	87%
Maximum Switching Frequency	$+5V$ up to 1 MHz
Maximum Continuous Current	$+5V$ up to $15A$

Table D.1: PWRAMPD specifications.

D.4 Microcontroller AVRCAN128

The microcontroller AVRCAN128 (Fig. D.6) behaves as a system of generic user interface for sensors and actuators.

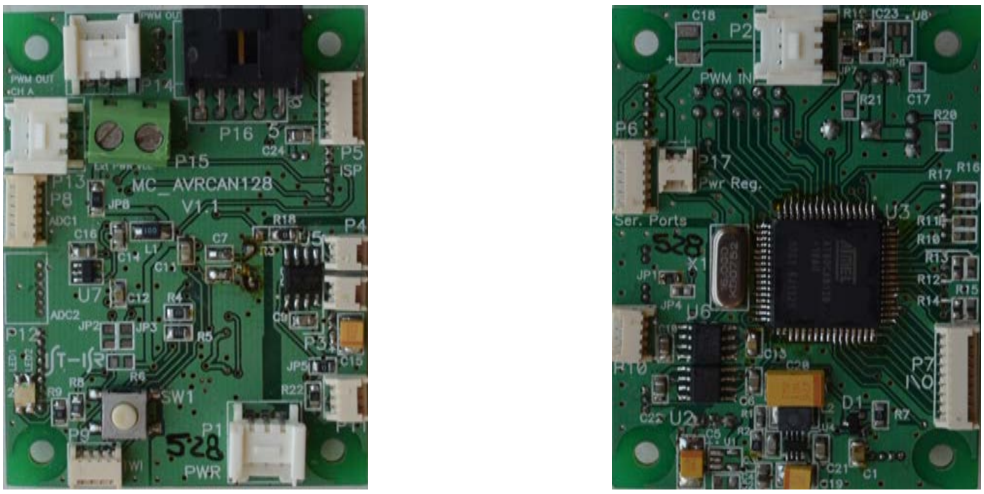

(a) Upper layer. (b) Lower layer.

Figure D.6: Microcontroller AVRCAN128 board.

This board is built around the microcontroller Atmel AVR AT90CAN128 [12], whose specifications are described below:

- Advanced Reduced Instruction Set Computer (RISC) architecture
- Non volatile Program and Data Memories
- CAN Controller 2.0A & 2.0B
- Programmable Watchdog Timer with On-chip Oscillator

- 8-bit Synchronous Timer/Counter
- 8-bit Asynchronous Timer/Counter-2
- Byte-oriented Two-wire Serial Interface, Dual 16-bit Synchronous Timer/Counters
- 8-channel, 10-bit SAR ADC
- Dual Programmable Serial USART, Master/Slave SPI Serial Interface
- 8 External Interrupt Sources, 5 Sleep Modes
- Operating Voltages from 2.7 V to 5.5 V
- Maximum Frequency: 8 MHz@2.7 V and 16 MHz@5.5 V

The peripherals of the microcontroller AVR AT90CAN128 were made into connectors in order to enable interface with the outside. The available interfaces are listed below:

- CAN bus
- Two-Wire Interface (TWI)
- SPI
- 2 PWM generation channels and 1 reception 16 bit channel
- Parallel input/output port of generic use

The CAN bus is a vehicle bus standard designed to allow microcontrollers and devices to communicate with each other without a host computer.

D.5 Power Connector (PWRCONN)

The PWRCONN board (Fig. D.7) receives power from two power sources and generates four output channels for each power supply, with output voltage equal to the input voltage.

D.6 Power Supply/Can opto-isolation and termination/RS-485 board (PWROPT0485)

A PWROPT board (Fig. D.8) is a DC-DC converter board.

This board has two high performance DC-DC converter modules, whose specifications are shown in table D.2.

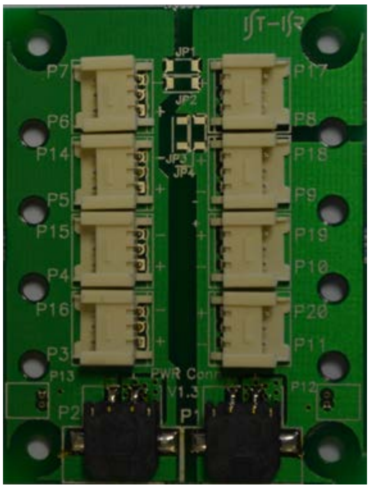

(a) Upper layer.

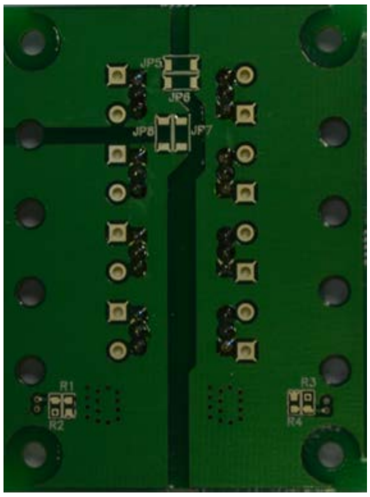

(b) Lower layer.

Figure D.7: PWRCONN board.

(a) Upper layer.

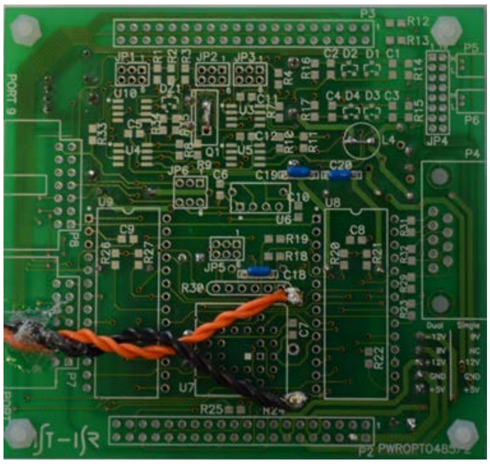

(b) Lower layer.

Figure D.8: PWROPT0485 board.

Model	Input voltage range	Output Voltage	Maximum Output Current	Efficiency
TEN 10-1221	$9V - 18V$ DC (12 VDC nominal)	$\pm 5VDC$	$\pm 1A$	78%
TEN 15-2410	$9V - 36V$ DC (24 VDC nominal)	$3.3VDC$	$3A$	80%

Table D.2: PWROPT's DC-DC converters specifications.

D.7 Switching Low Noise Power (SWLNPWR)

The SWLNPWR board (Fig. D.9) contains four high efficiency switching power supplies designed to be able to generate regulated voltages from a single voltage source, which may vary between +2.7V and +24V. The output voltage of each source is switched individually by configuration through a resistive circuit and can vary between +3V and +24V. The SWLNPWR board has a low noise advantage, as well as a small size and weight.

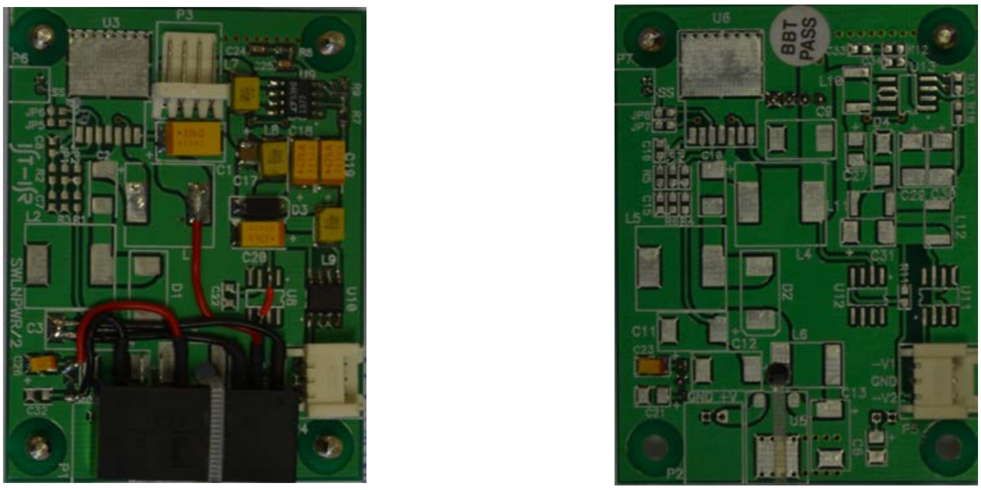

(a) Upper layer. (b) Lower layer.

Figure D.9: SWLNPWR board.

A block diagram representative of the SWLNPWR's functioning can be seen in Fig. D.10.

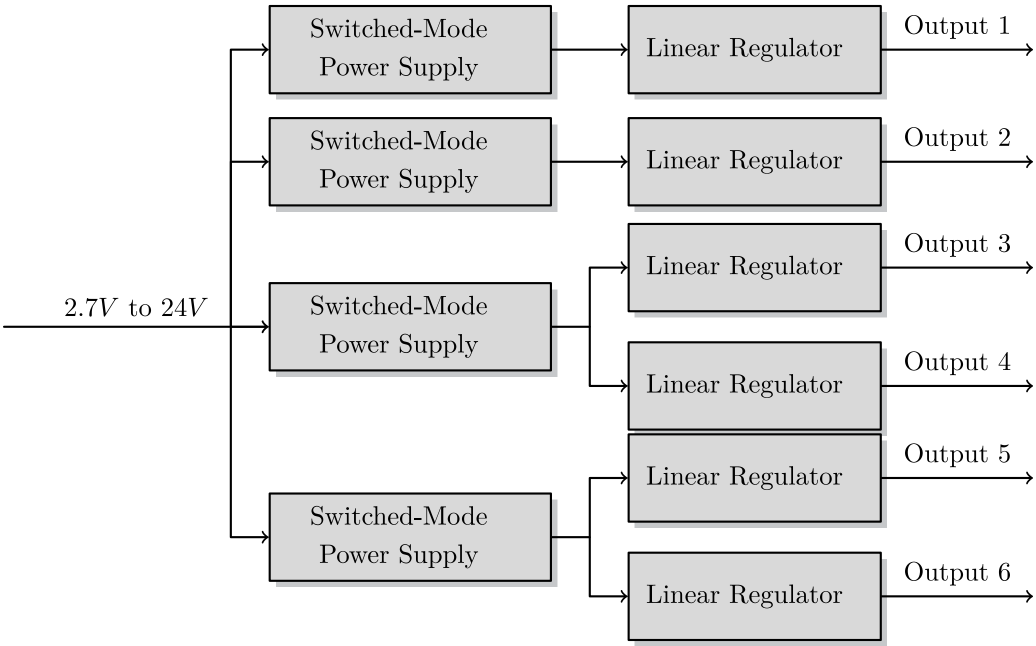

Figure D.10: SWLNPWR block diagram.

Further specifications of the SWLNPWR are as follows:

- Maximum output current equal to 1.5A (750 mA with linear regulator).
- Both positive and negative output voltages.
- Low noise optional output voltage of 1 μV (0.1 Hz - 10 Hz) at 15 mA.

D.8 Voltage Gain Amplifier with Band-Pass Filter (VGAMP)

The VGAMP (Fig. D.11) board is a very low noise amplifier/filter with an user selectable fixed gain up to 60 dB or linear-in-dB variable gain amplifier (VGA) and aButterworth, Bessel or Chebychev 4^{th} order band-pass filter. This board is optimized for time-based variable gain control.

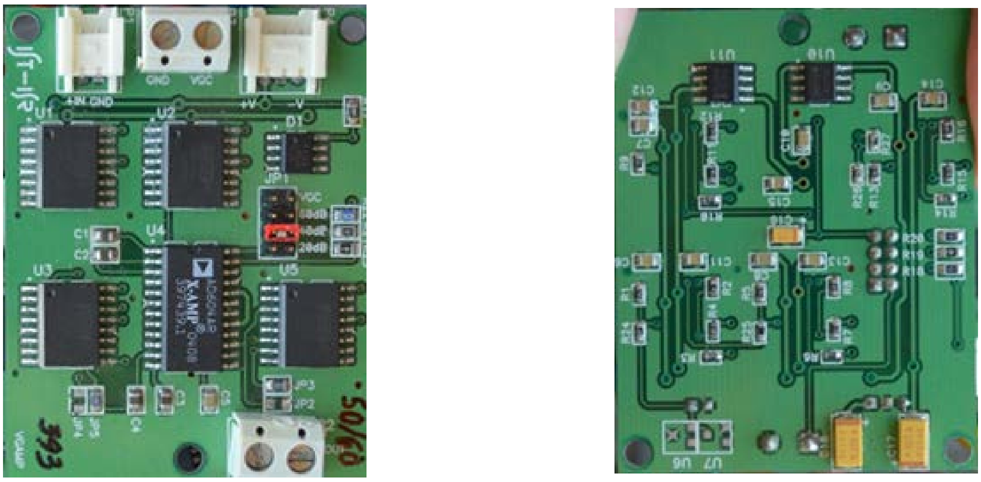

(a) Upper layer.

(b) Lower layer.

Figure D.11: VGAMP board.

A block diagram representative of the VGAMP's functioning can be seen in Fig. D.12.

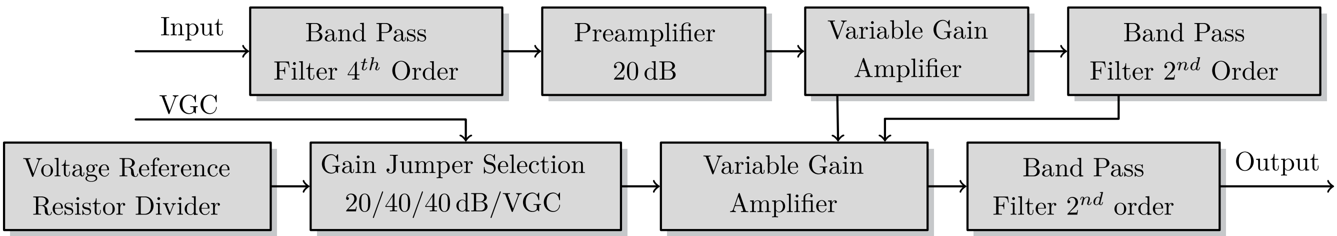

Figure D.12: VGAMP block diagram.

Further specifications of the VGAMP are displayed in table D.3.

Amplifier		Filter	
Input Resistance	300 kΩ	Frequency Range	0 to 100 kHz
Peak Input Voltage	±200 mV	Frequency Accuracy	$< 1\%$
Bandwidth	40 MHz	Maximum Q	400
Output Signal Range	2.5 ± 1.5 V	Input Voltage Range	±11.5 V
Output Impedance	2Ω	Input Resistance	> 1000 MΩ
Absolute Gain Error	±0.3 dB	Operating Voltage Range	±6 to ±18V
Power Supply	+5 V	Quiescent Supply Current	6 mA
Quiescent Supply Current	20 mA@5 V/10 mA@ − 5 V		

Table D.3: VGAMP specifications.

E | Parts design in Solidworks©

The present section introduces a photograph catalog of the devices design in Solidworks©, by the author of this thesis, as an aid to the implementation of the MAST/AM tool's architecture.

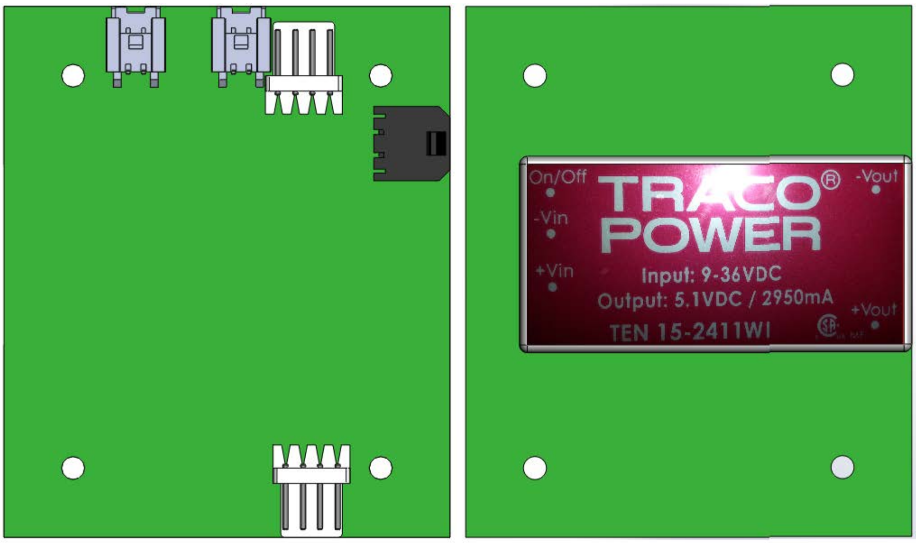

(a) DC-DC.

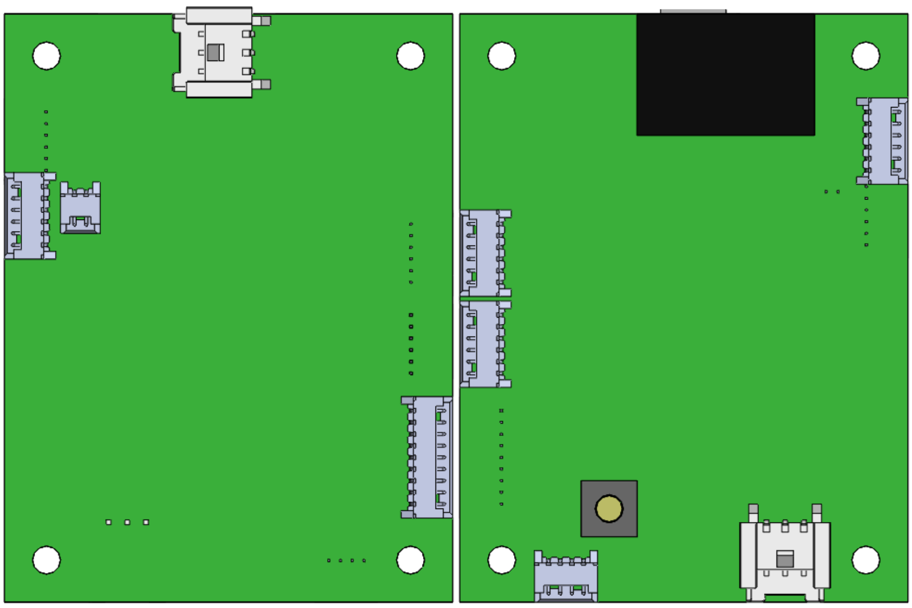

(b) Microcontroller AVRCAN128.

(c) Android device.

(d) ITC-1042 Spherical Omnidirectional Transducer Acoustic Transducer.

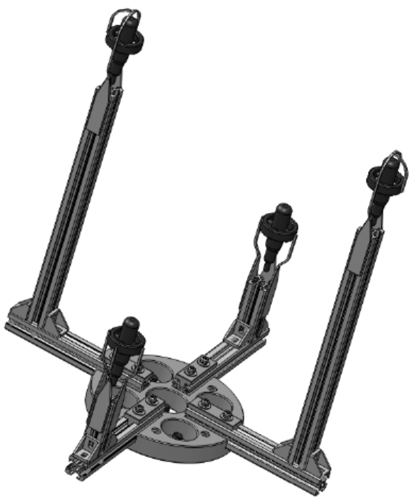

(e) USBL Array.

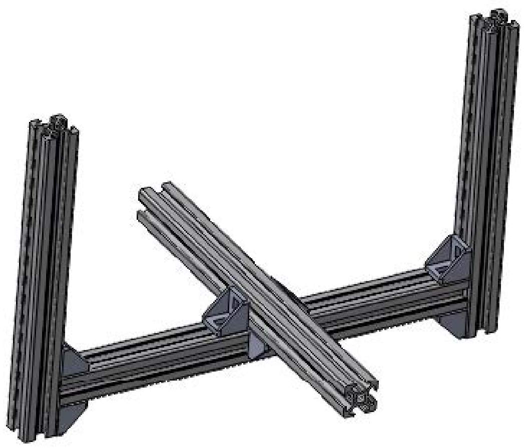

;

(f) Handler.

(a) Ethernet/USB Adapter.

(b) Microstrain 3DM-GX3-35.

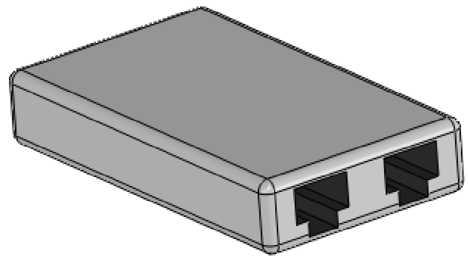

(c) Ethernet Switch.

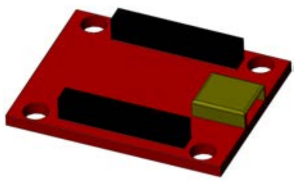

(d) XBEE Explorer USB.

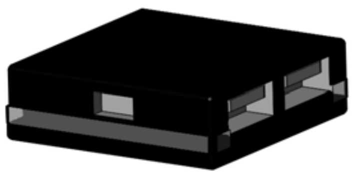

(e) USB Hub.

Figure E.2: Devices designed in Solidoworks.

Bibliography

[1] *Introduction to Radar Systems*. Tata McGraw Hill, 2003.

[2] Cenc Acar and Andrei Shkel. *MEMS Vibratory Gyroscopes: Structural Approaches to Improve Robustness*. Springer, first edition, 2009.

[3] TRACO ELECTRONIC AG. Traco Power. http://www.tracopower.com/, September 2013.

[4] A. Alcocer, P. Oliveira, and A. Pascoal. Underwater Acoustic Positioning Systems Based On Buoys With GPS. *Proceedings of the Eighth European Conference on Underwater Acoustics, 8th ECUA*, 2006.

[5] Matej Andrejasic. MEMS Accelerometers. Technical report, 2008.

[6] Andrew C. Singern, Jill K. Nelson, and Suleyman S. Kozat. Signal Processing for Underwater Acoustic Communications. *Underwater Wireless Communications*, 2009.

[7] Anrophysics. Earth's Magnetic Field. http://www.patana.ac.th/secondary/science/anrophysics/ntopic6/commentary.htm, April 2013.

[8] ASIX. Asix Electronics Corporation. http://asix.com.tw/, April 2013.

[9] ASIX. Asix Electronics Corporation. http://www.asix.com.tw/products.php?op=pItemdetail&PItemID=97;71;101, April 2013.

[10] International Marine Contractors Association. Deep Water Acoustic Positioning. Technical report, 2009.

[11] ATMEL. Maxim Digitally Controlled Fuel-Gauge Interface. Technical report, 2006.

[12] ATMEL. AT90CAN128 Specifications. Technical report, 2008.

[13] T.C. Austin. The application of spread spectrum signaling techniques to underwater acoustic navigation. pages 443–449, 1994.

[14] Pedro Batista. Controlo de Veículos Autónomos Baseado na Informação Directa de Sensores Acústicos. Technical report, Instituto Superior Técnico, Universidade Técnica de Lisboa, September 2005.

[15] D. Richard Blidberg. The Development of Autonomous Underwater Vehicles (AUV); A Brief Summary. Technical report, 2001.

[16] Boeffla-Kernel. Boeffla-Kernel ... your daily-usage kernel for the Samsung Galaxy S3. http://www.boeffla-kernel.de/index.php/about-the-kernel, June 2013.

[17] Bosch. BMP085 Digital Pressure Sensor. Technical report, 2011.

[18] Pablo Brenner. A Techical Tutorial on the IEEE 82.11 Protocol. Technical report, 1997.

[19] Pablo Brenner. Microstrain 3DM-GX3-35 Miniature Attitude Heading Reference System Datasheet. Technical report, 2013.

[20] Robert C. Briggs. Mechanical design of a self-mooring autonomous underwater vehicle. Master's thesis, Virginia Polytechnic Institute, Decemeber 2000.

[21] Bruno Cardeira. Arquitecturas para Navegação Inercial/GPS com Aplicação a Veículos Autónomos. Master's thesis, Universidade Técnica de Lisboa, Instituto Superior Técnico, Fevereiro 2009.

[22] International Transducer Corporation. Model ITC-1042. Technical report, 2008.

[23] John J. Craig. *Introduction to Robotics: Mechanics and Control*. Prentice-Hall, third edition, 2003.

[24] CyanogenMod. Cyanogenmod: A Customized Aftermarket Firmware Distribution. http://www.cyanogenmod.org/, June 2013.

[25] Jose Eduardo Charters Ribeiro da Cunha Sanguino. Reference coordinate systems. University Lecture, 2012.

[26] Jose Eduardo Charters Ribeiro da Cunha Sanguino. Reference coordinate systems. University Lecture, 2012.

[27] E. Dentia, R. Galatoloa, and F. Schettinia. An AHRS Based on a Kalman Filter for the Integration of Inertial, Magnetometric and GPS Data. *Aerotecnica Missili & Spazio, The Journal of Aerospace Science, Technology and Systems*, 2010.

[28] D.SignT. Signal Processing Tools. http://www.dsignt.de/, September 2013.

[29] Mark Euston, Paul Coote, Robert Mahony, Jonghyuk Kim, and Tarek Hamel. A Low-Cost and Low-Weight Attitude Estimation System for an Autonomous Helicopter. *International Conference on Intelligent Robots and Systems*, 1997.

[30] Mark Euston, Paul Coote, Robert Mahony, Jonghyuk Kim, and Tarek Hamel. A Complementary Filter for Attityde Estimation of a Fixed-Wing UAV. *International Conference on Intelligent Robots and Systems*, 2008.

[31] JW Fishers. Underwater Search Equipment. http://www.jwfishers.com/, September 2013.

[32] C. Forney, E. Manii, M. Farris, M.A. Moline, C.G. Lowe, and C.M. Clark. Tracking of a Tagged Leopard Shark with an AUV: Sensor Calibration and State Estimation. *2012 IEEE International Conference on Robotics and Automation*, 2012.

[33] Eclipse Foundation. Featured Eclipse Project. http://www.eclipse.org/, December 2012.

[34] Daniel W. French. Analisys of Unmanned Undersea Vehicle (UUV) Architectures and an Assessment of UUV Integration Into Undersea Applications. Master's thesis, Naval Postgraduate School, Civilian, Department of the Navy B.S., University of Rhode Island, September 2010.

[35] Environmental Geophysics. Earth's Magnetic Field Intensity Variation. http://www.epa.gov/esd/cmb/GeophysicsWebsite/pages/reference/properties/Magnetic_Susceptibility/Geomagnetic_Field.htmm, April 2013.

[36] Google. Android Jelly Bean. http://developer.android.com/about/versions/android-4.1.html, September 2013.

[37] Google. Sensors Overview. http://developer.android.com/guide/topics/sensors/sensors_overview.html, April 2013.

[38] P.D. Groves. *Principles of GNSS, inertial, and multi-sensor integrated navigation systems*. GNSS technology and applications series. Artech House, 2008.

[39] W.T. Higgins. A comparison of complementary and kalman filtering. *Aerospace and Electronic Systems, IEEE Transactions on*, AES-11(3):321–325, 1975.

[40] TELEDYNE Impulse. Ie55 subminiature. http://www.teledyneimpulse.com/products/submini.aspx, October 2013.

[41] H. Iro. *A Modern Approach to Classical Mechanics*. World Scientific, 2002.

[42] Jones. Universal Serial Bus Specification. Technical report, 2000.

[43] Jones. The IEEE 802.3 Standard (Ethernet). Technical report, 2001.

[44] Eric M. Jones and Paul Fjeld. Gimbal Angles, Gimbal Lock. www.hq.nasa.gov, September 2013.

[45] M. Kayton and W.R. Fried. *Avionics Navigation Systems*. A Wiley-Interscience publication. John Wiley & Sons, 1997.

[46] M. Kok, J.D. Hol, T.B. Schon, F. Gustafsson, and H. Luinge. Calibration of a magnetometer in combination with inertial sensors. pages 787–793, 2012.

[47] Kokam. Cell Specification Data SLPB 75106205. Technical report, 2012.

[48] A. Lawrence. *MODERN INERTIAL TECHNOLOGY.: Navigation, Guidance, and Control, 2nd edition*. Mechanical engineering series. Springer, 1998.

[49] John J. Leonard, Andrew A. Bennett, Christopher M. Smith, and Hans Jacob S. Feder. Autonomous Underwater Vehicle Navigation. *MIT Marine Robotics Laboratory Technical Memorandum*, 1998.

[50] Computing Linux. Linux / unix command: ping. http://linux.about.com/od/commands/l/blcmdl8_ping.htm, October 2013.

[51] Sebastian O.H. Madgwick. An Efficient Orientation Filter for Inertial and Inertial/Magnetic Sensor Arrays. Technical report, 2010.

[52] W. Mauerer. *Professional Linux Kernel Architecture*. Wrox professional guides. Wiley, 2008.

[53] G. Milette and A. Stroud. *Professional Android Sensor Programming*. Wrox, 2012.

[54] M. Morgado, P. Oliveira, and C. Silvestre. Experimental evaluation of a USBL underwater positioning system. *ELMAR, 2010 PROCEEDINGS*, pages 485–488, 2010.

[55] Marco Martins Morgado, Paulo Jorge Oliveira, and Carlos Jorge Silvestre. Sistema de Navegação Inercial com Ajuda USBL. Technical report, 2006.

[56] P. Oliveira, C. Silvestre, M. Morgado, K. Erzini, L. Bentes, A. Afonso, F. Hazin, and B. Block. Preliminary results from project mast/am-advanced tracking and telemetry methodologies to study marine animals. *OCEANS, 2011 IEEE - Spain*, pages 1–6, 2011.

[57] Alan V. Oppenheim and R.W. Schafer. *Digital signal processing*. Prentice-Hall international editions. Prentice-Hall, 1975.

[58] Hewlett Packard Company, Intel Corporation, LSI Corporation, Microsoft Corporation, Renesas Electronics Corporation, and ST-Ericsson. On-The-Go and Embedded Host Supplement to the USB Revision 2.0 Specification. Technical report, 2012.

[59] A. Pascoal, I. Kamminer, and P. Oliveira. Navigation system design using time-varying complementary filters. *Control Applications, 1998. Proceedings of the 1998 IEEE International Conference on*, 2:1099–1104 vol.2, 1998.

[60] A. Pascoal, P. Oliveira, C. Silvestre, L. Sebastiao, M. Rufino, V. Barroso, J. Gomes, G. Ayela, P. Coince, M. Cardew, A. Ryan, H. Braithwaite, N. Cardew, J. Trepte, N. Seube, J. Champeau, P. Dhaussy, V. Sauce, R. Moitie, R. Santos, F. Cardigos, M. Brussieux, and P. Dando. Robotic ocean vehicles for marine science applications: the european asimov project. *OCEANS 2000 MTS/IEEE Conference and Exhibition*, 1:409–415 vol.1, 2000.

[61] Douglas Pincock, David Welch, Scott McKinley, and George Jackson. Acoustic Telemetry for Studying Migration Movements of Small Fish in Rivers and the Ocean - Current Capabilities and Future Possibilities. *PNAMP Special Publication: Tagging, Telemetry, and Marking Measures for Monitoring Fish Populations*, 2010.

[62] Samsung. Samsung Open Source Release Center. http://opensource.samsung.com/, April 2013.

[63] D. Simon. *Optimal State Estimation: Kalman, H Infinity, and Nonlinear Approaches*. Wiley, 2006.

[64] Sparkfun. Barometric Pressure Sensor - BMP085 Breakout. https://www.sparkfun.com/products/retired/9694, September 2013.

[65] Sparkfun. Xbee Explorer USB. https://www.sparkfun.com/products/8687, September 2013.

[66] M. Stojanovic, J.G. Proarkis, J.A. Rice, and M.D. Green. Spread spectrum underwater acoustic telemetry. *OCEANS '98 Conference Proceedings*, 2:650–654 vol.2, 1998.

[67] Subcon©. Underwater Pluggable Electrical Connectors. http://www.subconn.com/, October 2013.

[68] Salah Sukkarieh. *Low Cost, High Integrity, Aided Inertial Navigation Systems for Autononous Land Vehicles.* PhD thesis, University of Sidney, March 2000.

[69] R.G. Takwale and P.S. Puranik. *Introduction to Classical Mechanics.* Tata McGraw-Hill, 1979.

[70] D. Titterton, J.L. Weston, and Institution of Electrical Engineers. *Strapdown Inertial Navigation Technology, 2nd Edition.* IEE radar, sonar, navigation, and avionics series. Institution of Engineering and Technology, 2004.

[71] Theodore Ts'o. Standalone Device Drivers in Linux. *Proceedings of the FREENIX Track: 1999 USENIX Annual Technical Conference*, 1999.

[72] T. Ura, J. Kojima, T. Nakano, H. Sugimatus, K. Mori, R. Hirotsu, and M. Yanagishawa. Experimental result of auv-based acoustic tracking system of sperm whales. *OCEANS 2006 - Asia Pacific*, pages 1–5, 2006.

[73] Krishnaraj Varma. Time-Delay-Estimate Based Direction-of-Arrival Estimation for Speech in Reverberant Environments. Master's thesis, Virginia Polytechnic Institute, October 2002.

[74] VENCO©. V16 Continuous Transmitter. Technical report, 2010.

[75] VENCO©. V8 Coded Transmitter. Technical report, 2011.

[76] VENCO©. Vemco Positioning System (VPS) Datasheet. Technical report, 2013.

[77] VENCO. VR100 Receivers. http://vemco.com/products/vr100/, June 2013.

[78] K. Vickery. Acoustic positioning systems. a practical overview of current systems. *Autonomous Underwater Vehicles, 1998. AUV'98. Proceedings of the 1998 Workshop on*, pages 5–17, 1998.

[79] Oliver J. Woodman. An Introduction to Inertial Navigation. Technical report, 2007.

[80] Wordpress. Geoid. http://geograficamente.wordpress.com/2009/03/19/1621/, April 2013.

[81] xda developers. Android. http://forum.xda-developers.com/wiki/Android, September 2013.

[82] xda developers. Samsung Galaxy S III. http://forum.xda-developers.com/wiki/Samsung_Galaxy_S_III, September 2013.

[83] Yu Yang, Zhang Xiaomin, Peng Bo, and Fu Yujing. Design of sensor nodes in underwater sensor networks. *Industrial Electronics and Applications, 2009. ICIEA 2009. 4th IEEE Conference on*, pages 3978–3982, 2009.